Étude de Nouveaux Matériaux Polymères pour Membranes de Séparation et Actionneurs Contrôlés par Stimuli

par

Liangliang Dong

Thèse présentée au Département de chimie en vue
de l'obtention du grade de docteur ès sciences (Ph.D.)
FACULTÉ DES SCIENCES, UNIVERSITÉ DE SHERBROOKE

présentée au School of Chemical and Material Engineering en vue
de l'obtention du grade de Docteur
JIANGNAN UNIVERSITY

Sherbrooke, Québec, Canada, September 2018

Le 28 September 2018

le jury a accepté la thèse de monsieur Liangliang Dong
dans sa version finale.

Membres du jury

Professeur Yue Zhao
Directeur de recherche
Département de chimie

Professeur Mingqing Chen
Codirecteur de recherche
Université de Jiangnan

Professeur Yves Dory
Président-rapporteur
Département de chimie

Professour Armand Soldera
Évaluateur interne
Département de chimie

Professeur Christopher Barrett
Évaluateur externe
Université de McGill

SOMMAIRE

Les matériaux qui réagissent aux stimuli ont trouvé beaucoup d'applications. Ils peuvent changer leurs propriétés chimiques et/ou physiques lorsqu'ils sont exposés à des conditions environnementales changeantes. Les membranes poreuses de séparation et les actionneurs polymères sensibles aux stimuli sont deux applications représentatives, et font l'objet de cette thèse. D'une part, les membranes poreuses sensibles aux stimuli peuvent ajuster leurs propriétés de transfert de masse et interfaciales pour manipuler la perméabilité et la sélectivité en réponse à des stimuli tels que le pH, la lumière, la température, l'oxydoréduction, etc. Malgré le développement rapide, il existe certaines limites pour ce type de membranes intelligentes. Par exemple, pour les membranes sensibles au pH, l'addition d'acides et de bases dans la solution entraîne une accumulation de sel qui peut contaminer le système et affecter le fonctionnement. Alors que pour les membranes sensibles à un changement de température et à la lumière, elles peuvent être endommagées par les stimuli dans une certaine mesure. Conséquemment, il est encore urgent de développer des méthodes de stimulation nouvelles qui sont conviviales pour l'environnement et rentables. D'autre part, les actionneurs polymères ont acquis un intérêt croissant en raison de leurs applications potentielles pour la biomédecine, les muscles artificiels et les robots souples. Au lieu d'utiliser une force mécanique pour obtenir un mouvement ou une déformation, les actionneurs polymères peuvent se déplacer ou se déformer sous l'effet d'une stimulation thermique, optique ou électrique. Parmi ceux-ci, les actionneurs en réseaux de polymères à cristaux liquides (LCN) et contrôlés par la lumière via un effet photothermique sont émergés comme un système de matériaux particulièrement prometteur. Pour ce type d'actionneur, des agents photothermiques sont nécessaires pour convertir l'énergie optique en énergie thermique afin d'induire la transition de phase LC-isotrope qui entraîne la déformation macroscopique de l'actionneur. Cependant, les agents photothermiques ont souvent une mauvaise compatibilité avec les polymères organiques, ce qui restreint leur concentration et ainsi limite l’effet photothermique. De plus, c’est un défi de fabriquer des actionneurs LCN pouvant se déplacer comme une chenille dont le mouvement est

guidé par la lumière.

L'objectif principal de cette thèse est de développer de nouvelles membranes poreuses sensibles aux stimuli pour la séparation dépendant de la taille et la nanofiltration ainsi que des actionneurs polymères à base de LCN capables de mouvement contrôlé à distance. La conception rationnelle des matériaux, inspirée par la nature, nous permet de relever les défis ou de surmonter les problèmes mentionnés ci-dessus. Plus spécifiquement, d'une part, nous utilisons des polymères sensibles au gaz CO_2 dans une membrane de séparation pour qu'elle puisse "ouvrir" et "fermer" de façon réversible les pores et ainsi renforcer la sélectivité de séparation sous stimulation gazeuse. Comparé à d'autres stimuli, l'utilisation du CO_2 présente plusieurs avantages, tels que le respect de l'environnement, la facilité d'utilisation, une excellente robustesse sans dommage ni contamination et une bonne efficacité pour l'intérieur de la membrane. D'autre part, nous démontrons un actionneur tricouche à base de LCN sensible à l'effet photothermique. Guidé par un laser proche infrarouge (NIR), il peut effectuer des changements de forme et des mouvements sur une surface non traitée, horizontale ou inclinée. Les travaux de recherche de cette thèse portent principalement sur ces deux sujets et sont présentés en trois chapitres. L'ensemble des résultats contribue à l'avancement de nos connaissances fondamentales sur le développement et les applications de polymères sensibles aux stimuli.

Dans le premier projet, nous avons proposé un nouveau concept pour contrôler la taille des pores d'une membrane de séparation par le CO_2. Un polymère sensible au CO_2, le poly (méthacrylate de N, N-diéthylaminoéthyle) (PDEAEMA), a été greffé à la membrane de polyvinylidène (PVDF) modifié avec la polydopamine (PDA) pour subir une expansion et un effondrement de chaîne réversible en réponse au CO_2 et Ar en solution, respectivement, entraînant la fermeture et l'ouverture correspondantes des pores dans la membrane. La séparation contrôlée de nanoparticules d'or (AuNPs, 50 nm de diamètre) a été démontrée. Cette nouvelle modalité de contrôle du gaz montre un grand potentiel pour le développement des membranes intelligentes pour des

applications qui nécessitent ou impliquent une séparation ajustable et sélective en fonction de la taille d'espèces moléculaires ou de nanoparticules.

Sur la base du premier travail, afin d'améliorer davantage la capacité de séparation sélective des membranes polymères sensibles au CO_2, nous avons développé une nouvelle membrane de nanofiltration en greffant du PDEAEMA modifié par la pyrène (Py-PDEAEMA) sur l'oxyde de graphène (GO). Cette membrane de nanofiltration en matériau composite présente un certain nombre d'attributs potentiellement attrayants pour le traitement de l'eau, tels que la perméabilité réversiblement changeable, la perméabilité à l'eau élevée, le rejet de molécules de colorants organiques et un changement réversible de signe de charge en surface. À notre connaissance, il s'agit de la première étude sur les membranes de nanofiltration sensibles au gaz. Notre conception de membrane combine les avantages des polymères sensibles au CO_2 et des membranes de nanofiltration à base de GO. Notre recherche a ainsi démontré de nouvelles perspectives dans le développement des membranes de nanofiltration intelligentes pour la purification de l'eau.

Le troisième, et dernier, projet porte sur le design et la démonstration d'un nouvel actionneur à base de LCN, lequel est capable d'effectuer un mouvement de chenille guidé par un laser NIR. L'actionneur a une structure à trois couches, comprenant une couche supérieure d'oxyde de graphène réduit (RGO), une couche intermédiaire de polymère inactive et une couche inférieure active de LCN. Lorsque le côté RGO est exposé à un laser NIR en mouvement, la déformation de l'actionneur sous forme d'une bande crée une onde mobile le long de la direction de mouvement du laser, ce qui fait de l'actionneur un marcheur à chenille efficace dont le déplacement est piloté et guidé à distance par le laser. De plus, en déposant RGO, l'agent photothermique, directement sur la surface d'une couche de polymère de l'actionneur, le problème potentiel de compatibilité de RGO avec les polymères est évité.

Mots clés: polymères sensibles au CO_2, membrane de séparation, oxyde de graphène, actionneurs polymères, polymères cristallins liquides

ABSTRACT

Stimuli-responsive materials have exhibited a wide range of applications, because the necessity of designing novel "smart" systems usually requires materials that can change their chemical and/or physical properties upon exposure to changed environmental conditions. Two representative applications are stimuli-responsive porous membranes and polymer actuators which are subjects of this thesis. On one hand, stimuli-responsive porous membranes are a class of membranes that can adjust their mass transfer and interfacial properties to manipulate permeability and selectivity in response to changing environmental conditions, such as pH, light, temperature, redox, and so on. There has been a rapid development in this field over the past decades or so. However, there are some limitations for these stimuli-responsive porous membranes. For example, for pH-responsive porous membranes, addition of acids and bases into the solution results in salt accumulation that can contaminate the system and diminish the switchability, while temperature or light responsive porous membranes may be damaged by the stimuli to a certain extent. Therefore, it is still urgent to develop environmentally friendly and cost-effective stimulation modes for stimuli-responsive porous membranes. On the other hand, polymer actuators have aroused scientists' extensive research interest because of their potential applications in biomedicine, artificial muscles and soft robots. Instead of utilizing mechanical force to achieve motion or deformation, polymer actuators can move or deform under thermal, optical or electrical stimulation. Among them, photo-thermal-responsive polymer actuators based on liquid crystal polymer networks (LCNs) have emerged as a particularly promising materials system. For this kind of actuator, the photothermal agents are needed to convert optical energy into thermal energy to induce the LC-to-isotropic phase transition that drives the actuator to deform macro-scopically. However, the photothermal reagents often have poor compatibility with or-ganic polymeric matrices, resulting in a dilemma that reducing the doping percentages

of photothermal reagents would weaken the photo-actuation speeds of the LCN actuators, whereas increasing the doping percentages would lead to serious phase segregations, and then sacrifice the mechanical properties of the LCN actuators. Moreover, fabricating photothermal-responsive LCN actuators that can perform light-driven caterpillar-type motion on untreated surfaces is also challenging. The main topic of this thesis is to learn from nature to design and fabricate the stimuli-responsive porous membranes for the size separation and nanofiltration and the stimuli-responsive polymer actuators based on LCN for remotely controlled motion. We introduce the CO_2-responsive polymers into membrane separation, in a bid to develop a new external stimulus that can reversibly "open" and "close" the membrane pore sizes and further impact the size selectivity of the membrane. Compared with other stimuli, using CO_2 as trigger has several merits, such as environmental friendliness, easy operation, excellent repeatability without any damage and contamination and good depth inside the membranes. Moreover, we designed a photothermal-responsive LCN-based trilayer actuator that can perform near-infrared (NIR) light -guided bending, moving waves and motion on untreated, either horizontal or inclined surface. The research works in this thesis mainly contain above-mentioned two topics, presented in three chapters.

In the first work, we proposed a novel concept that gas-tunable pore sizes as well as gas-controlled separation of species can be successfully realized by using CO_2/Ar as trigger. In this work, a CO_2-responsvie polymer, poly(*N*,*N*-diethylaminoethyl methacrylate) (PDEAEMA), was grafted to the polydopamine (PDA) modified polyvinylidene fluoride (PVDF) membrane to undergo reversible contraction/extension in response to CO_2/Ar, resulting in the corresponding opening and closure of membrane pore. The reversible rejection of gold nanoparticles (AuNPs) with the diameter of 50 nm can be realized by alternating CO_2/Ar bubbling time. This novel modality that integrates CO_2-responsive polymers, tunable membrane pore size and membrane separation shows the great potential of developing smart membranes for applications requiring or involving tunable, size-selective separation of molecular species or nanoparticles.

On the basis of the first work, in order to improve the separation capability of CO_2-responsive polymer membranes, we developed a CO_2-responsive nanofiltration membrane based on pyrene modified PDEAEMA (Py-PDEAEMA) and graphene oxide (GO) for water purification. This composite nanofiltration membrane had a number of attributes potentially appealing for water treatment, such as the reversible, gas-tunable water permeability, both high water permeability and rejection of organic dye molecules and gas-tunable changes of the charge sign. To our knowledge, this is the first report about CO_2-responsive nanofiltration membrane. This work combines the advantages of a CO_2-responsive polymers and GO-based nanofiltration membrane, demonstrating new perspectives in developing smart stimuli-responsive nanofiltration membranes for water purification.

In the third work, we designed a LCN-based actuator that performed NIR light-guided locomotion. The actuator had a trilayer structure, including a thin reduced graphene oxide (RGO) top layer, an inactive polymer middle layer and an active LCN bottom layer. When exposing the RGO side to a moving NIR laser, a moving wave along the strip actuator is generated, which makes the strip an effective caterpillar walker that could move on untreated, either horizontal or inclined surface under the guide of NIR laser. Moreover, while known actuators using photothermal effect are usually fabricated by mixing the nanofiller as NIR light heater with the polymer, which may weak the reversible deformation degree and raise the compatibility concern, the easy trilayer fabrication method laminates directly a “sheet” of RGO on thick polymer layers, which circumvents the potential problems.

Keywords: CO_2-responsive polymers, membrane separation, graphene oxide, polymer actuators, liquid crystalline polymers

摘要

刺激响应性聚合物可以通过感知周围环境的变化而自发地调节自身物化性能来适应环境的变化，由于这种特殊的性质，此类聚合物目前已经被广泛地应用于各种领域。其中，两个代表性的应用分别为刺激响应性多孔膜和聚合物制动器，这也本论文的研究内容。一方面，刺激响应性多孔膜是一类可以根据周围环境的变化（如，pH，光，热，氧化还原等），来自发调节膜的传质性能从而实现对膜通量和选择性的可逆调节的智能多孔分离膜。近年来，该领域的发展迅速，各种响应性多孔膜已经被相继报道。但是，这些刺激响应性多孔膜，仍存在一些不足。例如，对于 pH 响应性的多孔膜，由于需要使用酸碱溶液来实现调节，因此，随着循环次数的增加造成盐积累现象，从而造成膜污染和膜分离性能下降等现象；光或热响应性的多孔膜，也会一定程度上地破坏膜结构的完整性。因此，开发一种环境友好型的刺激响应聚合物膜是十分必要和迫切的。另一方面，聚合物致动器因其在生物医学、人造肌肉、软体机器人等领域具有广泛的应用潜能，正在不断地引起科学家的研究兴趣。不同于那些利用机械力来使物体发生移动或变形，聚合物制动器可以在光、热、电等刺激下，实现自身的移动或变形。这其中，尤以基于液晶聚合物网络的光热响应性的聚合物制动器，最为引人注目。这类聚合物制动器，可以利用添加其中的光热剂，将光能转化成热能，从而引起液晶聚合物基质发生相变(从液晶相转变为各向同性相),从而引起整个物体的宏观运动。然而,由于这类聚合物制动器中的光热剂通常与聚合物基质的亲和性不好,因此,使得这类聚合物制动器陷入一个两难的境地：如果降低光热剂的含量，则会降低制动器的光热响应速度;而如果增加光热剂的含量,则会造成严重的相分离现象,从而降低材料的力学性能。此外，这类聚合物制动器中的一部分，可以模仿自然界中的毛毛虫，实现行走或爬坡。但是，需在经过处理的表面或是其他辅助条件下才能实现。因此，开发一种新型的基于液晶聚合物网络的光热响应性的聚合物制动器来解决上述两方面的问题，仍具有相当的挑战性。基于以上分析，本论文

的主要研究内容为，通过向自然界学习，设计、制备和研究新型刺激响应性多孔膜，以期实现对膜通量以及选择性的调控，同时考察其在纳滤领域的应用；设计、制备和研究新型刺激响应性聚合物制动器，以期实现远距离可控的响应性。我们将 CO_2 响应性聚合物引入到膜分离领域，以期将此作为一种新的刺激源，实现对膜通量和分离性的可逆调控，从而解决上文所提出的第一个难点。因为，相比于其他刺激源，将 CO_2 作为刺激源，具有环境友好、操作简单、重复性好、无膜污染、不损害膜结构、高渗透性等优点。另外，我们设计一种新型的光热响应的液晶聚合物网络制动器，该聚合物制动器具有三层结构，可以在近红外光（NIR）的刺激下，实现弯曲、波浪以及在光滑的表面上行走和爬坡，以期解决上文所提出的第二难点。

在本论文的第一个研究中，我们提出利用气体作为刺激源，来制备一种新型的气体响应性聚合物多孔膜。通过循环地通入 CO_2 或 Ar，来实现对膜通量和分离性能的调控。在本研究中，我们将一种具有 CO_2 响应性的聚合物，聚 N, N-二乙基胺基甲基丙烯酸乙酯（PDEAEMA），成功引入到经聚多巴胺（PDA）修饰过的聚偏氟乙烯（PVDF）多孔基质膜中。通过循环地向体系中通入 CO_2 或 Ar，PDEAEMA 的聚合物链能够发生可逆的溶胀或收缩，从而调节膜孔径的“关闭”或“打开”，进而实现对膜通量和选择性的调控。通过随后的金纳滤颗粒的截留实验，表明只要通过简单调控 CO_2 或 Ar 的通入时间，就可以实现对直径为 50 纳米的金纳米颗粒的可逆截留。本研究所设计的新型刺激响应性多孔膜，成功将 CO_2 响应性的聚合物融合到多孔膜中，实现了对膜孔径的完美调控，这将为设计具有可调孔径的，可逆的尺寸筛分能力的新型智能化多孔膜，提供借鉴和指导。

在上一个研究的基础上，为了提高 CO_2 响应性多孔膜的分离精度，在第二个研究中，我们将 CO_2 响应性的聚合物引入到纳滤膜中，制备了一种基于氧化石墨烯的 CO_2 响应性的复合纳滤膜，用于对不同盐的可逆截留。这种新型的刺激响应复合纳滤膜具有一些优异的特点，如，可逆的气体可控的膜通量、对染料分子同时具有高的截留率和高的水通量、以及气体可控的膜电荷的改变，非常适合应用于水处理。本研究首次将 CO_2 响应性聚合物应用于纳滤膜领域，为今后开发用于水处理的刺激响应性聚合物膜提供了理论支持和实验依据。

在本论文的第三个研究中，我们设计了一种具有光热响应性的基于液晶聚合物网络的制动器，该制动器具有三层结构，上层为薄的氧化石墨层，中间为胶黏层，底层为液晶聚合物网络层。当用近红外激光照射该制动器的氧化石墨层时，由于底层液晶聚合物网络层的相变引起的非对称性收缩，导致制动器可以形成一个光控移动的波浪。在此基础上，该制动器成功地实现了在光滑表面的光控的移动和爬坡。此外，本研究所提出的具有三层结构的聚合物制动器，也解决了本文开头所提出的光热响应的聚合物制动器所面临的光热剂和聚合物基质亲和性的问题。

关键词：CO_2响应性聚合物，膜分离，氧化石墨烯，聚合物制动器，液晶聚合物

ACKNOWLEDGEMENT

First of all, I would like to express sincere thanks and pay utmost respect to my supervisor, Prof. Yue Zhao, for his earnest instructions and encouragement during my research work and pursuit of my PhD degree at Université de Sherbrooke. It has been a great privilege for me to have an opportunity to study in his group, his unique insights into scientific research and personal charm have affected me deeply. I also would love to thank my co-supervisor, Prof. Mingqing Chen, for his patient guidance and unselfish assistance at Jiangnan University before I came to Canada.

I would like to express my thanks and respect to all the professors and staves working in the Department of Chemistry at the Université de Sherbrooke, for their kind assistance during my PhD study. I also would like to thank Prof. Christopher Barrett (Université de McGill), and Profs. Yves Dory and Armand Solder to read my thesis and serving in the jury.

I also sincerely thank all my group members, both past and present, since they are always a tremendous help for me in both life and study at Sherbrooke: Mrs. Xia Tong, Prof. Hongji Zhang, Dr. Weizheng Fan, Dr. Bing Yu, Dr. Hui Xiao, Dr. Rong Yang, Dr. Jun Xiang, Mrs. Amelie Auge, Mr. Farhad Farnia, Mr. Feijie Ge, Mr. Zhichao Jiang, Mr Yaoyu Xiao and Mr. Lu Yin. Especially, I give my sincere thanks to Mrs. Xia Tong for the big help in the characterization tests and good advice in the measurements in the lab. Thanks also for all group members and colleagues in Prof. Chen's lab in Jiangnan University.

I would like to thank the Chinese Scholar Council (CSC) for supporting my life and study in Canada. I also thank all the members of the Education Office of the Chinese

Embassy in Canada. I also sincerely thank for the love and encouragement from my parents and kinsfolks during my study in Canada.

Finally, I would like to acknowledge the financial support from the following organizations: Natural Sciences and Engineering Research Council of Canada (NSERC), le Fonds de recherche du Québec: Nature et technologies (FRQNT), National Natural Science Foundation of China (No.51173072, No. 21571084 and No. 21504031) and Natural Science Foundation of Jiangsu Province (No. BK20150135).

TABLE OF CONTENTS

LIST OF ABBREVIATIONS

LCST: lower critical solution temperature

P2VP: poly(2-vinyl pyridine)

PMMA: poly(methyl methacrylate)

PES-*b*-PSBMA: polyethersulfone-block-poly(sulfobetaine methacrylate)

PVDF: polyvinylidene fluoride

SP: spiropyran

BSA: bull serum albumin

PES: polyethersulfone

GOD: glucose oxidase

SPMMA:spiropyran-containing methacrylate

AAm: acrylamide

PAN: polyacrylonitrile

SWCNT: single-walled carbon nanotube

pNIPAm-*co*-AAm: poly(N-isopropylacrylamide-*co*-acrylamide)

PAMPS: poly(2-acrylamido-2-methyl-1-propanesulfonic acid)

PMMA-*co*-PDEAEMA: poly(methymethacrylate)-*co*-poly(*N*,*N*-diethylaminoethyl methacrylate)

PNIPAM: poly(*N*-isopropylacryl amide)

SA: stearyl acrylate

P4VP: poly(4-vinyl pyridine)

PAAC: poly(acrylic acid)

AZO: 4,4′-azodianiline

PDA: polydopamine

PVC: poly(vinyl chloride)

PILs: poly(ionic liquid)s

UV light: ultraviolet light

MC: merocyanine

UF: ultrafiltration

PTFE: polytetrafluoroethylene

MF: microfiltration

PET: polyethylene terephthalate

β-CD: *β*-cyclodextrin

PMMS:poly[3-mercaptopropyl-methylsiloxane]

Fc: ferrocene

AZ: azobenzene

AuNR: gold nanorods

AuNS: gold nanosphere

PC: polycarbonate

LC: liquid crystalline

PPFPA: poly(pentafluorophenyl acrylate)

PS-*b*-PDMAEMA: polystyrene-*b*-poly (*N*, *N*-dimethylamino ethyl methacrylate)

PHAAA: poly(histamine acrylamide)

LCPs: liquid-crystal polymers

LCNs: liquid-crystal polymer networks

T_{ni}: nematic-isotropic phase transition temperature

LSPR: localized surface plasmon resonance

PDEAEMA:poly(*N*,*N*-diethylaminoethyl methacrylate)

PS-*b*-P4VP: polystyrene-*b*-poly(4-vinylpyridine)

RAFT: reversible addition-fragmentation chain

DDMAT: 2-(dodecylthiocarbonothioyl thio)-2-methylpropionic acid

AIBN:2,2'-azobis(2-methyl propionitrile)

DCC: N, N'-dicyclohexyl carbodiimide

DA: dopaminehydrochloride

LCEs: liquid-crystal elastomers

LCMs: liquid-crystal monomers

MA: methacrylic acid

RGO: reduced graphene oxide

RB: rhodamine B

MO: methyl orange

GO: graphene oxide

NFM: nanofiltration membrane

PE: polyelectrolyte

THF: tetrahydrofuran

BCP: block copolymer

CNTs: carbon nanotubes

AFM: atomic force microscopy

XRD: X-ray diffraction

PPE: poly(p-phenyleneethynylene)

SEM: scanning electron microscope

SEC: size exclusion chromatograph

NIR light: near infrared light

LIST OF TABLES

LIST OF FIGURES

CHAPTER 1

CHAPTER 2

CHAPTER 3

INTRODUCTION

Stimuli-responsive polymers are defined as macromolecules that can sense a weak stimulating signal in their environment (e.g. pH, temperature, light, redox agents, enzymes, ions, mechanical force, electric and magnetic field) and respond by displaying a relatively large physical or chemical change for different functional expressions (1-4). They have established themselves as ‘‘smart’’ materials. In the past two decades or so, stimuli-responsive polymers have attracted growing interest due to their tremendous potential in a broad spectrum of applications, such as functional materials (5), bio-imaging (6), sensing (7), artificial muscles (8), actuators (9), and membrane separation (10). In the following sections, we will focus on the relevant literatures about two main applications of stimuli-responsive polymers: (1) stimuli-responsive porous membranes and (2) liquid crystal polymer actuators using photothermal effect. These are the research topics of this thesis.

I. Stimuli-responsive Porous Membranes

One of the main applications of stimuli-responsive polymers concerns the design of stimuli-responsive porous membranes where the pore sizes and/or the surface properties can be altered to adjust the permeability and selectivity in response to external stimuli, such as, temperature, light, magnetic and electric fields, pH, salt and redox (11, 12). Generally, stimuli-responsive porous membranes are created by chemically or physically binding stimuli-responsive polymers into traditional porous membranes, providing advanced functions and reinforced performances for breaking through the limitation of traditional membrane technologies (13). According to different target applications, the stimuli-responsive porous membranes can be manufactured with a variety of styles (Figure 1). For example, the membrane types can be flat (Figure 1-a1) (14), fiber (Figure 1-a2) (15) or capsule (Figure 1-a3) (16), which can be applied to various complex technical systems, such as, water purification, separation process, and controlled release (14-16). The stimuli-responsive polymer types (gates) in membrane pores can be linear

polymers (Figure 1-b1) (17), hydrogels (Figure 1-b2) (18), or microspheres (Figure 1-b3) (15), which can undergo reversible extension/collapse or swelling/shrinking under external stimuli to modulate the pore size and surface properties. The gate materials can be introduced into membrane pores in pore-filling form (Figure 1-c1) or pore-covering form (Figure 1-c2) (19, 20). Usually, there are two approaches to designing the stimuli-responsive porous membranes: (a) After the membrane formation, using stimuli-responsive polymers to modify existing membranes by various chemical/physical techniques. (b) During the membrane formation, blending stimuli-responsive polymers as components or additives with membrane polymers.

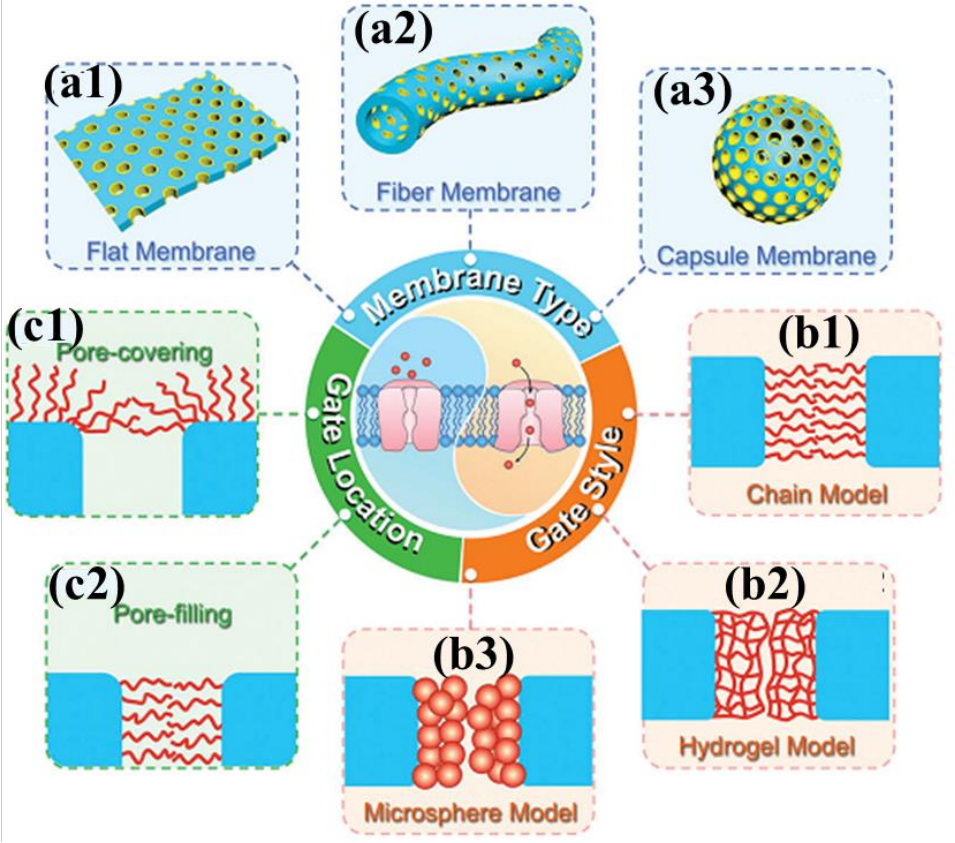

Figure 1. Design of stimuli-responsive porous membranes with various styles inspired by cell membranes. The membrane type: flat membrane (a1), fiber membrane (a2) and capsule membrane (a3). The gate style: linear polymer chains (b1), crosslinked hydrogel networks (b2) and microspheres (b3). The gate location: pore-filling (c1) and pore-covering (c2). Reproduced from [12] with permission from The Royal Society of Chemistry.

I.I. Stimuli-responsive polymers introduced after membrane formation

This strategy usually uses ‘‘grafting’’ techniques that can be divided into the ‘‘grafting from’’ and ‘‘grafting to’’ methods for fabricating stimuli-responsive porous membranes. Both methods endow the fabricated membranes with good response performances and fast response speed. For the ‘‘grafting from’’ method, the stimuli-responsive porous membranes are prepared by polymerizing functional monomers from the pre-treated active sites on the pore surface to form linear polymers or crosslinked networks in the pores (Figure 2 (a)) (18, 19). Up to now, various grafting techniques, such as chemical grafting (21), photo-induced grafting (22), radiation-induced grafting (10), and plasma-induced grafting (23), have successfully grafted different types of stimuli-responsive polymers into membrane substrates.

For the ‘‘grafting to’’ method, the stimuli-responsive porous membranes are prepared by physically/chemically introducing end-functionalized stimuli-responsive polymers, usually in the form of polymer chains or microspheres, to the pore surfaces with pre-treated active sites (Figure 2 (b and c)) (15, 17). Compared with the stimuli-responsive porous membranes fabricated through physical interactions such as van der Waals’ forces (15), the membranes based on chemical grafting are more robust and have a wider range of applications (17). Furthermore, because polymer chain length or the size of microspheres can be well-controlled by adopting appropriate methods, the ‘‘grafting to’’ method shows outstanding controllability and flexibility for the pore microstructures of prepared stimuli-responsive porous membranes.

I.II. Stimuli-responsive polymers introduced during the membrane formation

This strategy enables one-step process for membrane formation and synthesis of stimuli-responsive polymers, displaying excellent potential for easy scale-up. It allows the development of stimuli-responsive porous membranes by using membrane polymers functionalized with stimuli-responsive side chains (Figure 2 (d)), or blending stimuli-responsive block copolymers

(Figure 2 (e)) or microspheres (Figure 2 (f)) with membrane-forming polymers during membrane formation (24-26). These methods skillfully combine the stimuli-responsive polymers incorporation and the membrane formation into one step, which provides an effective and simple strategy for industrial manufacture for stimuli-responsive porous membranes with existing devices.

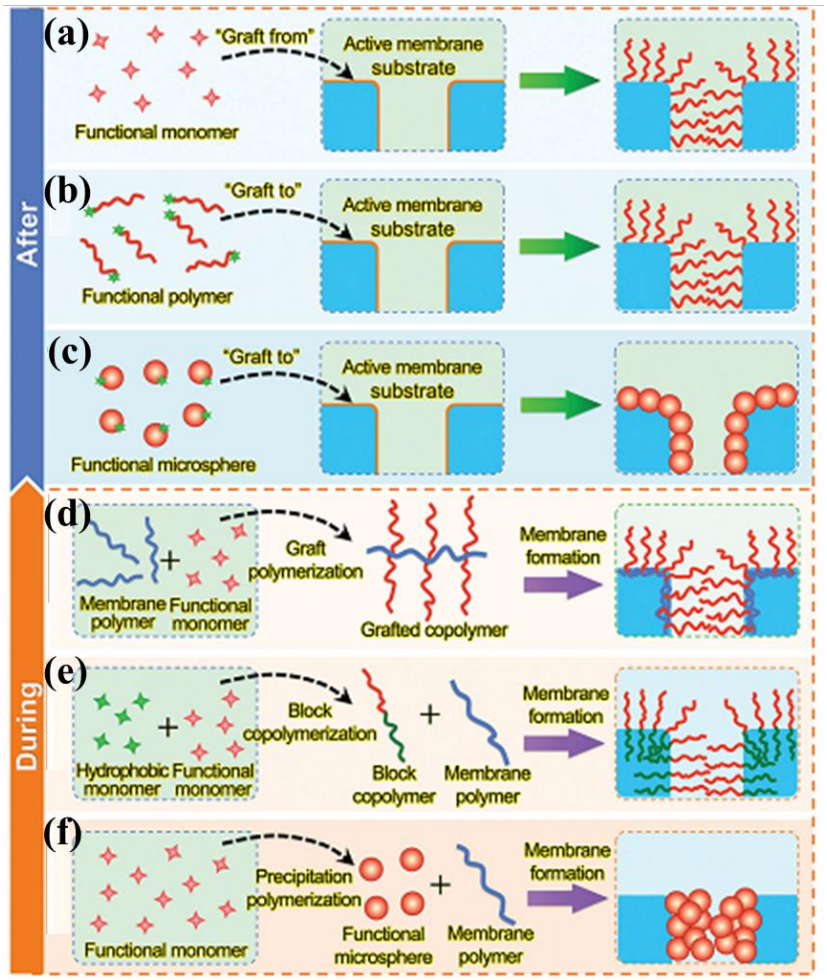

Figure 2. Strategies for design of stimuli-responsive porous membranes by introducing stimuli-responsive polymers after (a-c) or during (d-f) the membrane formation. After the membrane formation: stimuli-responsive porous membranes are fabricated by "grafting from" method (a) or "grafting to" method (b and c). During the membrane formation: stimuli-responsive porous membranes are fabricated by blending grafted copolymers (d), block copolymers (e), or microspheres (f) with membrane polymers. Reproduced from [12] with permission from

The Royal Society of Chemistry.

I.III. Triggers for stimuli-responsive porous membranes

As mentioned above, the response capabilities of stimuli-responsive porous membranes can be realized based on the hydrophobic/hydrophilic changes or/and shrinking/swelling transitions of stimuli-responsive polymers, which can adjust the pore size to increase or decrease the permeability and the surface properties of the pores. In order to meet the versatility demands of industrial production or biological activity, numerous stimuli have been utilized as triggers to develop stimuli-responsive porous membranes.

I.III.I. Thermo-responsive porous membranes

Among the various stimuli-responsive porous membranes, those responsive to temperature are one of the most widely studied. Various thermo-responsive polymers have been employed by scientists to design thermo-responsive porous membranes, including *N*-substituted polyamides, polyethers, poly(2-oxazoline)s, poly(vinyl caprolactone) and poly(methyl vinyl ether) (27). These polymers usually have significant volume changes at their lower critical solution temperature (LCST), which can be used as a thermo-responsive pore-controller in thermo-responsive porous membranes. For instance, poly(N-isopropylacryl amide) (PNIPAM) with a LCST of 32 ºC is typical thermo-responsive polymer. When the temperature is below its LCST, PNIPAM chains are swollen and hydrophilic because of the H-bonds between the amide groups and water molecules, which drives the membrane pores to ‘‘close’’. When the temperature is above the LCST, PNIPAM chains collapse and their volume contracts due to dominant interchain H-bonding, which drives the membrane pores to ‘‘open’’. Chu *et al.* used a copolymer of poly(*N*-isopropylacrylamide-*co*-acryloylamidobenzo-18-crown-6) (PNIPAM-*co*-$AAB_{18}C_6$) to modify nylon-6 membrane for selective detection and removal of trace Pb^{2+} ions (23). A schematic illustration of the process is shown in Figure 3. By simply tuning the operation temperature, selective removal of trace Pb^{2+} ions and effective membrane regeneration can be realized.

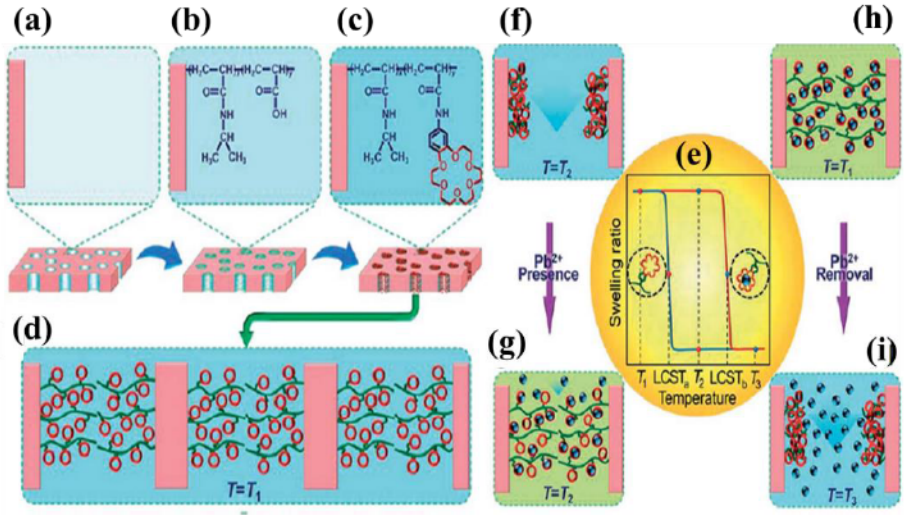

Figure 3. A thermo-responsive porous membrane for the detection and removal of trace Pb^{2+} ions. (a) Nylon-6 membrane. (b) Pore surfaces of the nylon-6 membrane are grafted with poly(*N*-isopropylacrylamide-*co*-acryloylamidobenzo) (PNIPAM-*co*-AA) copolymer. (c and d) The copolymer is modified by 18-crown-6-ether units. (e) A charged complex can be formed between the crown ether units and Pb^{2+} ions, which can shift the LCST from a lower $LCST_a$ to a higher $LCST_b$. (f and g) At T_2 ($LCST_a < T_2 < LCST_b$), the modified copolymer can transform from the collapsed to the swollen state under Pb^{2+} ions, thus decreasing transmembrane flux. (h and i) At T_1 ($< LCST_a$), Pb^{2+} ions can be easily captured by crown ether units and then decomplexed at T_3 ($> LCST_b$). Adapted from [23] with permission from The Royal Society of Chemistry.

I.III.II. pH-responsive porous membranes

Being responsive to pH change is another class of stimuli-responsive porous membranes that have attracted a great deal of attention. In response to change of pH, these membranes exhibit reversible structural and conformational changes, resulting in reversible change of pore size or permeability/selectivity. Generally, pH-responsive porous membrane is fabricated by grafting pH-responsive polymer brushes/chains or cross-linked polymer gels on the pore walls of the substrate membrane, which can induce changes in membrane permeability and/or selectivity

in response to change of pH.

Poly(2-vinyl pyridine) (P2VP) is a typical pH-responsive polymer, which exhibits pH-controlled wettability, conformation and swelling changes. Wang *et al.* used it as a membrane co-constituent with polystyrene (PS) to prepare a pH-responsive mesoporous block copolymer membrane (28). This membrane shows a reversible pH-responsive water flux and can completely separate 10 nm gold particles from a mixture containing 2 nm gold particles. Similar to P2VP, poly(4-vinyl pyridine) (P4VP) is another pH-responsive polymer widely used in the fabrication of pH-responsive porous membranes. For instance, Luo *et al.* reported a block copolymer fiber membrane consisting of P4VP and poly(methyl methacrylate) (PMMA), which showed reversible wetting properties: superhydrophobicity/superoleophilicity or superhydrophilicity/underwater superoleophobicity) (29). At pH=7, the oil could quickly go through this membrane while the water could be completely restricted. However, at pH=3, the water could selectively go through, whereas oil can be blocked (Figure 4 (a)). Moreover, after numerous cycles of the oil/water separation experiments, this membrane still has good stability of its 3D porous structure and excellent reversible wettability. Peinemann *et al.* prepared an asymmetric thin porous membrane *via* self-assembly of PS-*b*-P4VP under the presence of metal ions, which had monodisperse pH-sensitive nanochannels with high pore density ($> 2\times10^{14}$ pore per m^2) (30). When changing the pH from 2 to 8, this membrane exhibits obvious variation of the pore sizes (Figure 4 (c and d)), thus leading to reversible change of water flux by more than two orders of magnitude. Recently, the same group used acetic acid and hydrogen peroxide to treat the pre-prepared PS-*b*-P4VP membrane to fabricate a negatively pH-responsive isoporous membrane, where the pores were open at low pH and closed at high pH (Figure 4 (b)) (31). This membrane exhibits antipodally switchable transmembrane flux and selectivity, compared with PS-*b*-P4VP isoporous membrane.

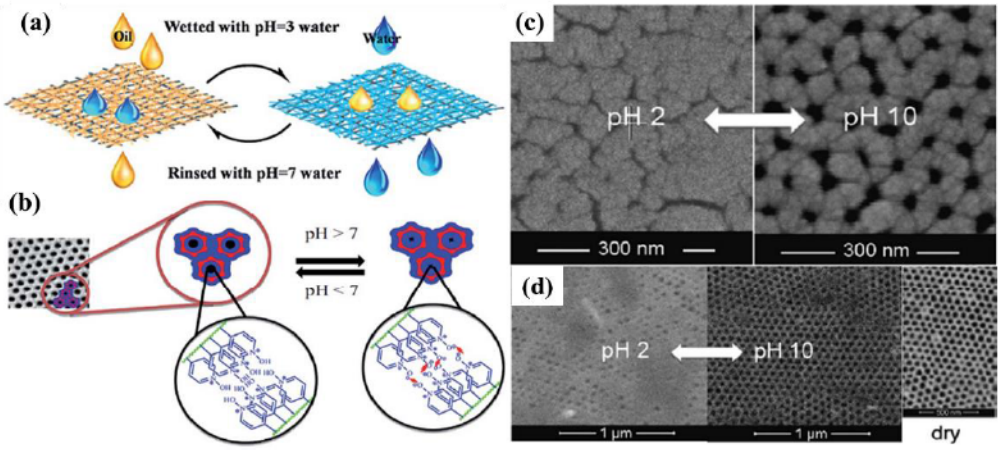

Figure 4. (a) A pH-responsive PMMA-*b*-P4VP fiber membrane that shows reversible oil/water separations. Reproduced from [29] with permission from American Chemical Society. (b) A schematic illustration of the pH-controlled changes of the pore size of a PS-*b*-P4VP-oxide isoporous membrane. Reproduced from [31] with permission from Elsevier. (c) Cryo-field emission scanning electron microscopy (Cryo-FESEM) and (d) environmental scanning electron microscopy (ESEM) of the PS-*b*-P4VP membrane at pH of 2 and 10; (d right) dry membrane observed by ESEM. Reproduced from [30] with permission from American Chemical Society.

I.III.III. Salt-responsive porous membranes

Salt-responsive porous membrane has shown tremendous application potential in the treatment of water. This membrane can reversibly modulate its separation performance and separation mechanism in response to the stimuli of the salt ions and/or strength of the surrounding environment (11). Zhu *et al.* fabricated salt-responsive polyethersulfone (PES) porous membrane blending with amphiphilic polyethersulfone-block-poly(sulfobetaine methacrylate) (PES-*b*-PSBMA) (32). In pure water, the PSBMA chains possess a collapsed chain conformation due to electrostatic interactions between positively charged ammonium groups and sulfonate groups, endowing the pores of this membrane with open state. When adding NaCl into pure water, the collapsed PSBMA chains become extended because Na^+ and Cl^- ions can destroy the electrostatic interactions, which brings the membrane pore to change from an open state to a

closed state. (Figure 5 (a)). Another anion species/strength responsive membrane of PES modified with poly(ionic liquid)s (PILs) copolymers has recently reported by Zhao *et al* (33). This membrane exhibits antipodal salt-response behavior, compared with the work of Zhu *et al*. As shown in Figure 5 (b), when placed in pure water; the positively charged parts of PILs copolymers extend because of the electrostatic repulsion, resulting in volume expansion of the cross-linked PILs copolymers embedded in the PES membranes. This "swelling" can decrease the pore size and reduce the transmembrane flux. When immersed in the salt solution, the positive charges of PILs copolymers are screened by the anions, making the polymer chains contract and then causing the volume contraction of the copolymers. AS a result, the pore size increases, leading to the rise of the transmembrane flux.

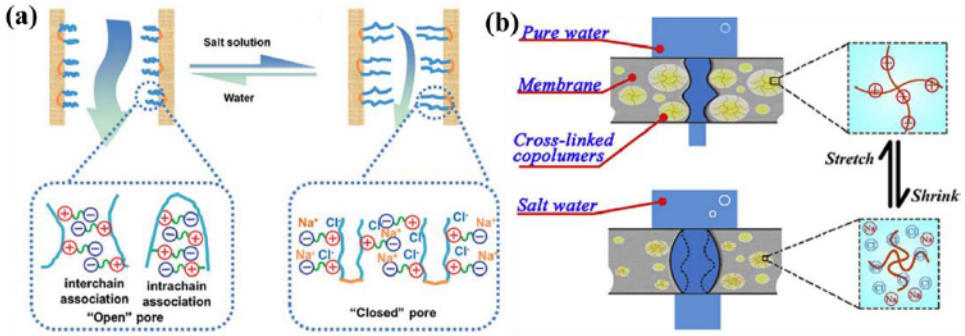

Figure 5. (a) A schematic illustration of conformational changes of the pore of PES/PES-*b*-PSBMA blend membrane in the presence of deionized water and salt solution. Reproduced from [32] with permission from Elsevier. (b) Schematic illustration of the ion strength responsive behavior of PES membranes modified by PILs. Reproduced from [33] with permission from Elsevier.

I.III.IV. Glucose-responsive porous membranes

Since diabetes is a major cause of death in the world, developing glucose-responsive, insulin-releasing systems for diabetes treatment has become more and more important. Among the many systems, glucose-responsive membranes are a good choice for combined stability and

responsiveness. For example, Chu *et al.* grafted poly(acrylic acid) (PAAC) and immobilized glucose oxidase (GOD) onto polyvinylidene fluoride (PVDF) porous membrane to fabricate glucose-responsive porous membrane (34). When placed in water in absence of glucose, because of electrostatic repulsion between the negatively charged carboxyl groups of the PAAC chains, they tend to extend and drive membrane pores to close, preventing the release of insulin. However, with the increase of glucose concentration in water, the GOD can transform the glucose into gluconic acid, decreasing the pH and thus protonating the carboxylate groups to make the extended PAAC chains turn to collapsed state. Consequently, the membrane pores are open to allow the release of insulin (Figure 6).

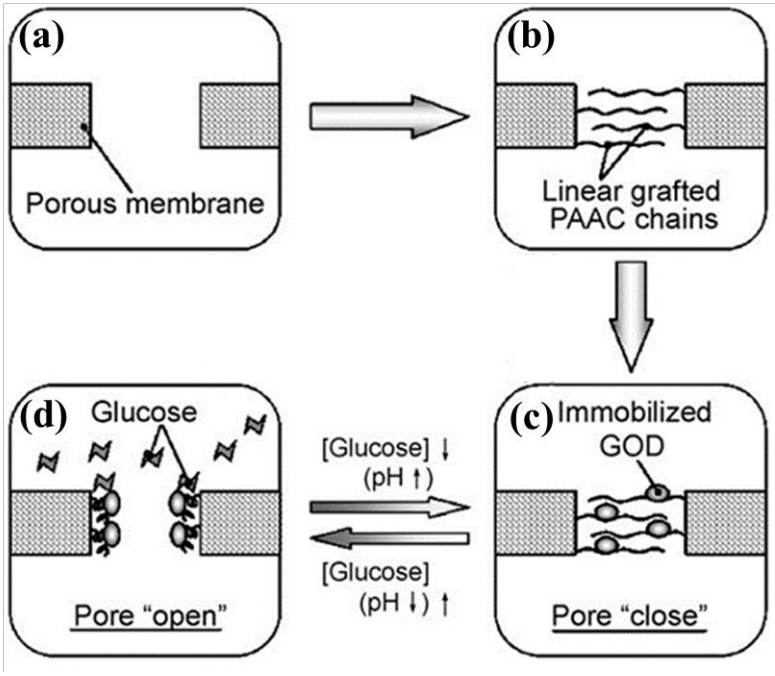

Figure 6. Schematic illustration of the fabrication process of glucose-responsive PVDF porous membrane modified by PAAC and GOD (a and b) and the mechanism of glucose-responsive behavior (c and d). Reproduced from [34] with permission from Elsevier.

I.III.V. Photo-responsive porous membranes

Among the various stimuli, light is a special and attractive choice, since it allows fast and

remote-controlled effect on physical/chemical properties of materials with no risk of chemical contamination and can be easily focused on the well-defined areas (35).

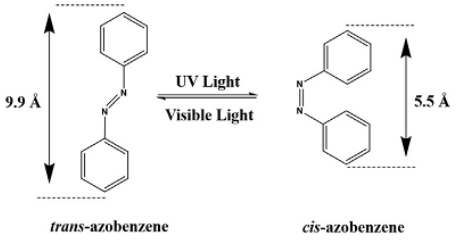

Figure 7. *Trans-cis* photoisomerization and resulting shape change of the azobenzene. Reproduced from [36] with permission from Elsevier.

Azobenzene is a typical photochromic group that can easily and rapidly undergo reversible photoisomerization (37). As shown in Figure 7, in response to the UV light, azobenzene changes from *trans*- to *cis*- configuration, decreasing the distance between the *para* carbon atoms (from 9.9 Å to 5.5 Å), and the increasing the dipole moment (from 0.5 D to 3.1 D) (36-38). This photoisomerization is reversible, and the *trans*-azobenzene can be reformed upon visible light absorption or heating. Different kinds of azobenzene-based materials have been employed to functionalize the membrane surface in order to modulate the surface wettability and permeability under UV light (39-42). For example, Anzai *et al.* reported a photoresponsive poly(vinyl chloride) (PVC) membranes containing azobenzene-modified crown ethers for ions permeation (43). Before UV light irradiation, the permeability of the membranes for the alkali cations follow an order of $K^+ > Rb^+ > Na^+ > Cs^+$. Upon UV light irradiation, the permeability of the K^+ is significantly increased while the permeability of the other cations almost has no changes. Therefore, this membrane can selectively accelerate passage of the K^+ by using UV light as a driving force. Lin *et al.* reported a photoresponsive, self-cleaning membrane by co-depositing 4,4′-azodianiline (AZO) and polydopamine (PDA) on the surface of ultrafiltration (UF) membranes (Figure 8 (a)) (36). By adjusting UV/visible light irradiation, the photoisomerization of AZO results in the decrease/increase of volume of PDA/AZO layer, which alleviates the aggregation of the contaminations on the membrane surface (Figure 8 (b)).

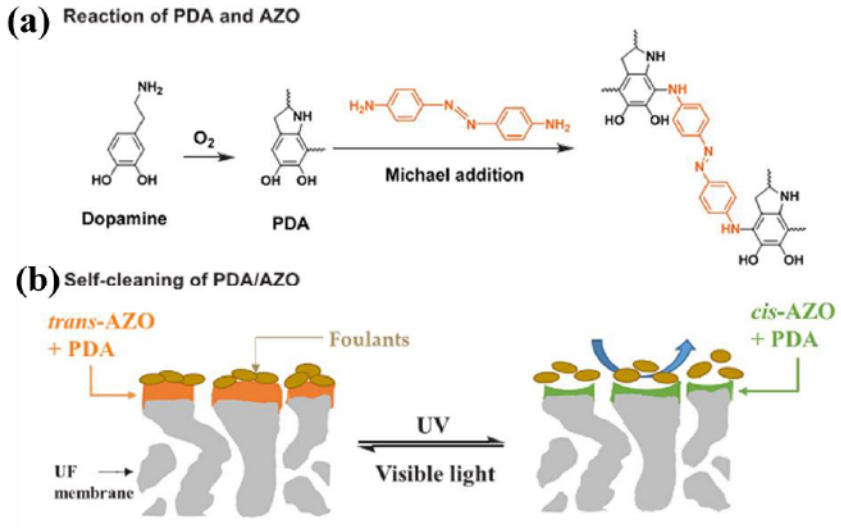

Figure 8. Scheme of Michael addition reaction between AZO and PDA (a). (b) Self-cleaning behavior of a photoresponsive UF membrane modified by AZO and PDA. Reproduced from [36] with permission from Elsevier.

Spiropyran (SP) is another mostly studied photochromic group. Upon absorption of UV light, SP can undergo a heterolytic ring cleavage from the hydrophobic SP to a hydrophilic and zwitterionic merocyanine (MC) isomer. After the visible light irradiation, the MC can recover to the initial SP state through a ring-closing reaction (Figure 9) (44). When incorporated into membranes, the photoisomerization of SP endows membranes with photocontrolled solvent permeability, self-cleaning and surface wettability. Chung *et al.* grafted copolymers of spiropyran-containing methacrylate (SPMMA) and acrylamide (AAm) onto polytetrafluoroethylene (PTFE) porous membranes to achieve photocontrolled permeability (45). The permeability of H_2O/CH_3OH mixture for this membrane was studied by applying UV/visible light irradiation. Different from PAAm-modified PTFE membranes, for which light has very little effect on permeability, the permeability of poly(SPMMA-*co*-AAm) modified PTFE membranes could sharply increase under UV irradiation before decreasing under visible light irradiation. The variation of permeability is attributed to polarity change between SP and MC. With UV light,

MC groups are generated, which makes the SPMMA become hydrophilic. Since the hydrophilic SPMMA chains have low solubility in a H_2O/CH_3OH mixture, the grafted chains are collapsed to open the membrane pores and thus increase the permeability. When exposed to visible light, the hydrophobic SP increases the grafted chains' solubility in H_2O/CH_3OH mixture, and the polymer chains with extended conformation close the membrane pores and decrease the permeability.

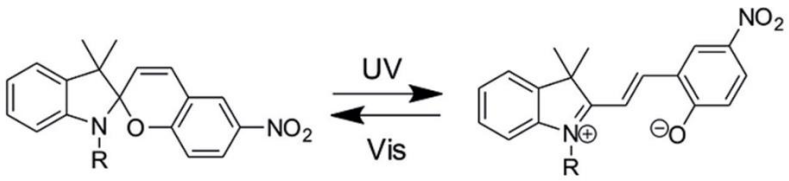

Figure 9. Reversible photoisomerization between spiropyan (SP) and zwitterionic merocyanine (MC). Reproduced from [44] with permission from American Chemical Society.

In another study, Belfort *et al.* grafted vinyl SP onto PES UF membranes to demonstrate photoswitchable membrane surface (Figure 10) (46). By alternating UV/visible light irradiation, the reversible changes of membrane surface wettability can be achieved. When exposed to UV light, the contact angle of the modified membrane decreases due to the hydrophilicity of generated MC groups, resulting in low adsorption of bull serum albumin (BSA). Followed by visible light irradiation, the contact angle increases due to the hydrophobicity of generated SP groups, leading to high adsorption of BSA. Asatekin *et al.* synthesized a comb-shaped graft copolymer containing polyacrylonitrile (PAN) backbones and SP side chains (47). They used this copolymer as the coating for porous support membrane to prepare self-cleaning membrane. By alternating UV/visible light irradiation, the membrane shows fast and reversible removal of BSA because of the presence of the copolymer coating. This copolymer shows a great potential in self-cleaning coatings for solving fouling problem of surfaces prone to organic.

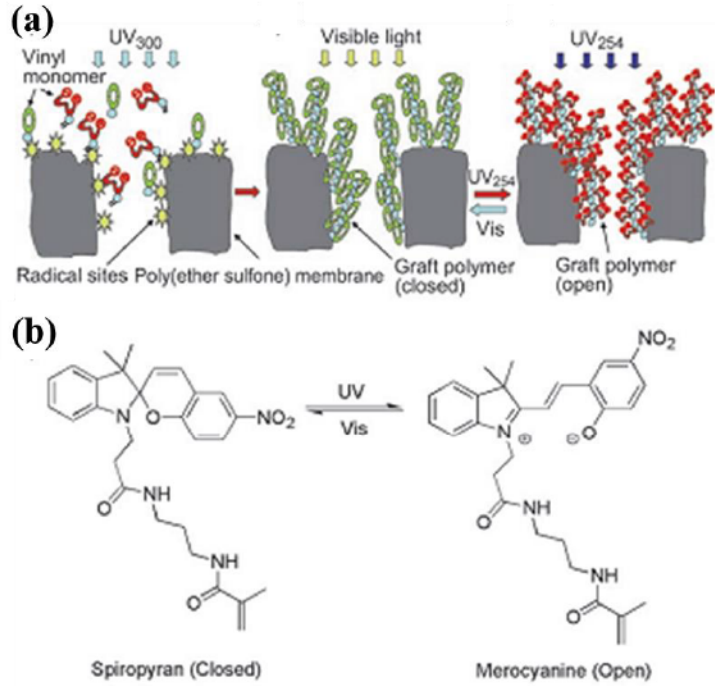

Figure 10. (a) Scheme of the fabrication process of SP-grafted PES porous membrane and the mechanism of reversible photo-switchable membrane surface. (b) Chemical structure changes of the vinyl SP in response to UV and vis irradiation. Adapted from [46] with permission from John Wiley and Sons.

Besides the photoisomerization reactions, photothermal effect has been the basis of another effective method for photoresponsive porous membranes. Generally, such responsive porous membranes are prepared with thermosensitive polymers loaded with photothermal agents. Upon exposure to light, the photothermal agents can convert the light energy into thermal energy, leading to the phase transition of thermosensitive polymers. This can drive the polymer chains to undergo the reversible shrinking/swelling, thus controlling the variation of membrane pore size. Ramírez *et al.* prepared a photothermal responsive porous membrane by grafting PNIPAM-AuNP nanocomposites onto polycarbonate track-etched porous membranes (PCTEPMs) (48). Under the yellow light irradiation, due to excellent light-heat conversion of AuNP, the PNIPAM chains change from the extended state to the collapsed state, opening the membrane pore to increase water flux. When switching off light, the PNIPAM chains recover

to the extended state, closing the membrane pore to decrease water flux. Jin *et al.* also used photothermal effect to prepare photo-responsive ultrathin membrane for switchable separation of oil/water nanoemulsion (49). The fabrication and photothermal-responsive behavior of this membrane is illustrated in Figure 11 (a). This membrane was fabricated in the following four steps: (1) design of the PDA modified single-walled carbon nanotube (SWCNT), (2) fabrication of the PDA-coated SWCNT membrane, followed by decoration of (3) poly(N-isopropylacrylamide-*co*-acrylamide) (pNIPAm-*co*-AAm) and (4) excess AuNRs. This membrane can be used for separating oil/water nanoemulsions with ultrahigh efficiency (> 99.99%) and a maximum permeate flux up to 35890 $m^2 \cdot h^{-1} \cdot bar^{-1}$ due to their nanometer pore sizes, hydrophilicity as well as underwater oleophobicity. Moreover, the permeate flux can be easily modulated by alternating light irradiation because of the presence of thermal-responsive copolymers and AuNPs. Another photothermal responsive porous membrane was reported by Cheng *et al* (50). This membrane was consisted of PNIPAM covalently bound to graphene oxide (GO) *via* free-radical polymerization (Figure 11 (b)). Upon alternating NIR light on and off, PNIPAM undergoes reversible shrinking/swelling transition to modulate the spaces of the GO layers, thus reversibly regulating the water permeability. Because of this space tunability, such membrane can gradually separate multiple molecules with different sizes. It should be noted that different from the membrane that can open and close the pores by turning off and turning on light irradiation, respectively, the PNIPAM-grafted GO membrane exhibits the opposite switching behavior. The reason is that there are two types of PNIPAM chain termination. In one case, the two ends of PNIPAM chain are connected two GO layers, while in the other case, only one end of PNIPAM chain is grafted onto GO layer. When exposed to NIR light, the first PNIPAM chain termination can pull two adjacent GO layers closer due to the polymer chain contraction. With only one chain end grafted, the distance between two adjacent GO layers is decreased due to the PNIPAM chains entanglement. Both forms play important roles in reversibly tuning space of GO layers, which endows the membrane with negatively photothermal-response behavior.

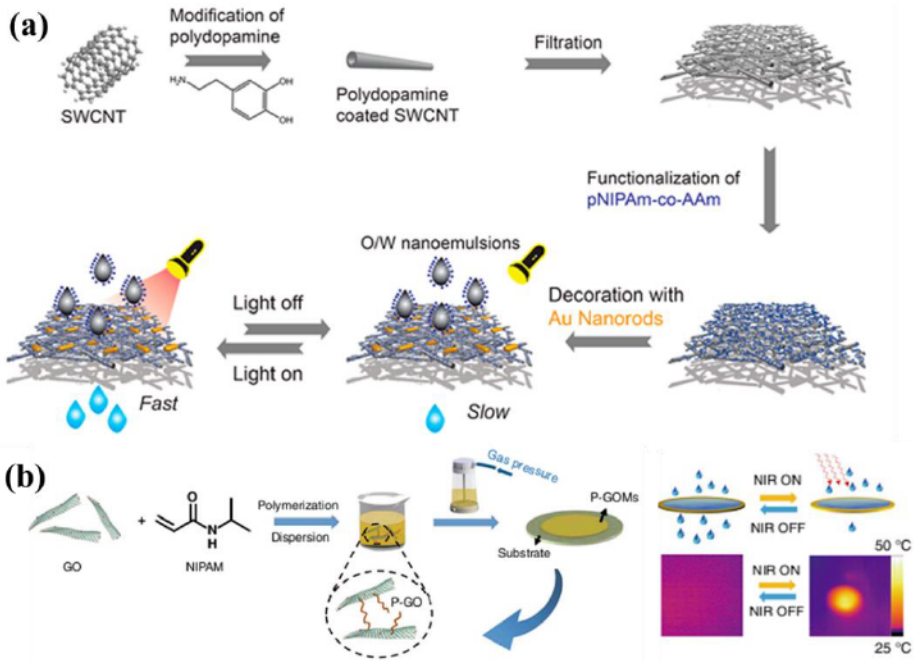

Figure 11. Scheme of the fabrication process of (a) photothermal-responsive AuNR/pNIPAm-*co*-AAm cohybrid SWCNT ultrathin membranes, and (b) PNIPAM-grafted GO membranes and the corresponding photothermal-responsive behavior. Reproduced and adapted from [49] and [50] with permission from American Chemical Society and Springer Nature, respectively.

I.III.VI. Magnetic-responsive porous membranes

Similar to the photothermally driven porous membranes, the magnetic field-responsive porous membranes also have the advantages of spatiotemporal and remote control (51). Generally, the magnetic field-responsive porous membranes contain magnetic nanoparticles such as iron oxides (e.g., Fe_3O_4) and thermoresponsive polymers. Due to high heating efficiency of these magnetic nanoparticles, they can generate heat under an alternating magnetic field (AFM), to remotely open or close membrane pores. Ulbricht *et al.* fabricated track-etched polyethylene terephthalate (PET) membranes embedded with the Fe_3O_4 nanoparticles, which subsequently was modified by the thermoresponsive PNIPAAm (Figure 12 (a)) (52). The effective pore size of this membrane can be modulated from 290 nm to > 400 nm by the magnetic field because of the synergy between the Fe_3O_4 nanoparticles and the PNIPAAm, which allows for effective

switching of the water flux. Subsequently, they reported another two magnetic field-responsive porous membranes for switchable molecular sieving (Figure 12 (b and c)) (53, 54). In these membranes, the magnetic nanoparticles and PNIPAAm hydrogels act as localized heater and the sieving medium, respectively. By switching on and off the external AMF, these membranes exhibit large and reversible changes of water flux. Additionally, the molecular weight cutoff of these membranes can be reversibly tuned from 70 to 1750 kDa by switching off or on the external AMF.

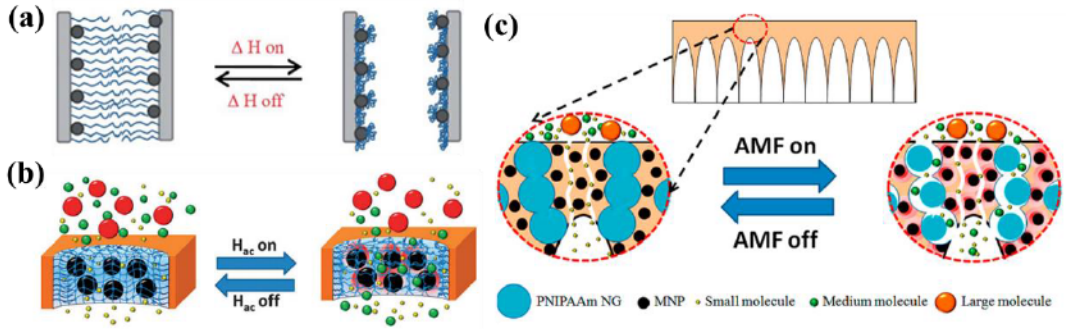

Figure 12. (a) Schematic illustration of reversible change of pore size of PET membrane embedded with Fe_3O_4 and PNIPAAm under magnetic field. Reproduced from [52] with permission from The Royal Society of Chemistry. (b) Scheme of magneto-responsive separation membrane based on iron oxide and PNIPAAm hydrogel. Reproduced from [53] with permission from The Royal Society of Chemistry. (c) Scheme of anisotropic magneto-responsive PES ultrafiltration membrane based on iron oxide and PNIPAAm hydrogel. Reproduced from [54] with permission from American Chemical Society.

I.III.VII. Electric-responsive porous membranes

Electric field-responsive porous membranes have drawn much scientist's attention since electrical fields can be rapidly and easily employed to the membrane separation systems in a large area, which can enhance the convenience of system operation. Elabd *et al.* studied the electric field-responsive permeability of polyelectrolyte gel functional polyester track-etched (PETE)

membranes (55). They used poly(2-acrylamido-2-methyl-1-propanesulfonic acid) (PAMPS) as polyelectrolyte gel to modulate the pore sizes and permeability. Without voltage, the membrane is almost impermeable due to swelling of PAMPS gel on the membrane surface and in the pores (Figure 13 (a)). With voltage applied, the PAMPS gel asymmetrically contract, leading to increase in permeation. Liu *et al.* applied the electrically induced reversible reactions between ferrocene (Fc) and *β*-cyclodextrin (*β*-CD) into PTFE membranes to achieve electrically driven biofouling release (56). The PTFE membrane was firstly modified with polymer chains containing Fc groups and then cross-linked with a difunctional *β*-CD compound through the complexation reaction between Fc and *β*-CD (Figure 13 (b)). Through the electrically induced reversible complexation/decomplexation behaviors of Fc/CD, the surface layer of the functional PTFE membrane displays reversible protein detachment.

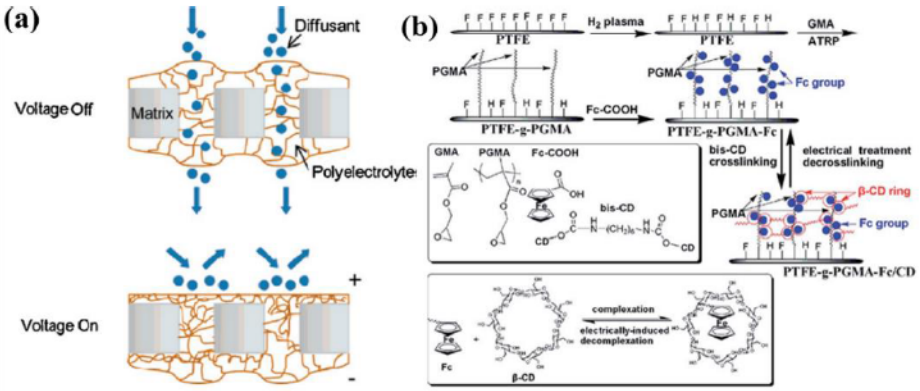

Figure 13. (a) Scheme of electric-responsive permeability of PAMPS gel-*g*-PETE nanocomposite membranes. Reproduced from [55] with permission from American Chemical Society. (b) Scheme of the fabrication process and mechanism of the electric-responsive PTFE-*g*-PGMA- Fc/CD membrane. Reproduced from [56] with permission from American Chemical Society.

I.III.VIII. CO_2-responsive porous membranes

Recently, the stimulus of CO_2 has gained increasing attention for the development of smart materials and systems. Compared with the other stimuli, CO_2 is “green” and easy to add or

remove in large volume operations, which has showed great interest in biomedical and industrial applications (57-60).

Yuan *et al.* used the electro-spinning process to prepare CO_2-responsive nanofibrous porous membranes from poly(methylmethacrylate)-*co*-poly(*N*, *N*-diethylaminoethyl methacrylate) (PMMA-*co*-PDEAEMA) copolymers, which can switch the surface oil/water wettability under the stimulation of CO_2 (Figure 14) (61). Initially, the membrane is hydrophobic and allows the oil in oil/water mixture to go through the membrane. Under the stimulation of CO_2, the membrane is changed from the hydrophobic to the hydrophilic state, thus only water can pass through the membrane. This CO_2-switchable membrane can be used as dual oil/water on-off switches. Feng and Billon's group fabricated CO_2-responsive honeycomb porous membranes from polystyrene-*b*-poly(*N*, *N*-dimethylamino ethyl methacrylate) (PS-*b*-PDMAEMA) (62). They find that hydrophilic PDMEAEMA segments determine the pore sizes, porous layers and regularity on surfaces. Because of the protonation/deprotonation of tertiary amine groups by injecting CO_2 or heating to remove CO_2, the membrane surface can undergo a reversible transition between hydrophilicity and hydrophobicity. Such porous membranes are potentially good candidates for cell scaffolds.

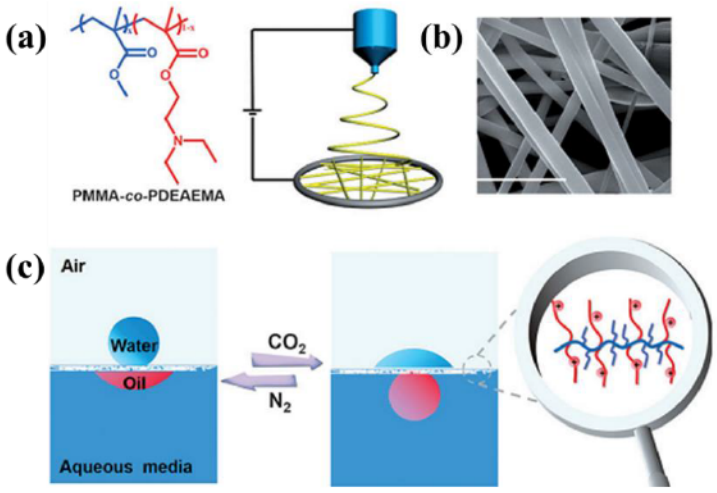

Figure 14. (a) Illustration of the fabrication of PMMA-*co*-PDEAEMA nanofibers through electro-spinning process. (b) SEM images of the fabricated CO_2 responsive porous membranes. (c)

Illustration of the CO_2-tunable oil/water. Reproduced from [61] with permission from John Wiley and Sons.

Recently, Theato *et al.* reported a crosslinked CO_2-responsive nanofibers membrane based on photo-cross-linked poly(pentafluorophenyl acrylate) (PPFPA) (63). The prepared PPFPA nanofibers were further modified by histamine to obtain cross-linked poly(histamine acrylamide) (PHAAA) nanofibers showing a CO_2 responsiveness (Figure 15). Under cyclic addition and removal of CO_2, the wettability of membrane surface can be reversibly tuned from hydrophobic to hydrophilic state, which can realize reversible absorption and release of BSA.

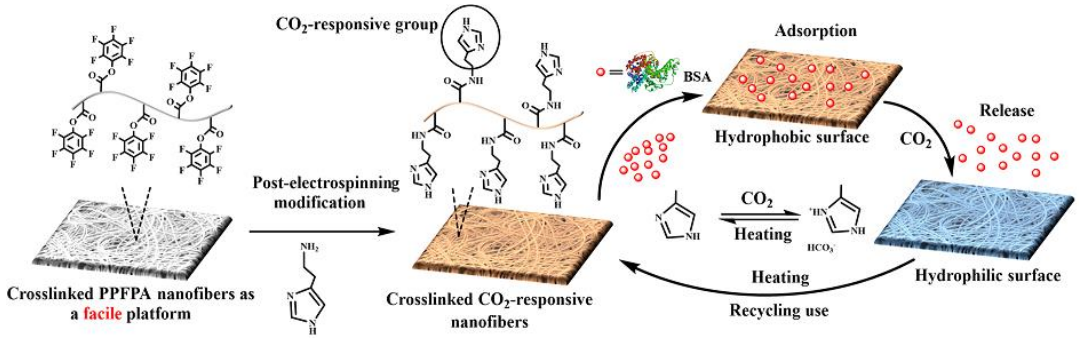

Figure 15. Illustration of the fabrication of cross-linked CO_2-responsive nanofibers through post-electrospinning modification and the CO_2 switched absorption and release of BSA. Adapted from [63] with permission from American Chemical Society.

II. Stimuli-responsive Polymer Actuators

(Note: The following parts mainly derive from my Review paper which has been published in *Materials Chemistry Frontiers,* 2018, DOI: 10.1039/C8QM00363G.)

In plants and animals, environmental changes can drive complex shape transformations including opening of pine cones (64), trap closure of carnivorous plants (65), and octopus adaptive-camouflage skin shape changes (66). Mimicking environmental responsiveness of living or-

ganisms has been a fascinating yet challenging research area for decades. So far, stimuli-responsive polymer actuators that can change shape or undergo motion in response to external stimuli have drawn broad attention in designing artificial muscles (67, 68), soft robots (69-72), cell scaffolds (73), reconfigurable devices (74), and micromanipulators (75). Among them, photo-responsive polymer actuators are especially attractive since light allows for remote and localized actuation of the polymers without the need to change their surrounding environment (76, 77).

Traditional photo-responsive polymer actuators mainly rely on the reversible *trans-cis* photoisomerization of azobenzene (AZ) derivatives stimulated by UV and visible light (78). In particular, liquid crystal polymers (LCPs) containing AZ mesogens are the most studied polymer actuator systems (79, 80). While trans-AZ is in a rodlike shape and compatible with the ordered LC phase, cis-AZ is in a bent shape and tends to destabilize the LC phase. Under UV irradiation, the change in molecular configuration of AZ mesogens upon *trans-cis* isomerization can lead to LC-isotropic phase transition and, consequently, drives the polymer to exhibit macroscopic deformation and related motions, such as rolling (81-83), bending (79, 84, 85), walking (86, 87), twisting (88), and oscillating (89-91). Although these photoinduced transformations are important achievements, UV light may not be the right stimulus for certain applications, especially for biomedical applications as UV light has limited tissue penetration depth and can be damaging to healthy cells (92). In this regard, longer-wavelength visible and near-infrared (NIR) light is more suitable. Besides, the number of photochemical reactions useful for effective polymer actuator applications is limited; and like for any photosensitive materials relying on a photochemical reaction, the long-term stability is always an issue due to side reactions and photodegradation. These concerns push researchers to look at alternative approaches to developing light-driven polymer actuators. In recent years, visible or NIR light induced photothermal conversion has emerged as a promising strategy for photo-responsive polymer actuators due to not only the wavelength-enabled biocompatibility and high tissue penetration abilities, but also the ease and flexibility in designing the materials. However, it

should be mentioned that AZ derivatives are also dyes and the photothermal effect can play an important role in some LCP actuators with AZ mesogens. Moreover, AZ derivatives with visible light driven trans-cis photoisomerization have been developed to address the wavelength issue (93, 94).

II.I. Photothermally-driven liquid crystal polymer actuators

Liquid crystals are the materials which greatly impact our daily life. They exhibit the dual-characteristics of the fluidity of an isotropic liquid and the molecular order of a crystalline solid (95-98). When incorporated into a polymer structure, referred to as mesogens, either in the chain backbone or as a side groups, they may give rise to liquid crystal polymers. For the purpose of actuator applications, LCPs need to be crosslinked, either as liquid crystal elastomers (LCEs) or liquid crystal networks (LCNs). Generally, LCEs are lightly crosslinked, contain side-chain or main-chain mesogenic units, and have a flexible chain backbone (*e.g.*, polysiloxane) (99, 100).

These polymers usually have a low glass transition temperature, T_g, below room temperature and behave similarly to traditional rubbers. By contrast, LCNs are moderately to densely crosslinked, usually obtained by polymerization of oriented LC monomers (*i.e.*, reactive mesogens). LCEs and LCNs have become a particularly promising material system for polymer actuators thanks to their ability to exhibit large reversible shape change upon the LC (order)-isotropic (disorder) phase transition. Figure 16 shows the basic principle behind this remarkable property. What is required is to have a specimen in which the mesogens are oriented in the absence of external stress. The monodomain of uniaxial orientation in the illustration can easily be obtained using generally a rubbed surface or mechanical stretching, with mesogens aligned along the rubbing or strain direction. Polymer chains in the macroscopically oriented LC phase have an anisotropic, elongated conformation; once heated above the LC-isotropic phase transi-tion temperature ($T_{lc\text{-}iso}$), the mesogens lose their orientation and become randomly aligned, which brings polymer chains back to the random coil conformation. Accompanying the LC-isotropic

phase transition, the specimen contracts along the initial orientation direction but expands in the perpendicular directions. When the LCE or LCN is cooled into the LC phase, below $T_{lc\text{-}iso}$, the mesogens recover spontaneously the orientation and the shape of the specimen goes back to the original state. back to the original state.

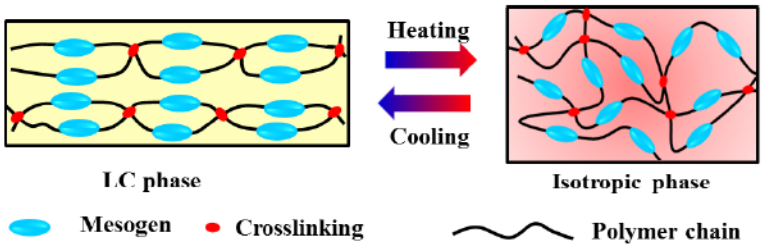

Figure 16. Schematic illustration of the reversible macroscopic shape change of crosslinked liquid crystal polymers (LCPs) with monodomain of oriented mesogens caused by liquid crystal (order)-isotropic (disorder) phase transition.

Since the reversible shape change is governed by the reversible LC-isotropic phase transition, LCEs and LCNs can readily be transformed into light-driven actuators using the photothermal effect. As compared to direct bulk heating, using light to control the LC-isotropic phase transition enables localized heating and thus actuation in spatially selected regions, which can be controlled remotely and switched on/off rapidly (92). To achieve effective photothermally-driven actuation, in principle, LCPs can be loaded with a variety of photothermal agents, often in the form of nanofillers, which include carbon nanotubes (92, 101-111), graphenes (112-115), metal nanoparticles (87, 116-120), organic or organo-metallic dyes (78, 121-132) and conjugated polymers (133). They can absorb visible and/or NIR light and convert optical energy into thermal energy by releasing heat into the polymer matrix to trigger the LC-isotropic phase transition. The choice of the photothermal agent should be made based on the targeted application of the actuator and by taking into consideration a number of general issues. First, the added photothermal agent determines the absorption wavelengths. For example, if the actuator device is aimed at biomedical applications, it should be driven by NIR light. In this case, either

gold nanorods or carbon nanotubes or graphene or NIR dyes can be used. Secondly, the photothermal agent should be effective, meaning that it has a high molar extinction coefficient and high quantum yield of optical-thermal energy conversion. With a highly effective photothermal agent, a tiny amount can be enough to increase the temperature above the LC-isotropic phase transition, which may be beneficial for certain applications. Thirdly, the photothermal agent should be well dispersed in the LCP matrix, which generally necessitates surface functionalization of the inorganic nanofillers with appropriate (polymer) ligands. In cases where the compatibility is problematic due to limited compatibility between the polymer and the nanofiller, incorporating an organic dye directly in the LCP structure may be the ultimate solution (78, 123, 125, 130-132). Fourthly, if the transparency and color of the LCP actuator is an issue, judicious choice of the photothermal agent may resolve the problem. For example, using an NIR dye that absorbs little in the visible light region, a transparent actuator is feasible.

On the other hand, the choice or design of a particular LCE or LCN is also important because its thermal phase transition temperatures, T_g and $T_{lc\text{-}iso}$, can impact the shape change or motion behaviors in the light-on and light-off state. Generally speaking, the LC-isotropic phase transition should not occur at very high temperatures, say, 150 ^oC, because it means that high content of a photothermal agent or high excitation light intensity (or power) is required to heat the polymer above $T_{lc\text{-}iso}$ for actuation. However, the phase transition temperature should not be too close to room temperature either, because the polymer cooling upon turning off light may be slow, leading to slow shape recovery and thus slow motion of the actuator. As for T_g, LCEs require a low T_g below room temperature so that the polymer can be deformed under ambient conditions to obtain LC orientation (a second chain crosslinking may be necessary to retain the monodomain). But with comparable crosslinking density, low T_g usually means weak mechanical strength (hardness). A potential problem for high-T_g LCNs is that once light is turned off, the polymer is cooled below T_g too fast to allow complete shape recovery to occur because of the lost chain mobility in the glassy state. All of the above issues may need to be considered when building a photothermally-driven LCP-based actuator.

II.I.I. Actuation modes

The reversible shape change of LCP-based actuators depends on the configuration of the macroscopic LC orientation (134). For the sake of clarity, the uniaxial orientation in Figure 16 will be used as an example to explain the basic actuation modes knowing, however, that more complex LC orientation states such as twisted, splayed and hybrid LC directors can be prepared to generate more complex shape changes upon the LC-isotropic phase transition (112, 113, 121, 122, 126). As shown in Figure 16, when a strip LCP actuator of monodomain is uniformly heated above $T_{lc\text{-}iso}$ and then cooled back to the LC phase, the shape change is simply contraction/extension along the LC orientation direction. However, if the actuator is converted to be photo-thermally driven by light, the shape change of the strip is different due to light absorption characteristics and spatially selective light exposure. What follows is a discussion of some basic shape morphing, referred to as actuation modes, of photothermally-driven LCP actuators.

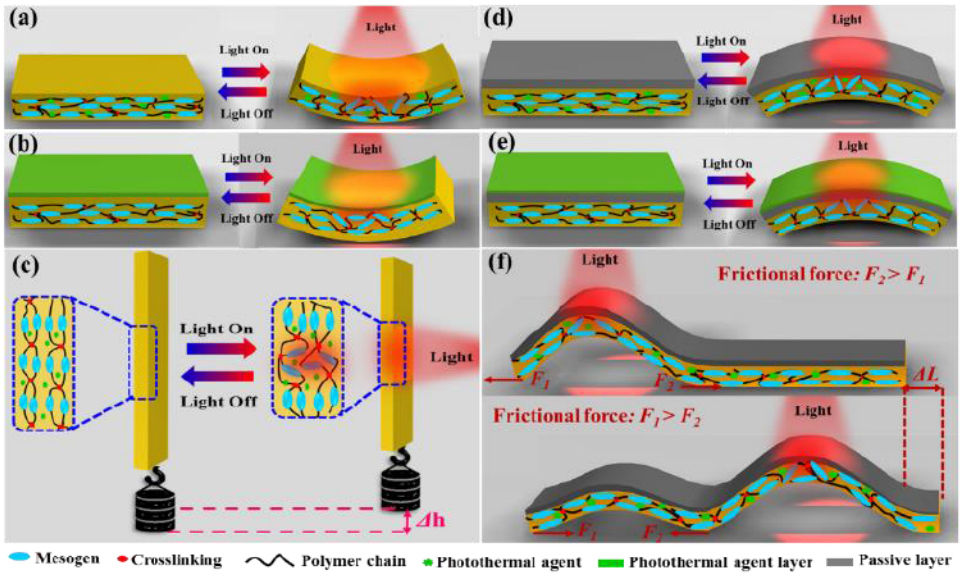

Figure 17. Actuation modes of photothermally-driven LCP actuators. (a and b) Reversible bending toward the light source. (c) Reversible contraction under a load. (d and e) Reversible bending away from the light source. (f) Light-driven locomotion. For the actuator design: in (a), a photothermal agent is dispersed in the LCP matrix; in (b), a thin layer of a photothermal agent is deposited on the LCP; in (d), a passive layer is on (a); and in (e), a passive layer is

between the photothermal agent layer and the LCP layer.

The first and most general actuation mode is reversible bending toward the light source followed by unbending when the light is off (Figure 17a). Upon light irradiation on one side of the strip actuator, the dispersed photothermal agent absorbs light and releases heat to increase the temperature of the illuminated area above $T_{lc\text{-}iso}$. Due to the light attenuation, the heating along the thickness direction is not uniform and a decreasing temperature gradient exists within a certain period of time, on the order of tens of seconds depending on the conditions. As a result, the LC-isotropic phase transition only takes place in the top surface region, resulting in an imbalanced contraction force that bends the strip toward the light source. After removal of the light, the temperature of the illuminated area may drop quickly into the LC phase, which unbends the strip due to extensional force arising from isotropic-LC phase transition (75, 87, 101, 106, 135). Nevertheless, it should be noted that long time irradiation can also drive the bended actuator to gradually unbend, as a result of uniform heating across the thickness that can be attained after long time irradiation (106). In other words, bending actuation toward the light source requires a temperature gradient for partial LC-isotropic phase transition from one side to the other along the specimen thickness. This can also be obtained by depositing a thin layer of a photothermal agent on the surface side exposed to light (Figure 17b). This approach is particularly useful if a uniform dispersion of the photothermal agent is difficult to achieve.

The second actuation mode is reversible contraction/extension, under a load (Figure 17c). In this case, when the light is applied, the bending tendency of the actuator shortly under irradiation is inhibited due to the presence of the external force that keeps the strip straight. After the temperature gradient along the thickness direction in the illuminated area disappears as the irradiation goes on, the actuator shows uniform contraction and reaches the maximum contraction within a certain period of time. Once the light is off, the actuator extends and recovers to the original length after removal of or turning off the light. This actuation mode is often used to demonstrate the conversion of optical energy into physical work. By varying the load, which can be many times the weight of the LCP actuator, this actuation mode can also be used to

estimate or appreciate the magnitude of the contraction force optically generated upon the LC-isotropic phase transition. Of course, even for free LCP actuators (without load), if the specimen is sufficiently thin and exposed to high intensity light, a uniform heating across the thickness to $T>T_{lc\text{-}iso}$ may be obtained quickly so that the contraction/extension mode is observed.

The third actuation mode is reversible bending away from the light source, i.e., the central region of the strip actuator ascends toward the incident light, which is followed by unbending after the light is off (Figure 17d and e). As will be shown further on, this type of shape change is particularly important for light-driven locomotion of LCP actuators. There are different ways to make the actuator bend away from the light source. With uniaxial orientation of an LC director, it requires a sort of bilayer structure: one active layer that is LCE or LCN and one passive layer that is a transparent polymer and that is exposed to light. Such a passive layer can be bound to an LCP actuator with dispersed photothermal agent (Figure 17d) or to an LCP actuator coated with a thin layer of a photothermal agent (Figure 17e). In both cases, if the relatively hard passive layer has an appropriate thickness, when the actuator undergoes photothermally induced LC-isotropic phase transition and tends to contract, the constant length of the passive layer and its interface with the active layer will result in bending away from the light source. Of course, actuators of this kind with multilayer structures can be built to display different bending behaviors, but the above discussion covers the basic bending modes of photothermally-driven actuators of LCEs or LCNs.

Although LCP actuators with uniaxial LC orientation are used for the discussion, it should be noted that the bending actuation can readily be controlled by programming the alignment of the LC director field in LCEs or LCNs using the reactive mesogen approach. For example, under light irradiation, the splay LC orientation can lead to non-uniform expansion/contraction at the two opposite sides of the strip actuator, which drives the strip to bend towards or away from the light source depending on which side is exposed (123, 126, 131, 136, 137).

Light-driven motions such as locomotion and oscillation represent a more advanced class of

actuation that can be explored to mimic certain movements of plants or living species in nature. In this regard, photothermally-driven, LCP-based actuators are particularly promising. Figure 17f depicts how to obtain laser-driven worm-like motion using a strip actuator that bends away from the laser. Upon light irradiation, the left side of the strip ascends by bending, which displaces the left end to the right. As the laser moves forward to the other end, the initial bump tends to flatten due to cooling-induced extensional force and the dragging down effect by the new bump formed on the right side. If the left end bears a larger friction with the substrate surface than the right end, it will act as a stationary end and repeated scanning of the laser can thus drive the strip to move from left to right.

II.I.II. Comparison of photothermal agents

As discussed above, in principle, any species that has a strong photothermal effect (high light absorption and high quantum yield of photothermal conversion) can be utilized with LCEs or LCNs for fabricating light-driven polymer actuators. In practice, however, various issues need to be considered according to what should be achieved in the targeted application. Consequently, the number of frequently used photothermal agents in LCP actuators is limited. Since an ideal photothermal agent would be one that is so effective that even with a small amount and a low-intensity light irradiation, a high temperature can be obtained very quickly. What follows is an attempt to compare the efficiency of the various photothermal agents through a survey of the studies reported in the literature. This comparison, unfortunately, turns out to be very difficult to do, because it is simply not possible to compare the different studies in a straightforward manner. For example, even at the same concentration with the same type of photothermal agent, the actual dispersion state in the LCP can be different, which affects the light absorption and heat release. Even with the same amount of heat released, the used LCPs may differ in heat capacity and thermal conductivity, which influences the temperature rise in the irradiated area. Nevertheless, in order to give readers an idea about the choice of most used photothermal agents and a general appreciation of their performance, we show in Table 1 a comparison of the relevant properties reported in a number of publications (not an exhaustive

list).

Some general trends can be noticed from Table 1. For the same photothermal agent, the concentration in LCE or LCN plays an important role in the attainable temperature and the temperature rising speed of prepared actuators under light irradiation. The larger the concentration, the higher maximum temperature and faster speed can be achieved under light irradiation. The same can be said for the light irradiation intensity. At the same photothermal agent concentration, increasing the light intensity has as effect to increase the temperature higher and faster. On the other hand, because most photothermal agents are inorganic materials (e.g. CNT, GO and Au nanoparticles), they inevitably have poor compatibility with organic LCPs, which limits their concentration in the polymer actuators. It can be seen from Table 1 that the usually used concentrations are low. Compared with them, the organic photothermal agents, such as dyes, polydopamine (PDA) and conjugated polymers, can usually afford relatively high concentrations due to good compatibility with LCPs. Of course, if the photothermal agent is part of the LCP structure, the compatibility is no longer an issue. A striking example was demonstrated by Yang's group (125). They designed and synthesized an LCE actuator bearing chemically bound NIR dye with a concentration up to 17.06 wt%. Owing to the high content of the photothermal agent, the surface temperature of their LCE actuator could jump over $T_{lc\text{-}iso}$ (116 ^{o}C) in 2 s and reach 260 ^{o}C within 8 s, exhibiting ultrafast photo-responsive speed. This actuator also shows superior mechanical properties by lifting up 5680 times its own weight upon NIR light induced contraction (Figure 18).

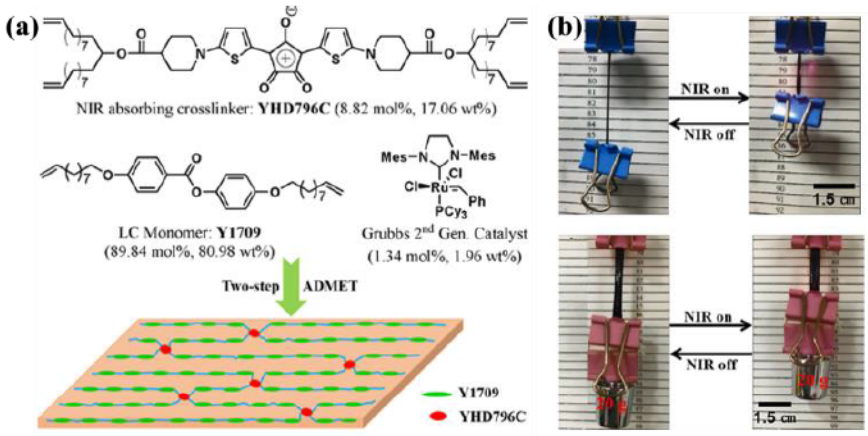

Figure 18. (a) Chemical composition of LCE actuator with chemically bonded NIR light absorbing chromophore. (b) Photos showing a LCE film lifting up a binder clip and load under NIR light illumination. Reproduced from [125] with permission from American Chemical Society.

If an inorganic photothermal agent has a very high molar extinction coefficient and quantum yield of photothermal conversion, it can also endow the LCP actuator with fast photothermal-response even at an extremely low concentration. This is the case of gold nanoparticles (AuNPs) and nanorods (AuNRs). For example, our group recently demonstrated an LCP actuator loaded with AuNRs (87). Despite the very low AuNR concent ration (0.05 wt%), the actuator still shows excellent photothermal response with the temperature rising to 175 ºC in less than 40 s under NIR light irradiation.

Also shown in Table 1 is that in addition to dispersing photothermal agents in LCEs or LCNs, bilayer or trilayer structures are another effective method to design actuators. In this case, the photothermal agents (e.g. GO or PDA) form a thin layer on the surface of the LCP strip, and the released heat under light irradiation can increase the temperature of one side of the actuator (at the interface) quickly above $T_{lc\text{-}iso}$ (*e.g.*,within seconds), resulting in fast photothermal response.

Table 1. Summary of the frequently used photothermal agents in LCP-based actuators

	Materials	Content	Maximum temperature under light irradiation	Light intensity	$T_{lc\text{-}iso}$	Reference
Carbon nanotube (CNT)	LCE-CNTs	0.1 wt%	90 °C in 12s	2.25W/cm^2	77 °C	101
	LCE/SWCNT	1.0 wt%	120 °C in 30s	-	87 °C	102
	LCE/PPE-SWNTs[a]	0.2 wt%	80 °C in 4s	-	52.5 °C	103
	CNT-xLCEs[b]	0.1 wt%	180 °C in 20s	0.84W/cm^2	105 °C	106
	SWNT-LCE/silicone bilayer film	0.1 wt%	83 °C in 10s	1.10W/cm^2	65 °C	108
	SWCNT-LCE	0.3 wt%	90 °C in 32s	0.23W/cm^2	78 °C	109
	Polyurethane/SWCNT/LCE	0.45wt%	-	0.23W/cm^2	68 °C	111
Graphene oxide (GO)	HRGO/LCE[c]	0.2 wt%	105 °C	-	86 °C	114
Gold nanorods (AuNR)	AuNR-ALCNs[d]	0.05wt%	175 °C in 40s	6.7 W/cm^2	146°C[e]	87
	AuNR/LCEs composite	0.09wt%	50 °C in 10 min[f]	-	49 °C	120
Dye	LCE/YHD796 film[g]	1.3 wt%	115 °C in 30s	-	106 °C	78
	Dye 1002-LCE/silicone bilayer film	0.2 wt%	69 °C	0.57W/cm^2	61.4 °C	108
	Bilayer LCE-YHD796	0.5 wt%	90 °C in 8s	-	67 °C, 57°C[h,i]	124
	Dye crosslinked LCE	17.0wt%	260 °C in 8s	0.83W/cm^2	116 °C	125
	LCE/imNi8(4)[j]	0.2 wt%	85 °C in 4s	4.6 W/cm^2	55 °C	129
	LCN/1-AM[k]	1.5 wt%	45 °C	0.15 W/cm^2	-	130
	LCN I[l]	7 mol%	100 °C	0.5 W/cm^2	90 °C	131
	LCN/F-azo[m]	10 wt%	31 °C	0.035W/cm^2	-	132
Polydopamine (PDA)	PDA-xLCE	2.0 wt%	160 °C in 15s	1.40W/cm^2	105 °C	136
	PDA-coated LCE film	-	160 °C in 0.4s	3.10W/cm^2	79 °C	137
Conjugated polymers	ES/LCE[n]	1.0 wt%	125 °C in 60s	-	61 °C	133
	EB/LCE[o]	1.0 wt%	100 °C in 60s	-	60 °C	

[a]PPE-SWNT: poly(p-phenyleneethynylene) functional single-walled carbon nanotubes; [b]xLCEs: liquid crystalline elastomers with exchangeable links; [c]HRGO: high temperature reduced graphene oxide; [d]AuNR-ALCNs: azobenzene liquid-crystalline networks doped with gold nanorods; [e]Temperature of sematic-isotropic phase transition; [f]Temperature was measured in THF;

[g]YHD796: NIR dye; [h]Temperature of top layer of bilayer LCE-YHD796; [i]Temperature of bottom layer of bilayer LCE-YHD796; [j]imNi8(4): N, N'- dialkylimidazolidine-2, 4, 5-trithone nickel complex carrying 2-butyloctyl carbon chains; [k]1-AM: azomerocyanine dye; [l]LCN copolymerized with mixtures of azobenzene derivative; [m]LCN copolymerized with mixtures of azobenzene derivative; [n] Emeralidine salt; [o]Emeralidine salt.

If an inorganic photothermal agent has a very high molar extinction coefficient and quantum yield of photothermal conversion, it can also endow LCP actuator with fast photothermal response at even an extremely low concentration. This is the case of gold nanoparticles (AuNPs) and nanorods (AuNRs). For example, our group recently demonstrated LCP actuator loaded with AuNRs (85). Despite the very low AuNR concentration (0.05 wt%), the actuator still shows excellent photothermal response with the temperature rising to 175 °C in less than 40s under NIR light irradiation.

Also shown in Table 1 is that in addition to dispersing photothermal agents in LCEs or LCNs, bilayer or trilayer structure is another effective method to design actuators. In this case, the photothermal agents (e.g. GO or PDA), form a thin layer on the surface of the LCP strip, the released heat under light irradiation can rise the temperature of one side of the actuator (at the interface) quickly above $T_{lc\text{-}iso}$ (e.g., within seconds), resulting in fast photothermal response.

II.I.III. Applications

II.I.III.I Complex deformation and shape morphing

One unique feature of LCE or LCN actuators is that they can undergo complex shape changes in response to light stimuli. Generally, there are three approaches to realize light-driven deformations. The first one is to create local deformation by controlling illuminated regions in monodomain LCP actuators containing photothermal agents. A nice example was demonstrated by Broer and coworkers. They shined patterns of white light on an LCP film loaded with AuNP or AuNR (NSLC or NRLC, respectively) to achieve different shape deformations

(117). By tuning the illuminated regions, the photothermally induced increase of temperature caused the LC-isotropic phase transition, resulting in local in-plane contraction along the planar director orientation and expansion along perpendicular directions (Figure 19a). These localized strains drive the films to form various buckled configurations, such as axisymmetric "hour-glass" rolled shapes (Figure 19 b and d), helix-like shapes (Figure 19c), and folding of the corners (Figure 19e).

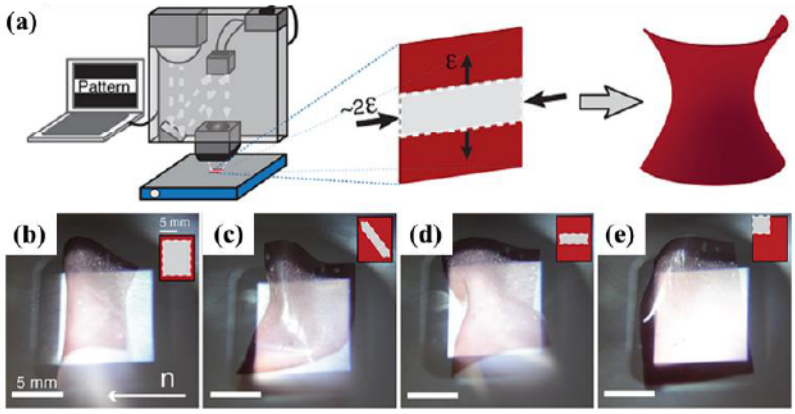

Figure 19. (a) Schematic illustration of projector setup and local in-plane contraction of nematic aligned LCP film loaded with AuNP. (b-e) Selected shape deformations of LCP film loaded with AuNP. Reproduced from [117] with permission from American Chemical Society.

Another strategy for light-induced complex shape change is to fabricate the LCP actuators with organized or patterned LC orientation profiles, such as twisted LC directors instead of uniaxial orientation. Such configured LC directors, which are usually prepared using reactive mesogens, can lead to non-uniform internal strains in the actuators under light irradiation, which results in complex shape evolution (117, 121, 122, 138, 139, 140). For example, Broer's group used a photoalignment technique to prepare IR absorbing dye-doped LCN films with complex order, such as azimuthal-, radial-, and spiral-aligned nematic director profiles. Upon IR light irradiation, these films exhibit reversible deformation due to the photothermal effect of the dye (121). As shown in Figure 20a, the azimuthal film deforms into a conical shape, while the radial film deforms into a saddle shape. In order to achieve even more complex reversible deformation

under IR light irradiation, they used the same technique to prepare accordion-like LCN actuators. In this case, the director profile was striped or checkerboard in the plane with a 90-degree twist across the film thickness. When the actuator is exposed to IR light, the accordion-like folds can be observed in the LCN film with a striped director profile, whereas the film with a checker-board director profile forms a periodic square pattern of peaks, depressions, and saddle points (Figure 20b) (122).

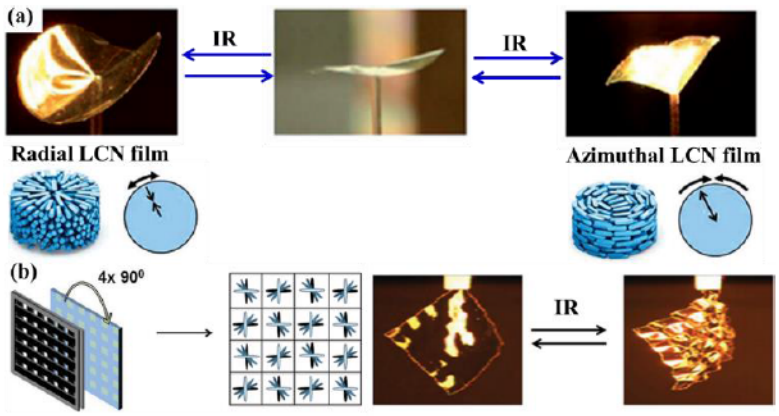

Figure 20. (a) Actuation behaviour of LCN films with azimuthal and radial alignment under IR stimulus. The arrows along the radius and the azimuth show the deformation directions. Reproduced from [121] with permission from John Wiley and Sons. (b) Deformation of a LCN film with a checkerboard pattern under IR irradiation. Reproduced from [122] with permission from John Wiley and Sons.

The last strategy consists in designing bilayer-structured LCP actuators with photothermal response. Yang's group prepared bilayer polysiloxane-based LCE actuators that can mimic a plant tendril by exhibiting two different 3D transformations (bending and chiral twisting) by tuning the wavelength band of light stimuli (124). This bilayer actuator was fabricated by gluing two different uniaxially aligned LCE samples together with a crossed angle of either 45° or -45°, as shown in Figure 21a. Upon NIR irradiation, due to the photothermal effect of the incorporated NIR dye, the two layers of the LCE actuator contract along their own alignment directions with a crossed angle of 45° or -45° (Figure 21b). Such a non-uniform contraction

leads to different contraction ratios, resulting in two bending trends along the two alignment directions. The vector sum of the two deformations creates an inclined angle with the long axis of the LCE ribbon and thus drives the dual-layer ribbon to twist or curl in either a right-handed or left-handed helix.

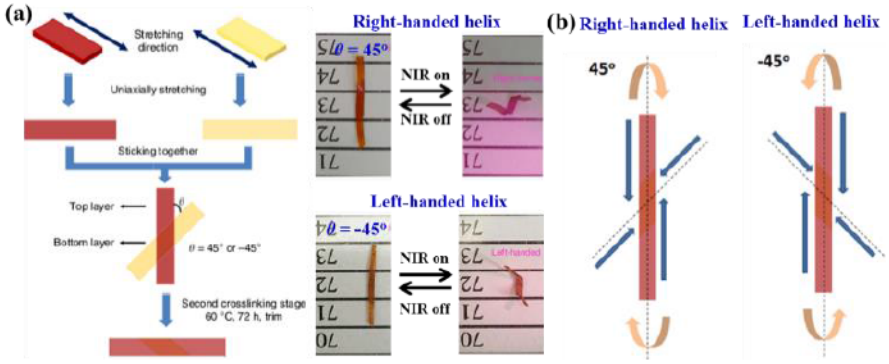

Figure 21. Soft actuator with phototunable bending and chiral twisting motion modes. (a) Design of bilayer LCE ribbons and the corresponding NIR-induced chiral twisting behavior. (b) Schematic illustration of twisting deformations of the bilayer LCE ribbons. Adapted from [124] with permission from Springer Nature.

II.I.III.II Machines, walkers, swimmers, oscillators and more

Photothermally driven deformations or shape changes of LCP actuators can be translated into light-guided movements, such as locomotion, and into devices that can execute physical work or help energy harvesting. Shown below are a few representative examples. Jiang *et al.* prepared an artificial heliotropic device by incorporating polyurethane fiber-networks as the reinforcement phase into SWCNT-LCE nanocomposite films (111). Figure 22 shows the concept of the artificial heliotropism for solar energy harvesting based on the nanocomposite films. The solar cells are installed on a platform that is connected to the LCE actuators and elastically supported so that it can tilt under the actuation force. The nanocomposite films facing the incident sunlight are always in the contracted state, while others not exposed to the sunlight are in

the relaxed state. Therefore, the platform supporting the solar cells can be driven by the contracted nanocomposite films and self-adaptively lean toward the sunlight. Note that this artificial heliotropism could be directly driven by the sunlight, similar to heliotropism of plants in nature. Subsequent laboratory tests proved that this device had full-range artificial heliotropism, with 60° of range in altitude angle, and 180° of range in azimuth angle (Figure 22b and c).

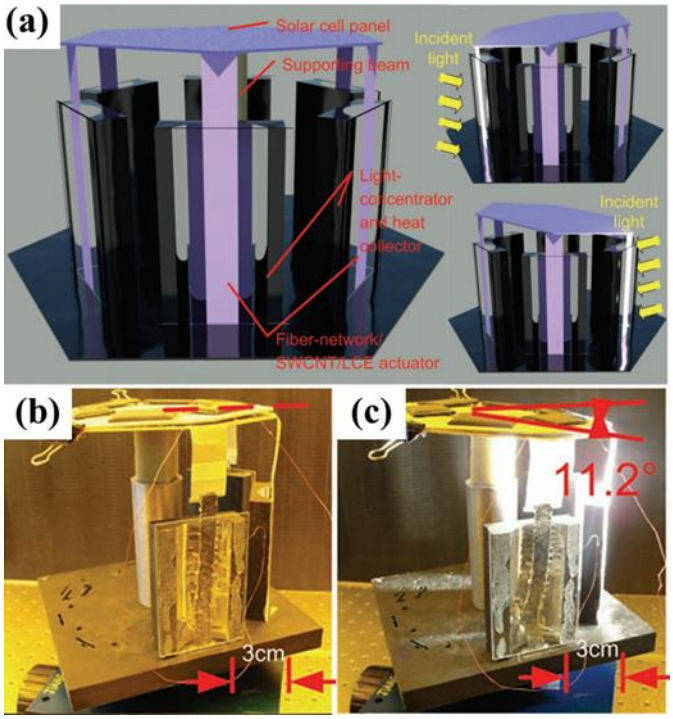

Figure 22. (a) Concept of the artificial heliotropism based on fiber network/SWCNT/LCE nanocomposite film and its heliotropic behaviour (b, c). Adapted from [111] with permission from John Wiley and Sons.

Photothermally driven LCP actuators can also transform their light-induced deformations into walking or swimming. Rogéż *et al.* fabricated a natural scale soft robot based on a dye incorporated LCE stripe, which can mimic the crawling of a caterpillar through a traveling deformation (127). The laser scanning along the stripe induces a local contraction, which leads to a curling shape deformation in the illuminated parts of the stripe, and thus drives the soft robot to move forward along the laser scanning direction (Figure 23-1(a–c)). This soft robot can also

climb on a slope with 11° incline (Figure 23-1(d)) and even squeeze through the crevice (Figure 23-1(e)). Recently, the same group developed a miniature inching robot based on a monolithic LCE film, which can perform locomotion on different substrates by spatially uniform light illumination (126). This inching robot consists of three splay aligned segments, each of which can form an arc shape, which together makes the whole strip deform into a "O" shape (Figure 23-2). Upon light irradiation, the photothermal effect forces the curved shape to be flat, thus extending the strip. After removal of the light, the robot recovers its initial shape. Through alternately turning on/off the light, the robot can undergo cyclic deformation, thereby mimicking the inching motion of a caterpillar (Figure 23-2(b)). Chen *et al.* reported an inchworm walker device based on an asymmetric SWNT–LCE/ silicone bilayer film and two polycarbonate (PC) films with different shapes (Figure 23-3(a and b)) (108). In response to IR light irradiation, the asymmetric structure of this device drives its front part and back part to bend outward and inward, respectively, which allows the whole device to crawl up a wood substrate at a 50° incline (Figure 23-3(c and d)).

On the other hand, Cai *et al.* designed a robotic swimmer based on PDA-coated LCE film, which could swim near the water and air interface in response to NIR light irradiation (Figure 23-4) (137). This soft swimmer has a fish shape with a VHB film (an adhesive film from 3M company) as its body and PDA-coated LCE film as the caudal fin. In their design, the swimming motion is controlled by the momentum exchange between the solid caudal fin and water. Upon exposing to NIR light irradiation, the tail could bend downward because of PDA coating on the bottom surface of the LCE film. After switching off the NIR light, the restoring elastic force could allow the tail to go upward quickly and extrude the water backward, which pushes the whole actuator to swim forward. Additionally, the reinforced heat dissipation in water allows a relatively moderate bending downward of the caudal fin, followed by a faster recovery, resulting in stronger momentum exchange and further promoting the forward swimming. In another example, Palagi *et al.* designed an LCE cylinder microrobot which can achieve biomi-

metic swimming and versatile locomotion in a liquid environment (141). The used LCE contains covalently bound azobenzene dye, and both the *trans-cis* photoisomerization and photothermal effect of the dye contribute to the motion. As shown in Figure 23-5, a structured light field is used in their work to selectively trigger deformation of the microrobot body, with radial expansion and longitudinal contraction of the illuminated parts, which forms a travelling wave along the cylinder and leads to its swimming motion.

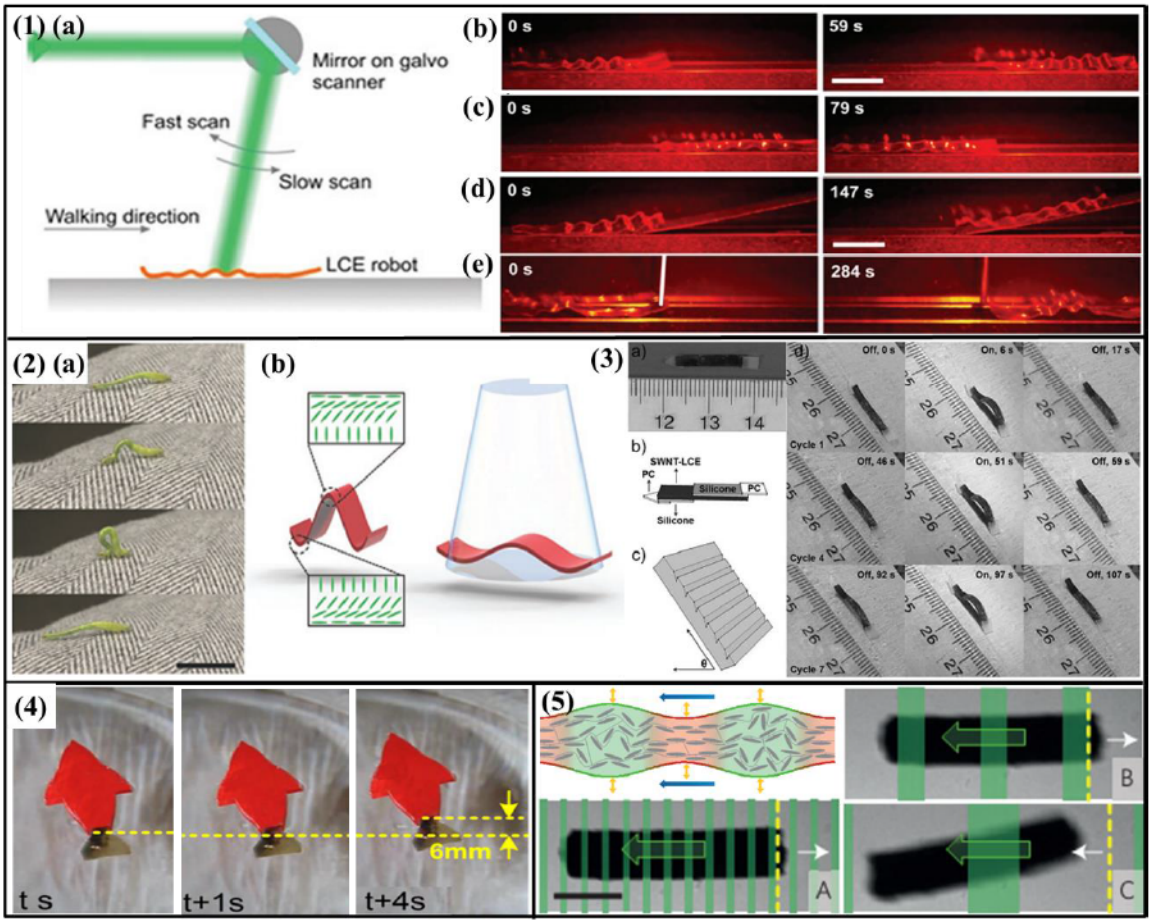

Figure 23. (1) (a) Schematic of the experiment for light-driven locomotion of the LCE soft robot. Through scanning a laser beam along the robot body,the soft robot can move forward (b) and backward (c), climb on a slope (d) and squeeze through a high slit (e). (Adapted from [127] with permission from John Wiley and Sons.) (2) Inching locomotion of a caterpillar (a) and its design based on a splay-aligned LCE. (Adapted from [126] with permission from John Wiley

and Sons.) (3) (a and b) Design of an inchworm walker device based on an SWNT–LCE/silicone bilayer film and two PC films with different shapes. (c and d) The inchworm walker can climb on the wood substrate at a 50^{o} incline under the NIR light stimulus. (Adapted from [108] with permission from John Wiley and Sons.) (4) Light-controlled swimming of a soft robot based on PDA-coated LCE film. (Adapted from [137] with permission from American Chemical Society.) (5) Concept of a light-triggered swimming microrobot using an LCE. By tuning the scanning light pattern, the microrobot can swim forward or backward (A-C). (Adapted from [141] with permission from Springer Nature.)

Autonomous oscillations that are characteristic of living systems have drawn more and more attention in recent years. A number of strategies have been proposed to design artificial systems mimicking the self-oscillation behaviour. Although most reports used the trans-cis photoisomerization in azobenzene-based LCNs (azo-LCN), self-oscillations based on the photothermal effect of azo dyes have also been disclosed. For example, Broer *et al.* incorporated various photostabilizers and azo dyes into LCN to design self-sustained mechanical oscillators (123). They demonstrated that during light irradiation, photostabilizers and azo-dye in LCN can rapidly transfer the optical energy into heat to activate self-oscillation due to the self-shad owing effect. They also realized sunlight triggered self-oscillation by using an LCN strip in which the light-absorbing dye is dispersed in a narrow line (Figure 24-1(a)). By controlling the angle of incident sunlight, this strip can continuously oscillate (Figure 24-1(b–d)). White *et al.* prepared a high modulus azo-LCN cantilever to achieve a photodriven flexural-torsional oscillation (142). By changing the alignment of the nematic director with respect to the long axis of the cantilever, the cantilever shows different dimensional oscillations, such as in-plane oscillation, bidirectional bending, flexural-torsional oscillation and twisting (Figure 24-2). Other sophisticated and intelligent actuation systems based on the photothermal effect of azobenzene have also been designed. Among the most notable examples, on the one hand, Martella *et al.* fabricated an LCN-based microhand that can grab microscopic objects in both water and air envi-

ronments, distinguish objects of different colours and grab only those showing the right absorption properties (Figure 24-3) (138). On the other hand, Priimagi and coworkers demonstrated LCE-based artificial flytraps that can differentiate different micro-objects through their optical feed-back and display automatic closure motion (grabbing) only when specific conditions are met (Figure 24-4) (139).

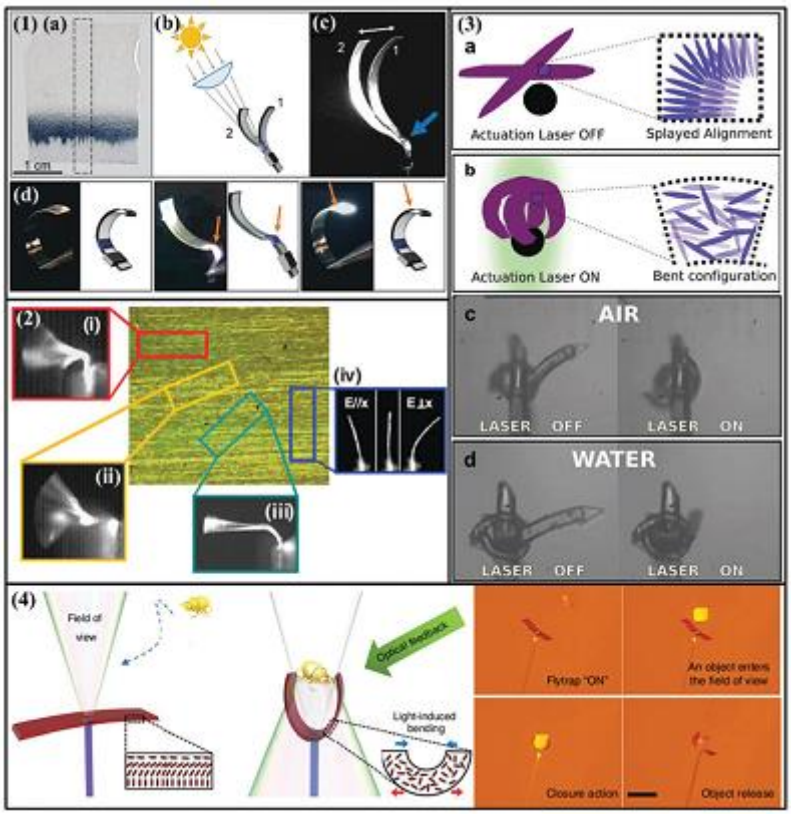

Figure 24. (1) Self-oscillation of LCN film with the indigo hinge: (a) picture and (b) schematic of sunlight triggered self-oscillation of an LCN film contain-ing a narrow line of indigo as the active component, (c) superposition of two pictures showing the self-shadowing effect on the hinge of the LCN film, and (d) pictures showing that the film can bend and self-oscillate only when the focus point of light (indicated by the orange arrow) is on the indigo stripe. (Adapted from [123] with permission from John Wiley and Sons.) (2) Polarized optical micrograph (POM) of an azo-LCN cantilever and its corresponding light-induced oscillation with nematic director cut to be (i) 0°, (ii) 15°, (iii) 45° and (iv) 90° to the long axis. (Adapted from [142] with

permission from John Wiley and Sons.) (3) Design of an LCN-based microhand: (a and b) illustration of open and closed microhands with the corresponding mesogen alignment at the laser-off and laser-on state, respectively, and (c and d) pictures showing the microhand performing actuation both in air and water. (Adapted from [138] with permission from John Wiley and Sons.) (4) Concept of a light-triggered artificial flytrap based on a dye incorporated LCE actuator with splay orientation and its flytrap-type capture motion. (Adapted from [139] with permission from John Wiley and Sons.)

Recently, our group investigated an NIR dye-doped LCE that shows several interesting features (129). With the LCE being photocrosslinkable, a strip can be made to have one side of crosslinked monodomain of uniaxial LC orientation (actuating side) along the thickness direction and the other side of crosslinked polydomain (non-actuating). When the non-actuating side of the actuator is exposed to NIR light, the strip bends away from the light source like layered actuators (Figure 25d and Figure 25e). This actuator is multifunctional. With the two ends of the strip fixed, scanning a NIR laser can generate and propagate a wave, which can be used to transport an object like a light-driven "walking belt". With two ends free, microcrawler can be fabricated that can turn in the movement as guided by laser. If only one end of the strip is fixed and the other end is suspended in air, the actuator displays versatile autonomous arm-like motions under constant NIR light irradiation as a result of self-shadowing effect. As shown in Figure 24, by tuning the incident laser direction with respect to the actuator, it can execute self-sustained upward-downward bending motion (Figure 25a) or twisting motion (Figure 25b).

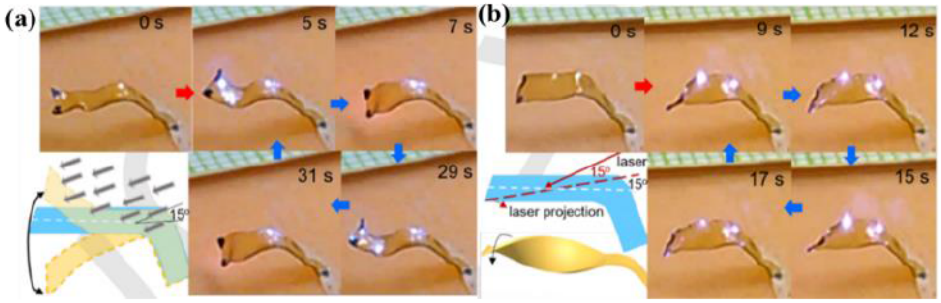

Figure 25. Autonomous arm-like motions of the LCE/imNi8(4) actuator. (a) Self-sustained

upward-downward bending motion. In this case, NIR laser applied at an incident angle of 15° and along the actuator's long axis. (b) Self-sustained twisting motion. In this case, NIR laser applied at an incident angle of 15° while being rotated by 15° along the actuator's long axis. Reproduced from [129] with permission from John Wiley and Sons.

The photothermal effect can also be combined with photochemical reaction in LCE or LCN actuators to enhance the photocontrol. An example was demonstrated by our group (87). Gold nanorods (AuNR) were loaded in a main-chain LCN containing azobenzene mesogens. Photo-mechanical force and photocontrolled deformation and motion can be obtained using either *trans-cis* photoisomerization of azobenzene under UV and visible light irradiation or photo-thermal effect by NIR light excitation of AuNR for heat release. Among the demonstrated actuations, an UV- and NIR light-responsive polymer "crane" was fabricated to carry out a sequence of physical work including grasping, lifting up, lowering down and release of an object (Figure 26)

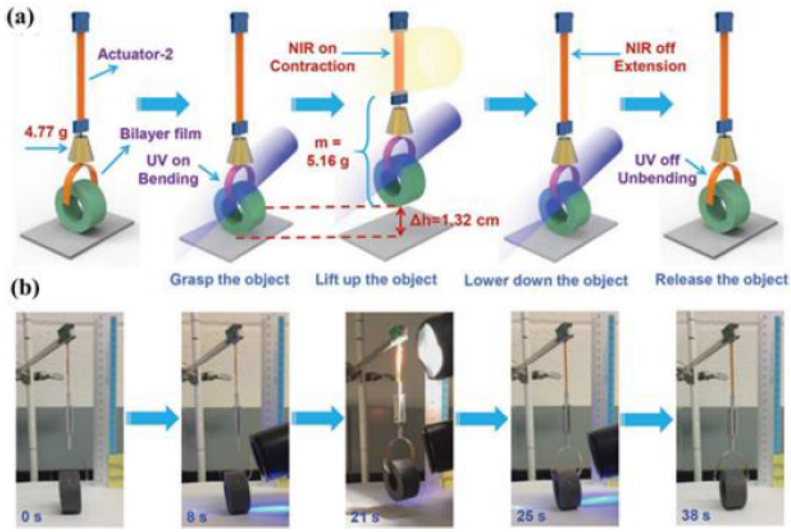

Figure 26. (a) Schematic illustration of the polymer "crane" based on AuNR incorporated LCN containing azobenzene mesogens. (b) Under the UV- and NIR light stimuli, such polymer "crane" can successively grasp, lift up, and put down an object. Reproduced from [87] with

permission from John Wiley and Sons.

III. Objective of the Thesis

The overall objective of this thesis is to design, fabricate and study two types of stimuli-responsive polymers, namely, gas-responsive porous membranes for size-selective separation and nanofiltration, and light-controlled polymer actuators.

Specifically, on one hand, we want to introduce CO_2-responsive polymers into separation membranes in a bid to develop a new external stimulus that can reversibly open and close the membrane pores to allow size-selective separation or on-demand separation. A first method was reported in Chapter 1. We demonstrate that the concept of gas-tunable pore sizes as well as gas-controlled separation of species can be successfully realized by coating a substrate membrane PVDF with PDA to enable further functionalization of the membrane with a CO_2-responsvie polymer, poly(*N*,*N*-diethylaminoethyl methacrylate) (PDEAEMA). By doing so, the transition between extended and collapsed PDEAEMA chains upon alternating CO_2 and Ar bubbling into the solution results in reversible closure and opening of the pores and thus gas-controllable permeability. Based on the first project, in order to improve the separation capability of CO_2-responsive polymer membranes.

In a study described in Chapter 2, a design of CO_2-responsive composite nanofiltration membrane for water purification is developed. It is fabricated through electrostatic and π-π interaction between pyrene modified PDEAEMA (Py-PDEAEMA) and GO. First, the reversible, gas-tunable water permeability can be achieved by switching CO_2 and Ar stimulation. The water permeability of such novel nanofiltration membrane is much higher than those of commercial nanofiltration membranes. Secondly, the rejection of organic dye molecules of this membrane is similarly efficient as that of a pure GO membrane despite the much higher water permeability. Finally, the CO_2 can induce reversible changes of the charge sign, endowing this composite

membrane with an excellent trade-off between rejection of salts like $MgCl_2$ and water permeability. The purpose of this work is to develop smart stimuli-responsive nanofiltration membranes for water purification.

On another front of stimuli-responsive polymers research, liquid crystal polymer (LCP) actuators are gaining growing interest. We have carried a study with the specific purpose of developing light-triggered LCP actuators through the use of photothermal effect. We propose a trilayer-structured actuator comprising a thin reduced graphene oxide (RGO) top layer, an inactive polymer middle layer and an active LCN bottom layer. When exposing the RGO side to a moving NIR laser, a moving wave along the strip actuator can be generated, making the strip an effective caterpillar walker whose light-driven locomotion has appealing attributes. This trilayer actuator can move on untreated, either horizontal or inclined surface under the guide of NIR laser. Moreover, while known actuators using photothermal effect are usually fabricated by mixing the nanofiller as NIR light heater with the polymer, which raises the compatibility concern. The easy trilayer fabrication method laminates directly a "sheet" of RGO on thick polymer layers, which allows to circumvent the potential problems. The results of this study are presented in Chapter 3.

In the last chapter of the thesis, Chapter 4, we provide an overall discussion about the main conclusions and innovation of our research. We also come up with some future works that are worth in-depth study.

CHAPITRE 1. CO_2-RESPONSIVE POLYMER MEMBRANES WITH GAS-TUNABLE PORE SIZE

1.1. About the Project

Inspired by cell membranes that can self-regulate permeability and selectivity in response to changing environmental conditions, design of stimuli-responsive porous membranes has aroused intensive interest and research from scientists. In response to variation in environmental stimuli, such as temperature, pH, light, magnetic field or redox agents, these membranes can self-regulate their pore sizes and further manipulate the permeability and selectivity. Although many progresses have been made in recent years, it still exists some problems for these stimuli-responsive porous membranes. That is, pH-responsive porous membrane often suffers from declined switch ability of membrane after cyclic addition of acids and bases into the solution because of the salt accumulation, while temperature or light stimuli may destroy the integrity of membranes to a certain extent. CO_2-responsive polymers are a class of polymers in which the tertiary amine groups can react with CO_2 in water to make the polymer chains hydrophilic and extended. After bubbling N_2 or Ar to remove CO_2, the polymer chains can recover their initial state with collapsed chain conformation. This gas-switchable conformational change can be repeated as many cycles as without chemical contamination of the polymer solution. With the unique features of CO_2-responsive polymers in mind and an eye to solve those problems of traditional stimuli-responsive membranes, we developed a CO_2-responsive polymer membrane whose pore can be modulated between the ‘‘closed’’ and ‘‘open’’ state by reversibly bubbling CO_2 and Ar into solution. Compared with other stimuli, such as pH or temperature, gas is an environmentally friendly and cost-effective stimulus for achieving reversible modulation of the pore size and the size selectivity of the membrane.

This work was published in *Chemical Communications*, **2017**, 53, 9574 by Liangliang Dong,

Weizheng Fan, Hongji Zhang, Mingqing Chen and Yue Zhao. This research work was accomplished in the Université de Sherbrooke under the supervision of Prof. Zhao and co-supervision of Prof. Chen. I fabricated the CO_2-responsive polymers, poly(N, N-diethylaminoethyl methacrylate) (PDEAEMA) and all membrane samples (PDA@PVDF membranes and PDEAEMA-PDA@PVDF membranes) and performed the experiments reported in the paper. Weizheng Fan assisted me with SEC experiments and Hongji Zhang gave me some useful advice about this project. I wrote the first draft of the manuscript. Prof. Zhao revised and finalized the manuscript.

1.2. Paper Published in Chemical Communications, 2017, 53, 9574.

CO_2-Responsive polymer membranes with gas-tunable pore size

Liangliang Dong,[ab] Weizheng Fan,[a] Hongji Zhang,[b] Mingqing Chen*[b] and Yue Zhao*[a]

[a]Département de chimie, Université de Sherbrooke, Sherbrooke, QC, J1K 2R1, Canada. E-mail: yue.zhao@usherbrooke.ca

[b]Key Laboratory of Synthetic and Biological Colloids, Ministry of Education, School of Chemical and Material Engineering, Jiangnan University, 1800 Lihu Road, Wuxi 214122, P. R. China. E-mail: mqchen@jiangnan.edu.cn

1.2.1 Abstract

We report a smart polymer membrane whose pore can be switched between the ‘‘closed’’ and ‘‘open’’ state just by passing CO_2 and Ar in solution respectively. Compared with other stimuli, such as pH or temperature change, gas is an environmentally friendly and cost-effective stimulus for reversibly tuning the pore size and imparting the size selectivity of the membrane.

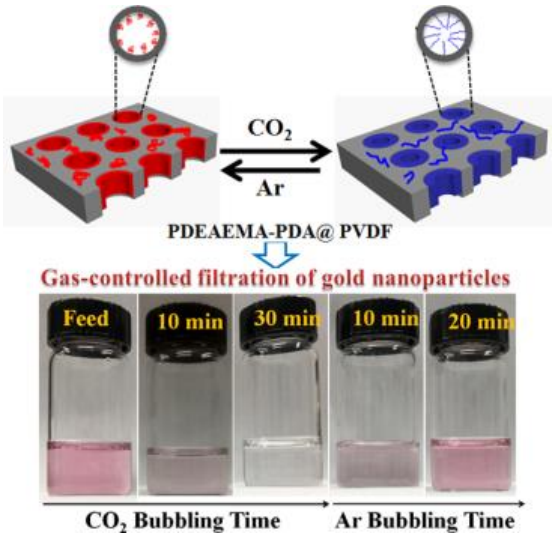

1.2.2. Introduction

Inspired by cell membranes with stimuli-responsive channels for self-regulating permeability and selectivity in response to changing environmental conditions, artificial smart gating membranes have been created by chemically or physically incorporating stimuli-responsive materials into porous membranes as functional gates.[1] In response to variation in environmental stimuli, such as temperature,[2] pH,[3] light,[4] magnetic field[5] or redox agents,[6] their functional gates have a conformational switch to adjust the pore sizes of the membranes and thus to manipulate the permeability and selectivity. For instance, Clodt *et al.*[2a] prepared temperature-sensitive porous membranes by grafting poly(N-isopropylacrylamide) (PNIPAAm) onto polystyrene-*b*-poly(4-vinyl-pyridine) (PS-*b*-P4VP) porous membranes, in which variation of the pore size and water flux could be finely adjusted by temperature. Chu *et al.*[2b] reported multi-stimuli-responsive membranes with hierarchically structured gates, which were able to respond to changes in temperature, pH, salt concentration and anion species. However, for pH-responsive porous membranes, addition of acids and bases into the solution results in salt accumulation that could contaminate the system and diminish the switchability, while temperature or light responsive membranes may be damaged by the stimuli to a certain extent.[7] Therefore, it is urgent to develop environmentally friendly and cost-effective stimulation modes for pore-tunable membranes.

As a nontoxic and inexpensive gas, carbon dioxide (CO_2) can reversibly switch certain types of solvents, surfactants, vesicles and polymer gels.[8,9] Poly(N,N -diethylaminoethyl methacrylate) (PDEAEMA) is a representative CO_2-responsive polymer, in which the tertiary amine groups can react with CO_2 in water, and the protonated form makes the polymer hydrophilic and exhibit an extended chain conformation.[9a] Upon subsequent exposure to N_2 or Ar to remove CO_2, the polymer recovers its hydrophobic state with collapsed chain conformation. This gas-switchable conformational change can be repeated for as many cycles as required without chemical contamination of the polymer solution. This robust property prompts us to select PDEAEMA as a CO_2-sensitive polymer for the gas-controlled porous membrane.

1.2.3. Results and Discussion

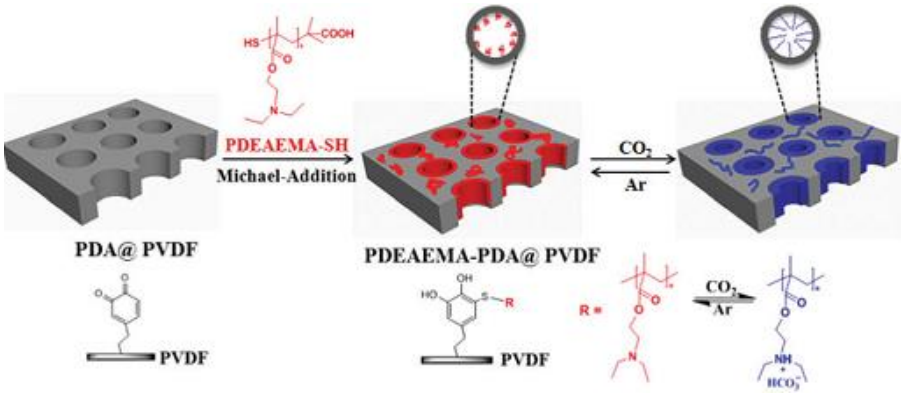

Figure 1. Schematic illustration of the preparation of CO_2-responsive PDEAEMA-PDA@PVDF membranes via the Michael addition reaction of PDA-coated PVDF membranes and thiolated PDEAEMA; the polymer grafting reaction as well as the reversible protonation/deprotonation of tertiary amine groups in PDEAEMA upon CO_2 and Ar bubbling, respectively, are also shown. The membrane permeability decreases through membrane pore closure upon exposure to CO_2, while the permeability recovers through pore opening upon exposure to Ar that removes CO_2.

Here we demonstrate, for the first time, a simple method to prepare gas-switchable porous membranes. As shown in Figure 1, we firstly synthesized a series of thiol-terminated PDEAEMA homopolymers by reversible addition-fragmentation chain transfer (RAFT) polymerization and ammonolysis, respectively.[10] Then using polydopamine (PDA) as an interlayer coating for the functionalization of polyvinylidene fluoride porous membranes (PVDF) with thiol terminated PDEAEMA through the Michael addition reaction between thiol groups and PDA (shown in Figure 1) (for synthesis and characterization details see the Supporting Information, Table S1 and Figure S1).[11] The working mechanism of reversible variation of the pore size for the membrane by CO_2/Ar bubbling is also depicted in Figure 1. At room temperature and pH = 7, PDEAEMA chains are insoluble in water, being in the collapsed state, thus the membrane is ‘‘open’’. Upon passing CO_2 through the solution, the tertiary amine groups in

PDEAEMA react with CO_2 in water to form charged ammonium bicarbonate,[8g] which renders the polymer soluble in water, and the chains of extended conformation fill in the pore to close the membrane. Subsequently, passing Ar through the solution can remove CO_2 and bring PDEAEMA chains back to the insoluble state, thus reopening the membrane. It should be mentioned that a CO_2-responsive membrane made with electrospun nanofibers of PDEAEMA was recently reported by Yuan and coworkers.[7c] Their focus was to use CO_2/N_2 to switch between the hydrophilic and hydrophobic membrane surfaces in order to achieve gas-switchable oil/water wettability. In the present study, our purpose is to use gases to open or close the pore of the membrane to allow the passage or retention of a compound in solution based on size exclusion.

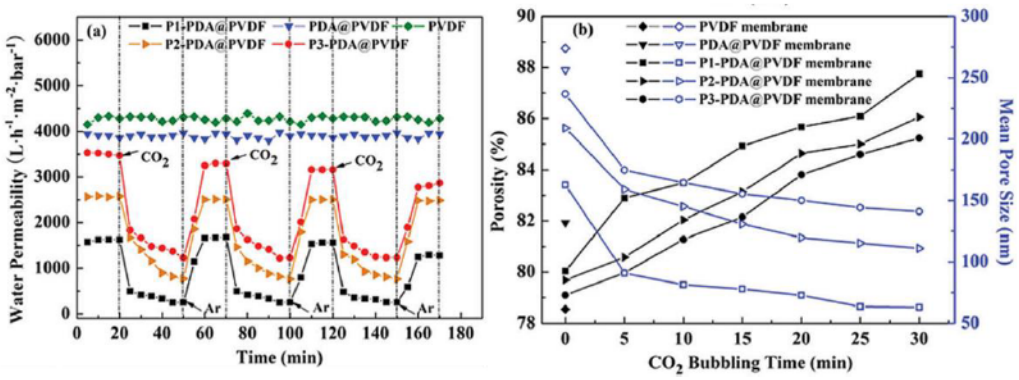

Figure 2. CO_2-Responsive behaviour of the PDEAEMA-PDA@PVDF membranes: (a) reversible water permeability decrease and recover upon CO_2 and Ar bubbling, respectively, and the results of PVDF and PDA@PVDF membranes are shown for comparison; and (b) change in porosity and mean pore size as a function of CO_2 bubbling time. Note that P-PDA@PVDF membranes represent PDEAEMA-PDA@PVDF membranes with different molecular weights of PDEAEMA (P1<P2< P3).

The successful formation of PDEAEMA-PDA@PVDF membranes is confirmed by FT-IR/ATR (Figure S2, Supporting Information). No obvious difference between the spectra of the pure PVDF membrane and the PDA@PVDF membrane was detected. However, new peaks appearing at 1730 cm^{-1} and 1068 cm^{-1} belong to C=O and N-CH_2 vibrations, which implies the grafting of PDEAEMA segments onto the surface of membranes (inside and outside the pores).

The CO_2-responsive behaviour of PDEAEMA-PDA@PVDF membranes was verified by a water permeability test under CO_2/Ar stimulation at room temperature (setup illustration and details in the measurement of water permeability are shown in the Supporting Information). As shown in Figure 2(a), when CO_2 was bubbled through the solution (flow rate: 20 mL min^{-1}), the water permeability for all three PDEAEMA-PDA@ PVDF membranes, differing in the initial water permeability due to different molecular weights of PDEAEMA, decreased until a plateau was reached after 30 min, while pure PVDF and PDA@PVDF membranes showed no change in water permeability under the same CO_2 stimulation. The water permeability decreased by 84.1% (P1-PDA@PVDF), 69.8% (P2-PDA@PVDF) and 65.2% (P3-PDA@PVDF), respectively. The significant decrease in water permeability was due to stretched PDEAEMA chains under CO_2 in water, leading to decreased effective pore sizes (pore closure). Subsequently, upon passing Ar through the solution (flow rate: 20 mL min^{-1}), the water permeability increased to the initial level, indicating that the stretched PDEAEMA chains were gradually deprotonated and took a coiled conformation, resulting in the increase of the effective pore size (pore open).[12] The change in the water permeability was reversible for several tested cycles of alternating bubbling of CO_2 and Ar into the solution, while, by contrast, the pure PVDF and PDA@PVDF membranes displayed almost constant water permeability under the same stimulation conditions, confirming that the responsiveness of the PDEAEMA chains to CO_2 was at the origin of the reversible variation of the water permeability.

In order to further verify our hypothesis that CO_2/Ar can control the pore opening and closure state, the mean radius of the pore of CO_2 responsive PDEAEMA-PDA@PVDF membranes was calculated according to Poiseuille's equation:[13]

$$\boldsymbol{r = \sqrt{(8\eta l j / \varepsilon A \Delta P)}}, \quad (1)$$

where η is the viscosity of water (8.9×10^{-4} Pa s, 25 °C); l is the membrane thickness (m); j is the pure water flux (L s^{-1}); ε is the membrane porosity (%); ΔP is the pressure difference (Pa); and A is the membrane area (m^2).

And the membrane porosity (ε) was calculated according to eqn (2)

$$\boldsymbol{\varepsilon} = \left(\frac{\boldsymbol{m_1 - m_2}}{\boldsymbol{\rho_{H_2O}}}\right) / \left(\frac{\boldsymbol{m_1 - m_2}}{\boldsymbol{\rho_{H_2O}}} + \frac{\boldsymbol{m_2}}{\boldsymbol{\rho_P}}\right) \times \mathbf{100\%}, \quad (2)$$

where m_1 is the wet membrane weight (g), m_2 is the dry membrane weight (g), ρ_{H2O} is the water density (0.998 g cm^{-3}) and ρ_p is the PVDF density (1.74 g cm^{-3}). The results of porosity and mean pore size of membranes with bubbling CO_2/Ar are shown in Figure 2(b). Large porosities for the three PDEAEMA-PDA@PVDF membranes were obtained, compared to the pure PVDF membrane; on the other hand, the mean pore sizes of the PDEAEMA-PDA@PVDF membranes decreased with increasing CO_2 bubbling time. For example, when the CO_2 bubbling time was 30 min, the mean pore size of the P1-PDA@PVDF membrane decreased from 162 nm to 60 nm, which is the smallest pore size achieved for all three membranes, and which is mainly due to larger grafting density (1.3 mg cm^{-2}) and grafting degree (23%) of the P1-PDA@PVDF membrane than the other two membranes (Figure S5, Supporting Information).

The gas-controlled reversible change in the pore size over a large range of sizes means that the membrane may be useful for size-selective separation or ‘‘valve’’ for on-demand passage of species of appropriate sizes. We carried out an experiment to test this smart functionality of the membrane, the results are shown in Figure 3. Gold nanoparticles (AuNPs, 50 nm in diameter) in aqueous solution was chosen as the feed solution, while the P1-PDA@PVDF membrane was utilized (its mean pore size is gas-tunable between 162 and 60 nm). The permeability of AuNPs under the CO_2/Ar stimulation was investigated by monitoring the amount of the nanoparticles passing through the membrane, which is proportional to the apparent absorbance of the surface plasmon resonance (SPR) peak of AuNPs centred at about 528 nm.[14] To this end, UV-vis absorption spectra of the feed and filtrate solution were recorded at various CO_2 or Ar bubbling times. Figure 3(a) compares the spectra of the feed solution, the filtrate with the membrane exposed to 30 min CO_2 bubbling and the filtrate with the membrane subsequently exposed to 20 min Ar bubbling. It can be seen that 30 min CO_2 treatment basically closed the pore of the membrane and leaves few nanoparticles to go through, since the SPR peak of the filtrate is

hardly discernible. After 20 min of Ar treatment, the pore appeared to reopen to allow the nanoparticles to pass through the membrane, as revealed by the prominent SPR peak of the filtrate. Since the mean pore size is tunable by adjusting CO_2 or Ar bubbling time, the amount of AuNPs passing the membrane can easily be controlled. This feature is visible in Figure 3(b) that shows changes in the SPR absorbance at 528 nm of the filtrate and in the corresponding rejection rate of AuNPs over CO_2 or Ar bubbling time (the first data after membrane exposure to CO_2 or Ar, indicated by an arrow in the plots, correspond to 5 min gas bubbling). Essentially, with prolonging CO_2 bubbling time, the number of 450 nm pores in the membrane decreases and, as a result, the rejection to AuNP filtration increases. The opposite occurs under subsequent Ar exposure. Figure 3(c) shows a series of photographs of the filtrate compared to the feed solution appearing red. The decreasing and then increasing amount of AuNPs in the filtrate upon CO_2 then Ar bubbling can be noticed visually from the fading and then recovery of the color. Moreover, the gas-controllable rejection rate for AuNPs by passing alternately CO_2 and Ar in the solution could be repeated many times with no sign of deterioration in separation performance (Figure S8, Supporting Information).

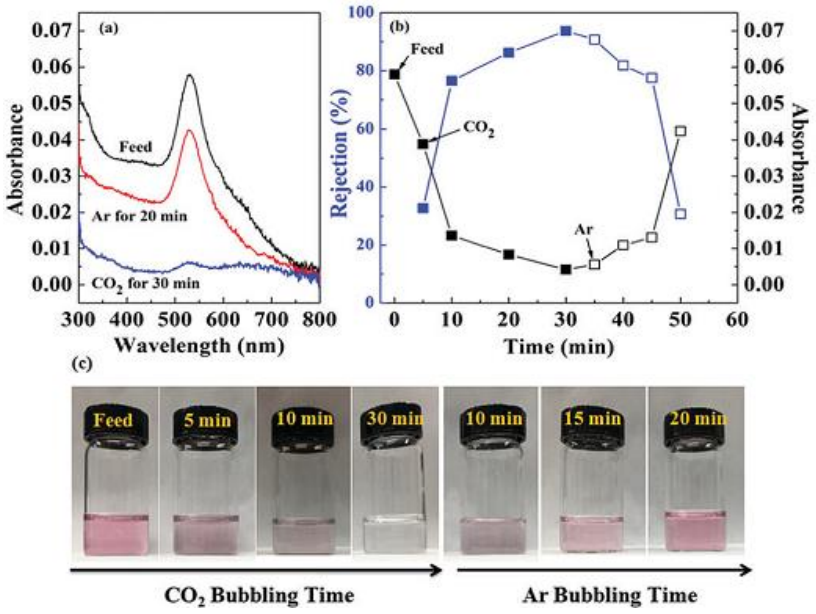

Figure 3. (a) UV-vis spectra of the feed solution with dissolved AuNPs (50 nm) and the filtrate

solution using the P1-PDA@PVDF membrane exposed to 30 min CO_2 bubbling and subsequently to 20 min Ar bubbling respectively. (b) Change in apparent absorbance at 528 nm (surface plasmon resonance of AuNPs) of the filtrate over CO_2 and subsequently Ar bubbling time for the P1-PDA@PVDF membrane as well as the corresponding change in the rejection rate for AuNPs, calculated by comparing the absorbance difference between the feed solution and filtrates. (c) Photographs of the feed solution and filtrates with the membrane exposed to various CO_2 and Ar bubbling times.

1.2.4. Conclusions

In conclusion, we have demonstrated a novel type of CO_2-responsive polymer membrane that exhibits gas-tunable pore size as well as gas-controlled switching between pore-open and pore-closure states with respect to separation of species in aqueous solution. We showed that the filtration of AuNPs (50 nm) could be controlled in a size-exclusion manner by reversibly changing the pore size of the membrane through CO_2 or Ar bubbling. Moreover, the preparation method is easy, robust and general, which consists in grafting a CO_2-switchable polymer like PDEAEMA onto the pore surface of a commercially available porous membrane like PVDF coated with a PDA layer. Compared to other stimuli such as pH or temperature change, the use of CO_2 is not only efficient for switching, but also environmentally friendly and cost-effective. By demonstrating the effectiveness of using a CO_2-switchable polymer coating to control the membrane pore size, this work points out the great potential of developing smart membranes for applications requiring or involving tunable, size-selective separation of molecular species or nanoparticles.

Acknowledgements

We acknowledge the financial support from the Natural Sciences and Engineering Research Council of Canada (NSERC) and le Fonds de recherche du Québec: Nature et technologies

(FRQNT). L. Dong thanks the China Scholarship Council (CSC) for awarding him a scholarship. H. J. Zhang thanks the Natural Science Foundation of Jiangsu Province (BK20150135).

Notes and references

1 (a) Y. Jiang, A. Lee, J. Chen, M. Cadene, B. T. Chait and R. MacKinnon, *Nature*, 2002, **417**, 523-526; (b) Z. Liu, W. Wang, R. Xie, X. J. Ju and L. Y. Chu, *Chem. Soc. Rev.*, 2016, **45**, 460-475.

2 (a) J. I. Clodt, V. Filiz, S. Rangou, K. Buhr, C. Abetz, D. Höche, J. Hahn, A. Jung and V. Abetz, *Adv. Funct. Mater.*, 2013, **23**, 731-738; (b) Y. C. Chen, R. Xie and L. Y. Chu, *J. Membr. Sci.*, 2013, **442**, 206-215; (c) L. Y. Chu, Y. Li, J. H. Zhu and W. M. Chen, *Angew. Chem., Int. Ed.*, 2005, **44**, 2124-2127.

3 (a) E. Stratakis, A. Mateescu, M. Barberoglou, M. Vamvakaki, C. Fotakisae and S. H. Anastasiadis, *Chem. Commun.*, 2010, **46**, 4136-4138; (b)A. Bera, C. U. Kumar, P. Parui and S. K. Jewrajka, *J. Membr. Sci.*, 2015, **481**, 137-147; (c) F. Schacher, T. Rudolph, F. Wieberger, M. Ulbricht and A. H. E. Müller, *ACS Appl. Mater. Interfaces*, 2009, **7**, 1492-1503.

4 (a) L. Hu, S. J. Gao, X. G. Ding, D. Wang, J. Jiang, J. Jin and L. Jiang, *ACS Nano*, 2015, **5**, 4835-4842; (b) N. G. Liu, Z. Chen, D. R. Dunphy, Y. B. Jiang, R. A. Assink and C. J. Brinker, *Angew. Chem., Int. Ed.*, 2003, **42**, 1731-1734.

5 (a) X. Lin, B. N. Quoc and M. Ulbricht, *ACS Appl. Mater. Interfaces*, 2016, **8**, 29001-29014; (b) A. M. Gajda and M. Ulbricht, *J. Mater. Chem. B*, 2014, **2**, 1317-1326.

6 Y. Ito, S. Nishi, Y. S. Park and Y. Imanishi, *Macromolecules*, 1997, **30**, 5856-5859.

7 (a) M. Motornov, R. Sheparovych, E. Katz and S. Minko, *ACS Nano*, 2008, **2**, 41-52; (b) L. A. Fielding, S. Edmondson and S. P. Armes, *J. Mater. Chem.*, 2011, **21**, 11773-11780; (c) H. L. Che, M. Huo, L. Peng, T. Fang, N. Liu, L. Feng, Y. Wei and J. Y. Yuan, *Angew. Chem., Int. Ed.*, 2015, **54**, 8934-8938.

8 (a) Q. Zhang, L. Lei and S. P. Zhu, *ACS Macro Lett.*, 2017, **6**, 515-522; (b) K. J. Boniface, R. R. Dykeman, A. Cormier, H. B. Wang, S. M. Mercer, G. Liu, M. F. Cunningham and P.

G. Jessop, *Green Chem.*, 2016, **18**, 208-213; (c) Y. F. Cai, W. M. Shen, R. Wang, W. B. Krantz, A. G. Fane and X. Hu, *Chem. Commun.*, 2013, **49**, 8377-8379; (d) Q. Yan, R. Zhou, C. K. Fu, H. J. Zhang, Y. W. Yin and J. Y. Yuan, *Angew. Chem., Int. Ed.*, 2011, **50**, 4923-4927; (e) H. Liu, W. Wang, H. Yin and Y. Feng, *Langmuir*, 2015, **31**, 8756-8763; (f) S. J. Lin and P. Theato, *Macromol. Rapid Commun.*, 2013, **34**, 1118-1133; (g) Z. R. Guo, Y. J. Feng, Y. Wang, J. Y. Wang, Y. F. Wu and Y. M. Zhang, *Chem. Commun.*, 2011, **47**, 9348-9350; (h) L. Lei, Q. Zhang, S. Shi and S. Zhu, *Langmuir*, 2015, **31**, 2196-2201.

9 (a) D. H. Han, X. Tong, O. Boissiére and Y. Zhao, *ACS Macro Lett.*, 2012, **1**, 57-61; (b) B. Yan, D. H. Han, O. Boissiére, P. Ayotte and Y. Zhao, *Soft Matter*, 2013, **9**, 2011-2016; (c) Q. Yan and Y. Zhao, *J. Am. Chem. Soc.*, 2013, **135**, 16300-16303.

10 (a) X. P. Qiu and F. M. Winnik, *Macromol. Rapid Commun.*, 2006, **27**, 1648-1653; (b) M. Aqil, A. Aqil, F. Ouhib, A. E. Idrissi, C. Detrembleur and C. Jérôme, *RSC Adv.*, 2015, **5**, 85035-85038; (c) P. E. Williams, S. T. Jones, Z. Walsh, E. A. Appel, E. K. A. Hamed and O. A. Scherman, *ACS Macro Lett.*, 2015, **4**, 255-259; (d) Y. M. Ma, D. X. Wei, H. Yao, L. P. Wu and G. Q. Chen, *Biomacromolecules*, 2016, **17**, 2680-2690.

11 (a) Y. G. Shi, M. Y. Liu, K. Wang, F. J. Deng, Q. Wan, Q. Huang, L. H. Fu, X. Y. Zhang and Y. Wei, *Polym. Chem.*, 2015, **6**, 5876-5883; (b) X. J. Li, Q. F. Fu, Q. H. Zhang, X. M. Jiang, F. Q. Yang, W. L. Wei and Z. N. Xia, *Anal. Methods*, 2015, **7**, 8227-8234.

12 H. Yin, A. L. Bulteau, Y. J. Feng and L. Billon, *Adv. Mater. Interfaces*, 2016, **3**, 1500623-1500632.

13 (a) M. G. Zhang, Q. T. Nguyen and Z. H. Ping, *J. Membr. Sci.*, 2009, **327**, 78-86; (b) X. H. Lü, X. K. Wang, L. Guo, Q. Y. Zhang, X. M. Guo and L. S. Li, *J. Membr. Sci.*, 2016, **520**, 933-940.

14 S. R. Johnson, S. D. Evans, S. W. Mahon and A. Ulman, *Langmuir*, 1997,**13**, 51-57.

1.2.5. Supporting Information

1.2.5.1. Synthesis and Characterization

1.2.5.1.1. Materials

2-(Diethylamino)ethyl methacrylate (Reagent plus, 99 % Aldrich)was passed through an activated basic alumina column to remove the inhibitory substances. 2,2'-Azobis(2-methylpropionitrile) (AIBN) (Sigma-Aldrich, 98%) was recrystallized from methanol before use. The chain transfer agent of DMTA was synthesized according to a previous report.[1] Dopaminehydrochloride (DA, Aldrich, 98%) and tris(hydroxymethyl)-aminomethane (Tris base, Aldrich, 98%) was used as received. Polyvinylidene fluoride microfiltration membranes (α-PVDF, mean pore size 0.22μm, diameter 47 mm) were purchased from Shanghai Xingya Purification Material. Other chemical reagents were all commercially available and of analytical grade.

1.2.5.1.2 Instrumentations

^{1}H NMR spectra were recorded on a Bruker 300 MHz using deuterated chloroform as the solvent and tetramethylsilane as the internal standard. Size exclusion chromatograph (SEC) measurements were performed on a Waters system equipped with a photodiode array detector (PDA 996) and a refractive index detector (RI 410). THF was used as the eluent at an elution rate of 1 mL/min, while polystyrene (PS) standards were used for calibration. Infrared spectra of the membranes were recorded on a FTIR (ABB Bomem, MB Series) between 800 and 4000 cm^{-1} at a resolution of 4 cm^{-1}. The morphology of membranes was examined using a Hitachi S-4700 field emission-gun scanning electron microscope (SEM) operating at 1.0 kV to10.0 kV. For SEM observation, a fine platinum coating layer (a few nm) was deposited on sample surface by using a K550 sputter coater for 1 or 2 min. UV-visible spectra were obtained using an UV-vis-NIR spectrophotometer (Agilent Cary 50 Bio).

1.2.5.1.3 Preparation of PDEAEMA-PDA@PVDF membrane

PDA@PVDF membrane. PVDF membrane was dipped into a solution of dopamine hydrochloride (2 mg/mL) dissolved in 15 mM Tris-buffer (pH 8.5, ultrapure water). The reaction vessel was shaken and the membranes were coated for 4h at room temperature. The membranes were rinsed thoroughly with ultrapure water and then dried at 60 °C under reduced pressure before use. Synthesis of PDEAEMA via RAFT. 2-(Diethylamino) ethyl methacrylate (3.33 g), AIBN (3.94 mg), CTA (36.43 mg), and THF (3 mL) were added into a Schlenk tube with a magnetic stir bar and air was eliminated by a nitrogen flow for 20 min. Next, the solution was degassed by three freeze/vacuum/nitrogen cycles and then put into an oil bath maintained at 70 °C for a certain time, respectively. Subsequently, the purified polymer was isolated by hexane precipitation after dissolving in THF. Finally, the obtained material was dried under vacuum.

Preparation of PDEAEMA-SH. PDEAEMA-CTA was dissolved in THF and then treated with n-butylamine to obtain thiol terminated PDEAEMA-SH[2]. The reaction was accomplished at room temperature for 4 h, with a color change from dark yellow to colorless. After the reaction, the product PDEAEMA-SH was also precipitated in cold n-hexane, centrifuged and vacuum-dried at room temperature for 24h before further characterization and reactions.

PDEAEMA-PDA@PVDF membrane. PDA@PVDF membrane was dipped into 50 mL ethanol for 30 min, and then a certain amount of ethanol solution of PDEAEMASH (0.3g/mL) was added and stirred for 24 h at room temperature. After cooling down to room temperature, the membrane was under stirring for additional 16 h. Subsequently, the membrane was rinsed three times with ethanol and ultrapure water and dried at 60 °C before characterization.

Synthesis of triammonium citrate-capped gold nanoparticles. Triammonium citrate-capped gold nanoparticles (AuNPs) were prepared by using triammonium citrate as the reducing agent, following a procedure similar to that reported in the literature.[3] An aqueous solution of

$HAuCl_4 \cdot 3H_2O$ (300 mL, 0.25 mM) was heated up to the boiling point with vigorous stirring (900 rpm), then the aqueous solution of triammonium citrate (1 mL, 243 mM) was introduced rapidly using a syringe. The solution was boiled for additional 30 min in an oil bath. Afterwards, the solution was cooled down to room temperature slowly. The final red solution of AuNPs was kept at room temperature.

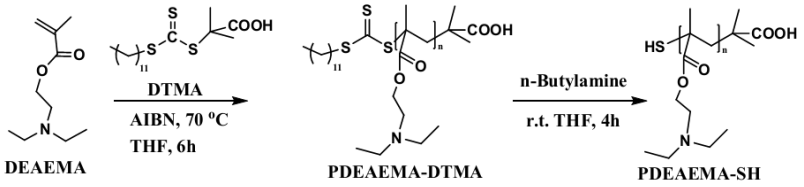

Scheme 1 Synthetic route for PDEAEMA-SH

Table S2. Properties of the obtained PDEAEMA[a]

Sample	*Mn (g/mol)*	*Mw (g/mol)*	*Đ*
P1	15700	25600	1.6
P2	16900	27600	1.6
P3	20000	32000	1.6

[a]The polymers have wide molecular weight distributions ($Đ$=1.6), which is due to the interaction of the polar PDEAEMA block with the SEC column, leading to longer retention time.

1.2.5.1.4 Characterization of the membranes

The structure of the PDEAEMA-CTA was confirmed by ^{1}HNMR spectroscopy, as shown in Figure S1(a). The peaks (a, b, c, d, e and f) corresponding to the protons of PDEAEMA are clearly visible, indicating the polymerization of DMAEMA monomers initiated by the CTA. The outcome of the aminolysis of PDEAEMA was also measured by UV-vis spectroscopy using the characteristic absorption centred at 310 nm of the trithiocarbonate group. As seen in

Figure S1 (b), the original PDEAEMA displays a strong 310 nm absorption, while no absorption appears in this spectral region for PDEAEMA-SH, indicating the complete aminolysis of trithiocarbonate groups.

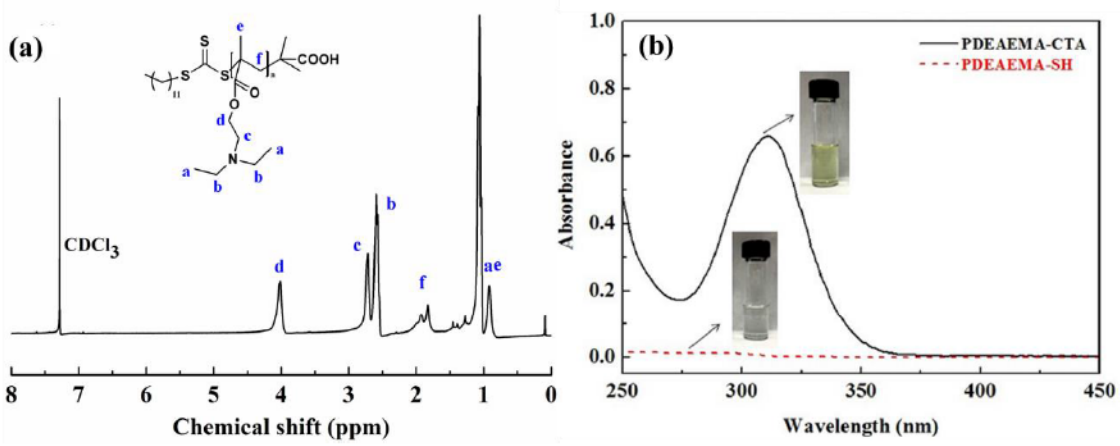

Figure S1. ^{1}H NMR spectra of (a) PDEAEMA-CTA in $CDCl_3$ and (b) UV-vis spectra of PDEAEMA-CTA (solid) and PDEAEMA-SH (dashed).

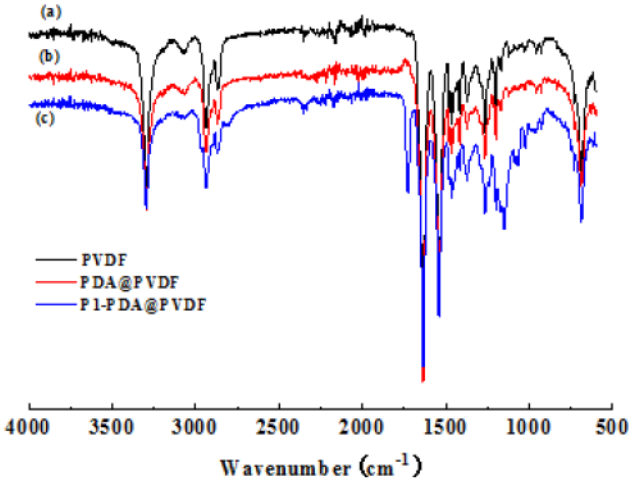

Figure S2. ATR-FTIR spectra: (a) PVDF membrane, (b) PDA@PVDF membrane, and (c) PDEAEMA-PDA@PVDF membrane.

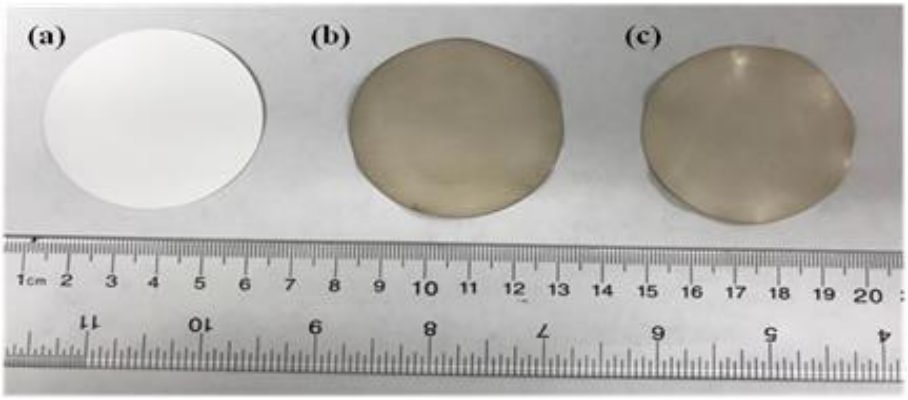

Figure S3. Photographs of (a) PVDF membrane, (b) PDA coated PVDF membrane and (c) PDEAEMA-PDA@PVDF membrane.

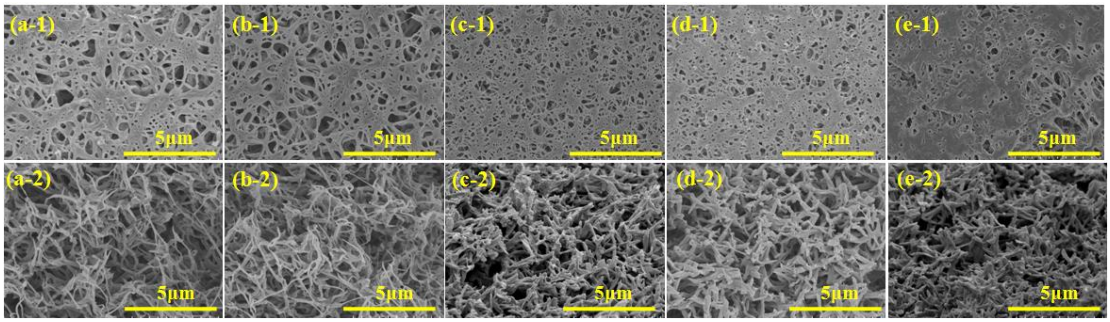

Figure S4. SEM images for (a-1and a-2) the PVDF membrane, (b-1and b-2) the PDA@PVDF membrane, (c-1and c-2) the P1-PDA@PVDF membrane, (d-1 and d-2) the P2-PDA@PVDF membrane, and (e-1 and e-2) the P3-PDA@PVDF membrane. Top: surface view, and bottom: cross-section view.

The SEM analysis was used to investigate the morphology of membranes. As shown in Figure S4, the pure PVDF membrane has an asymmetric structure with high pore density in the surface and spongy structure in the cross-section. There are no significant changes in morphology after modification, but the pore sizes of the membranes are reduced slightly after incorporation of functional polymers, which can be noticed in Figure S4(c)-(e). In addition, the similar morphology for all membranes suggests that incorporation of PDEAEMA chains did not destroy the asymmetric morphology of the pristine membrane.

1.2.5.2. Grafting Density and Degree of PDEAEMA

The grafting density of functional polymers on the modified membrane surface was described as the weight of polymer brushes per unit area of membrane, and the grafting degree was calculated according to the weight difference of membrane before and after Michael-Addition reaction, showed as the following equation:

$$\boldsymbol{Y} = \frac{\boldsymbol{W_1 - W_2}}{\boldsymbol{A}} \quad (1)$$

$$\boldsymbol{GD} = \frac{\boldsymbol{W_1 - W_2}}{\boldsymbol{W_2}} \times \mathbf{100} \quad (2)$$

where Y is grafting density of the PDEAEMA grafted onto the PDA@PVDF membrane (mg/cm^2), and W_1 and W_2 are the weight of PDA@PVDF membrane and PDEAEMA-PDA@PVDF (g), respectively, and A is the area of the membrane (cm^2).

The obtained grafting density and grafting degree of modified membranes were shown in Figure S5. It can be seen that the grafting density and degree of M1 membrane are higher than the other two membranes. This may be due to the fact that higher molecular weights (in M2 and M3) have longer polymer chains, which can bound to the surface and hinder the further attachment of chains in a localized area on the surface due to steric crowding.[4]

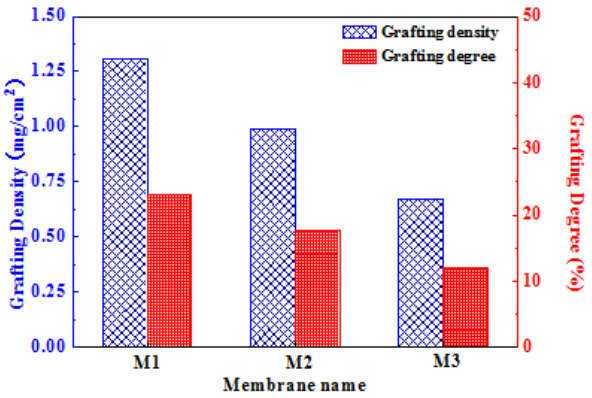

Figure S5. Grafting data of PDEAEMA-PDA@PVDF membranes (M1: P1-PDA@PDA

membrane; M2: P2-PDA@PDA membrane and M3: P3-PDA@PDA membrane)

1.2.5.3. Water Uptake Measurements

Water uptake was used to evaluate the adsorption of water of PDEAEMA-PDA@ PVDF membranes. Prepared membranes were rinsed with deionized water and then dried at 60 °C under vacuum for 24 h, and its weight (W_d) was taken. After that, the dried membranes were immersed in deionized water with bubbling CO_2 time of 5, 10, 15, 20, 25 and 30 min, and the weight of the wet membrane (W_s) was obtained. The water content of microfiltration membrane was calculated by the following relationship:

$$\textit{Water uptake}\ (\%) = \frac{W_s - W_d}{W_d} \times 100\% \qquad (3)$$

The water uptake (%) of each membrane was obtained by weight fraction of the membrane. In Figure S6, the water uptake (%) of the PDA@PVDF and PDEAEMA-PDA@PVDF membranes are all higher than that of the pristine one. For all PDEAEMA-PDA@PVDF membranes, the water uptake (%) increased with bubbling CO_2 time. This is because bubbling CO_2 can make the PDEAEMA chains protonated, enhancing the hydrophilicity of the membrane, and leading to more water absorption in the numerous pores in the membranes.

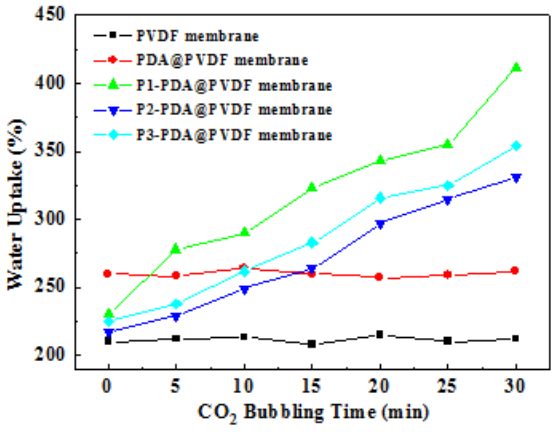

Figure S6. Water uptake (%) of PDEAEMA-PDA@PVDF membranes vs. CO_2 bubbling time.

It should be noted that if the membrane is a polymer that becomes more hydrophilic upon CO_2 bubbling, the increased water uptake can favor water flux. However, in the present study, the openness of the pores inside the PVDF membrane determines the water flux. When the PDEAEMA layer becomes protonated upon CO_2 bubbling, although the water uptake of the whole membrane increases, the pores are blocked by the soluble PDEAEMA chains of extended conformation, which leads to decrease in water flux (permeability).

1.2.5.4. Water Flux under CO_2/Ar Stimulation

To verify the effective gas-responsive gating function of PDEAEMA-PDA@PVDF membranes, water filtration was performed at 25 °C under CO_2/Ar. As shown in Figure S7, dead-end filtration cell with effective membrane area of 13.1 cm^2 was used. The trans-membrane pressure was kept 1 bar produced by vacuum. For CO_2 induced switching studies, the membrane was filtered with DI water first for a period of time to ensure a steady state. Then firstly bubbling CO_2 into solution for 30 min, next bubbling Ar for 20 min. Water flux samples were taken every 5 min. The flux was calculated from the volume of solution permeated per unit time and per unit area of the membrane surface. Water flux (J_w) was calculated as follow:

$$\boldsymbol{J_W = \frac{V}{A \cdot t \cdot \Delta P}} \quad (4)$$

where V is the volume of DI water (L), t is the permeation time (h), A is the membrane area and Δp is the trans-membrane pressure.

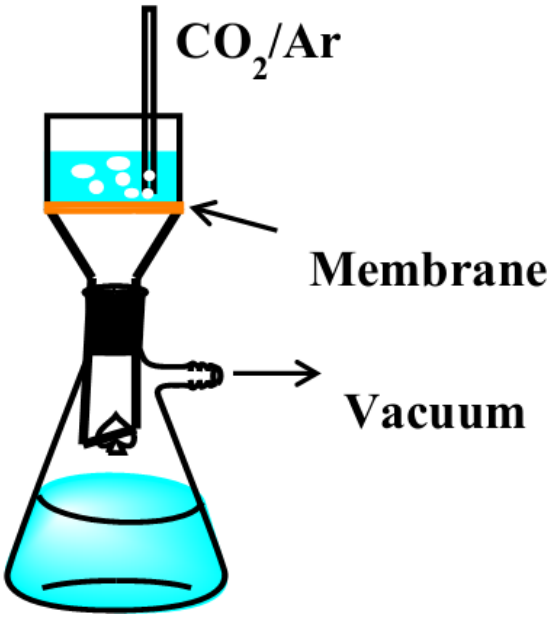

Figure **S7.** Experimental setup used for gas-responsive water flux measurements.

1.2.5.5. Repeated Cycles of AuNP Separation

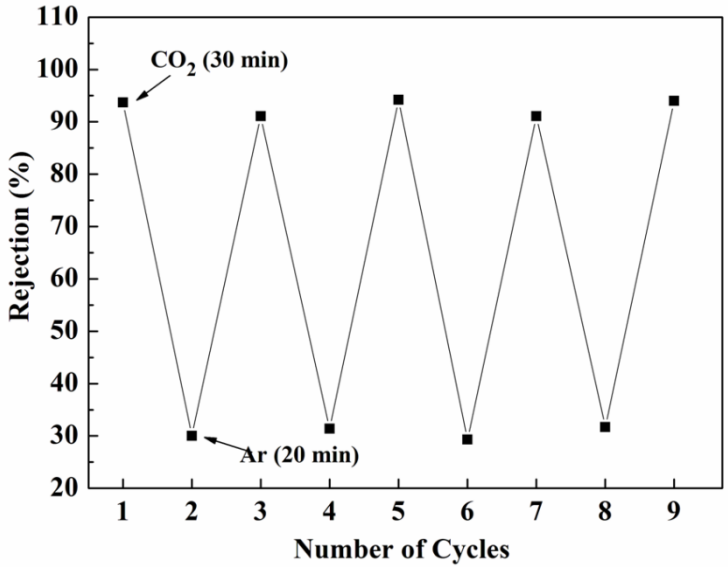

Figure S8. Cyclic change in rejection rate for AuNPs (50 nm) using the P1-PDA@PVDF membrane exposed alternately to 30 min CO_2 and 20 min Ar bubbling.

References

1. J. T. Lai, D. Filla and R. Shea, *Macromolecules*, 2002, **35**, 6754-6756.
2. Y. M. Ma, D. X. Wei, H. Yao, L. P. Wu and G. Q. Chen, *Biomacromolecules*, 2016, **17**, 2680-2690.
3. H. Kawasaki, T. Sugitani, T. Watanabe, T. Yonezawa, H. Moriwaki and R. Arakawa, *Anal. Chem.*, 2008, **80**, 7524-7533.
4. S. P. L. Masurier, G. Gody, S. Perrierand and A. M. Granville, *Polym. Chem.*, 2014, **5**, 2816-2823.

1.3. Summary of the Project

In this project, we have proposed a novel concept of CO_2-responsive polymer membranes with gas-tunable pore size for the first time. The PDEAEMA grafted on PDA@PVDF porous membrane can undergo reversible contraction/extension in response to CO_2/Ar, which control opening or closure of pore sizes of membranes and further impact the size selectivity of membrane. Subsequent the experiment of the rejection of AuNPs (50 nm) prove that this gas-tunable pore size can be very useful for size-selective separation or ‘‘valve’’ for on-demand passage of species of appropriate sizes. Compared with previous stimuli responsive membranes, the use of CO_2 as trigger is efficient for switching, environmentally friendly as well as cost-effective. Overall, such novel CO_2-responsive membranes with gas-tunable pore size and responsive size-selectivity show the greatly potential applications in microfluidic and other systems requiring tunable mass separation, or biomedical fields.

CHAPITRE 2. A CO_2-RESPONSIVE GRAPHENE OXIDE/POLYMER COMPOSITE NANOFILTRATION MEMEBR ANE FOR WATER PURIFICATION

2.1. About the Project

Nanofiltration membrane (NFM) technologies are one of the most important and effective strategies for addressing the water crisis because of their highly efficient, cost-effective, energy-saving, and environmentally sustainable attributes. Among various membrane materials for NFM, GO has been considered as promising one due to its zigzag nanochannels that allow water to permeate through while blocking ions or molecules larger than the interlayer spacing. However, the water flux of pure GO NFMs is usually low because of the narrow GO interlayer spacing (<0.8 nm). Some strategies have been adopted to increase the space between GO layers, such as insertion of organic molecules or nanostrands, but these strategies can decrease the retention performance of ions and organic dyes to some extent. Inspired by the work in Chapter 1, we also introduced the CO_2-responsive polymer, PDEAEMA, into GO NFM to design a CO_2 responsive NFM for the first time, with aim to not only solve the dilemma of pure GO NFM, but also achieve gas-tunable salt rejections. Such novel NFM has two unique features. One is that the use of a CO_2-responsive polymer in the NFM makes it possible to increase the space between GO layers and thus the water permeability with no detrimental effect on the rejection of dye molecules or without sacrificing too much on the rejections of ions in water in comparison to a pure GO membrane. Another is that the gas can convert the GO NFM from a negatively charged to a positively charged state, which makes the GO NFM suitable for water softening and metal ion removal, such as $MgCl_2$ removal. This work skillfully combines the merits of both CO_2-responsive polymers and GO-based NFMs, thus opening a door for the development of smart stimuli-responsive NFMs.

This work was published in *Journal of Materials Chemistry A*, **2018**, 6, 6875 by Liangliang

Dong, Weizheng Fan, Xia Tong, Hongji Zhang, Mingqing Chen and Yue Zhao. This research work was accomplished in the Université de Sherbrooke under the supervision of Prof. Zhao and co-supervision of Prof. Chen. I fabricated the poly(N,N-diethylaminoethyl methacrylate) bearing a pyrene end group (Py-PDEAEMA) and membrane samples (GO nanofiltration membranes and Py-PDEAEMA/GO nanofiltration membranes). Weizheng Fan and Xia Tong assisted me with SEC and AFM experiments, respectively. I performed all the other experiments and characterizations reported in the paper. Hongji Zhang gave me some useful advice about this project. I wrote the first draft of the manuscript. Prof. Zhao revised and finalized the manuscript.

2.2. Paper Published in Journal of Materials Chemistry A, 2018, 6, 6785.

A CO_2-responsive graphene oxide/polymer composite nanofiltration membrane for water purification

Liangliang Dong,[ab] Weizheng Fan,[b] Xia Tong,[b] Hongji Zhang,[a] Mingqing Chen*[a] and Yue Zhao*[b]

[a]Key Laboratory of Synthetic and Biological Colloids, Ministry of Education, School of Chemical and Material Engineering, Jiangnan University, 1800 Lihu Road, Wuxi 214122, P. R. China. E-mail: mqchen@jiangnan.edu.cn

[b]Département de chimie, Université de Sherbrooke, Sherbrooke, QC, J1K 2R1, Canada. E-mail: yue.zhao@usherbrooke.ca

2.2.1 Abstract

A “smart” graphene oxide (GO) based nanofiltration membrane was prepared through electrostatic and π-π interaction-driven complexation with poly(*N*,*N*- diethylaminoethyl methacrylate) bearing a pyrene end group (Py-PDEAEMA). The composite membranes show a number of attributes potentially appealing for water treatment. First, they display reversible, gas-tunable water permeability between the pore closure state under CO_2 stimulation and the pore opening state upon Ar bubbling. The water permeability remains much higher than that of a pure GO membrane even at the pore closure state. Secondly, the separation of organic dye molecules from water using this membrane is similarly efficient as that using a pure GO membrane despite the much higher water permeability. Finally, as a result of CO_2-induced reversal of the charge sign, the composite membrane shows an excellent trade-off between rejection of some salts like $MgCl_2$ and water permeability, with both much higher rejection and permeability compared to a pure GO membrane. This study of a CO_2-responsive, GO-based nanofiltration membrane, the first of its kind, demonstrates new perspectives in developing smart separation membranes for water purification.

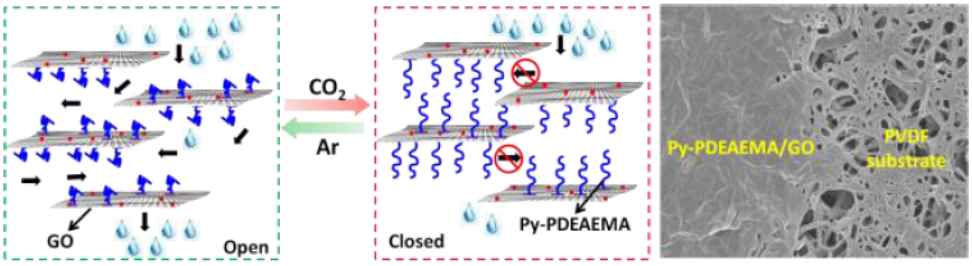

2.2.2 Introduction

As has been pointed out in the 2015 Global Risks Report, water crisis ranked top of ten global risks.[1] Among all the possible technologies for addressing the water crisis, nanofiltration technologies represent one of the most important and effective strategies due to their highly efficient, cost-effective, energy-saving, and environmentally sustainable attributes.[2-4] In recent years, GO as a 2D material with single atom layers has emerged as a promising membrane material for nanofiltration because of its easy accessibility, hydrophilicity, excellent mechanical strength, and high chemical and thermal stability.[5-7] Their zigzag nanochannels allow water to permeate through while blocking ions or molecules larger than the interlayer spacing.[8, 9] For instance, Han *et al.* reported ultrathin GO NFMs (22-53 nm thick) with 2D nanochannels by using a filtration-assisted assembly technique for water purification. The results showed that such membranes had >99% high retention for organic dyes and 60% retention for Na_2SO_4.[3] Wang *et al.* prepared novel GO-based NFMs on a highly porous poly-acrylonitrile nanofibrous mat (GO@PAN) for water treatment; the membrane showed nearly 100% rejection for the congo red dye and 56.7% rejection for Na_2SO_4.[10] However, the water flux of pure GO membranes is usually low due to the narrow GO interlayer spacing (<0.8 nm). An effective strategy to tackle this problem is to increase the space between GO layers by insertion of organic molecules or nanostrands.[11-16] This strategy, however, has a negative impact by weakening the retention performance of ions and organic dyes to some extent. Therefore, the challenge remains as to developing GO membranes that have simultaneously high water flux and rejection performance.

On the other hand, stimuli-responsive porous membranes have triggered much interest in membrane separation. In response to external stimuli, such as temperature, pH, light, magnetic field and redox agents, these “smart” membranes can undergo a conformational or structural or morphological switch to tune the pore sizes and/or the surface properties, which, in turn, controls the permeability and separation selectivity of the membranes.[17,18] CO_2 gas, as an abundant,

nontoxic and renewable resource, has been increasingly explored as a "green" stimulus in developing smart or switchable functional materials. To date, various types of CO_2-responsive polymers have been successfully synthesized and used for showcasing applications in biomedical delivery, sensors, catalysts and adhesives.[19-29] Compared with other stimuli, CO_2 possesses some unique features that make it particularly appealing in switchable or tunable membrane technologies. First, unlike thermal stimulation, which needs heating or cooling to adjust the temperature of the membrane environment, CO_2-responsive polymers can realize conformational transition in water by simple addition or removal of CO_2. Secondly, differing from pH-, ionic strength- or redox-based switching,[30-33] which require repeated addition of chemical species into the solution and thus result in accumulation of salts or other chemicals, CO_2-responsive polymers can be switched in as many cycles as needed without any contamination. Finally, CO_2-responsive polymers can show responsive behavior deep inside the material since CO_2 has a good penetration depth in the presence of water, which allows the CO_2-responsive polymer to overcome the depth limitation problem often experienced with light- or magnetic-responsive polymers.[34] Despite the potential advantages of CO_2-stimulable separation membranes, only a few studies have been reported to date.[22, 23, 35-37] And to the best of our knowledge, no CO_2-responsive, GO-based nanofiltration membrane has been reported until now.

Herein, we report the fabrication of CO_2-responsive polymer-intercalated GO NFMs using a simple vacuum filtration process. Their gas-switchable water permeability and the concomitant effect on the separation of dye molecules and salt ions were also investigated. This novel NFM has two unique features. First, as compared to a pure GO membrane, the use of a CO_2-responsive polymer in the composite membrane makes it possible to increase the space between GO layers and thus the water permeability with no detrimental effect on the retention of dye molecules or without compromising too much on the retention of ions in water. Next, while using CO_2 to switch the polymer chain conformation and thus tune the effective GO interlayer spacing, the gas converts the GO NFM from a negatively charged to a positively charged state, which is preferred for water softening and metal ion removal.[38-40] PDEAEMA is an effective

CO_2-responsive polymer, the tertiary amine groups of which can be protonated upon bubbling CO_2 into water and subsequently deprotonated upon removal of CO_2 by bubbling Ar or N_2 into the solution.[19, 41, 42] This allows the polymer to switch between the positively charged hydrophilic state with extended chain conformation and the neutral hydrophobic state with collapsed chain conformation. This gas-switchable conformational change can be repeated for many cycles without chemical contamination of the solution. This robust property motivated us to select PDEAEMA as the CO_2-responsive polymer in fabricating the GO composite NFM with the switchable water permeability and excellent separation performance.

2.2.3 Results and Discussion

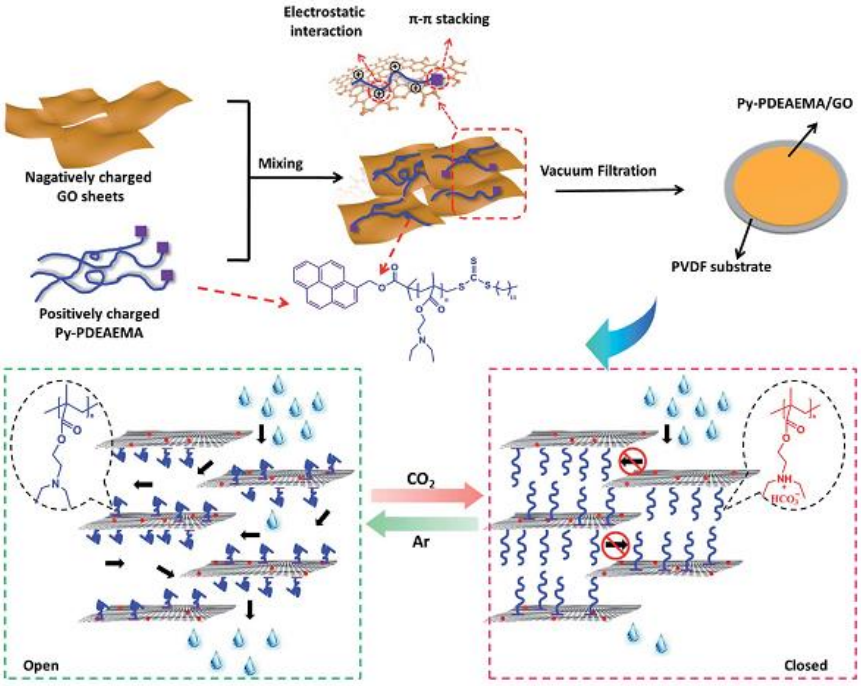

Figure 1. Schematic illustration of the fabrication process of the CO_2-switchable Py-PDEAEMA/GO NFM and its gas-tunable water gating properties. Upper part: Py-PDEAEMA and GO form a stable aqueous dispersion through the π-π interaction (pyrene and graphene) and electrostatic interaction (positively charged polymer and negatively charged GO), and then the membrane is prepared through vacuum filtration of the aqueous dispersion. Lower part: the water permeability of the Py-PDEAEMA/GO NFM decreases upon bubbling CO_2 due to the

narrowed water flow channel caused by the swollen Py-PDEAEMA chains, and increases upon bubbling Ar because of the opening channel of the membrane as a result of the collapsed Py-PDEAEMA chains.

To ensure the complexation between PDEAEMA and GO, we synthesized pyrene-terminated PDEAEMA (Py-PDEAEMA) through esterification of 2-(dodecylthiocarbonothioylthio)-2-methylpropionic acid (DDMAT) with pyrenemethanol that was then used for the reversible addition-fragmentation chain transfer (RAFT) polymerization of DEAEMA (synthetic details in Supporting Information Scheme S1, Table S1, Figure S1 and S2). To prepare the GO/polymer membrane, Py-PDEAEMA was dissolved in water under CO_2 bubbling and mixed with GO. Stable aqueous dispersions with a range of mass ratios of Py-PDEAEMA to GO ($R_{P/G}$) were obtained, thanks to the π-π interaction (between pyrene and graphene) and electrostatic interaction (between the positively charged polymer and negatively charged GO) (Figure S3 and S4). A series of Py-PDEAEMA/GO NFMs with different $R_{P/G}$ values were prepared by vacuum filtration of the mixed dispersions through a polyvinylidene fluoride microfiltration membrane (PVDF) (Figure 1). After drying in a vacuum, the obtained Py-PDEAEMA/GO NFMs (including a neat GO NFM as a control) with a diameter of 4.1 cm show excellent flexibility (Figure 2a). The scanning electron microscopy (SEM) images of the cross-section of Py-PDEAEMA/GO NFMs show a typical laminated structure without obvious aggregates. The average thickness of Py-PDEAEMA/GO NFMs is 60 nm, which is larger than that of the neat GO membrane (50 nm) (Figure S5). The SEM images of the surfaces of Py-PDEAEMA/GO NFMs show a smooth and uniform state (Figure 2b, c). From the height profile of the AFM image, the average thickness of the Py-PDEAEMA/GO was estimated to be about 1.7 nm (Figure 2d). What's more, the material loss of all Py-PDEAEMA/GO NFMs was lower than 6 wt%, implying that nearly all of the GO and Py-PDEAEMA were retained in the prepared membranes (Figure 2f). The presence of Py-PDEAEMA in the Py-PDEAEMA/GO NFMs is also confirmed by infrared spectroscopy observations (Figure S7). The above results confirm that GO complexed with Py-PDEAEMA has been uniformly and continuously co-deposited on the

PVDF microfiltration membrane during the vacuum filtration, leading to the formation of Py-PDEAEMA/GO NFMs.

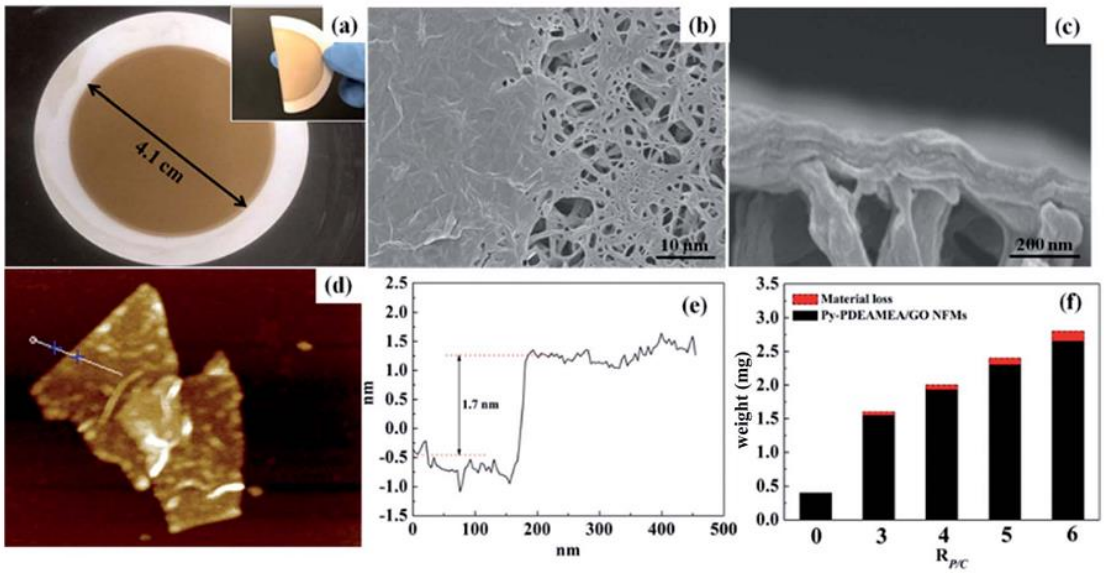

Figure 2. (a) Photograph of the Py-PDEAEMA/GO NFM on a PVDF microfiltration membrane. (b) SEM image (top view) of the coating of Py-PDEAEMA/GO on half of the surface of a PVDF microfiltration membrane, showing a clear boundary between the uniform and smooth surface of Py-PDEAEMA/GO sheets on the left and the porous surface structure of uncoated PVDF on the right. (c) Cross-sectional SEM image of Py-PDEAEMA/GO NFMs. (d and e) AFM images and the corresponding height pro files of Py-PDEAEMA/GO. In all cases, the used Py-PDEAEMA sample has M_n=13 500 g mol^{-1} and $R_{P/G}$ is 6 (f) comparison of the weight of the raw material used for vacuum filtration and the measured weight of dried Py-PDEAEMA/GO NFMs. All samples were prepared with 0.4 mg of GO and the corresponding amount of Py-PDEAEMA, and the weight difference represents Py-PDEAEMA and GO loss during filtration. The material loss for Py-PDEAEMA/GO NFMs with an $R_{P/G}$ of 3, 4, 5 and 6 was calculated to be 3.1 wt%, 3.5 wt%, 4.1 wt% and 5.3 wt%, respectively. Note that $R_{P/G}$=0 represents a polymer-free, neat GO membrane. In this case the used Py-PDEAEMA sample has M_n = 13 500g mol^{-1}.

Before assessing the separation performance of our Py-PDEAEMA/GO NFMs towards dyes

and ions in water, we investigated the effect of the intercalated polymer on the water permeability as well as the water flux tunability upon addition and removal of CO_2. Firstly, the effect of the thickness of the neat GO membrane on pure water permeability was studied. All pure water permeability measurements were carried out after the steady state was reached, typically after half an hour (Figure 3a). Since the largest steady-state water permeability was observed for the neat GO membrane prepared with 4 mL of GO suspension, being 8.1 L m^{-2} h^{-1} bar^{-1}, while thicker GO membranes prepared with larger volumes of GO suspension displayed lower water permeability (Figure S8), we chose 4 mL of GO suspension (0.1 mg mL^{-1}) as the optimum volume for preparing the Py-PDEAEMA/GO NFMs. The water permeability was measured systematically for the membranes with different $R_{P/G}$ values using the same Py-PDEAEMA (M_n = 13 500 g mol^{-1}) and for the membranes with different molecular weights of Py-PDEAEMA at a given $R_{P/G}$. In what follows, Py-PDEAEMA/GO NFMs with different molecular weights of Py-PDEAEMA (Table S1) are denoted as **membrane-1**, **membrane-2** and **membrane-3**. As shown in Figure 3b, with increasing $R_{P/G}$, the water permeability of Py-PDEAEMA/GO NFMs gradually increased. This is because the addition of Py-PDEAEMA enlarges the space between GO layers (Figure S9), and thus facilitates the transport of water through the membrane. Meanwhile, the higher molecular weight of Py-PDEAEMA (membrane-3) had the effect of an increased GO layer spacing, leading to higher water permeability (Figure 3c). **Membrane-3** with $R_{P/G}$ = 6 had the maximum water permeability of 53.6 L m^{-2} h^{-1} bar^{-1}, which is about 6.6 times greater than that of the pure GO membrane. Unless otherwise stated, this membrane was utilized for CO_2-switchable water permeability and separation measurements. Theoretically, based on slip flow theory,[43] the oxygen-containing groups of GO sheets would hinder the transport of water molecules due to the strong interaction between them. Thus only GO regions without such functional groups can facilitate the transport of water. After being tethered by Py-PDEAEMA, a large amount of the hydrophilic functional groups on GO may be covered by the polymer chains, which also contributes to the increase in water permeability.

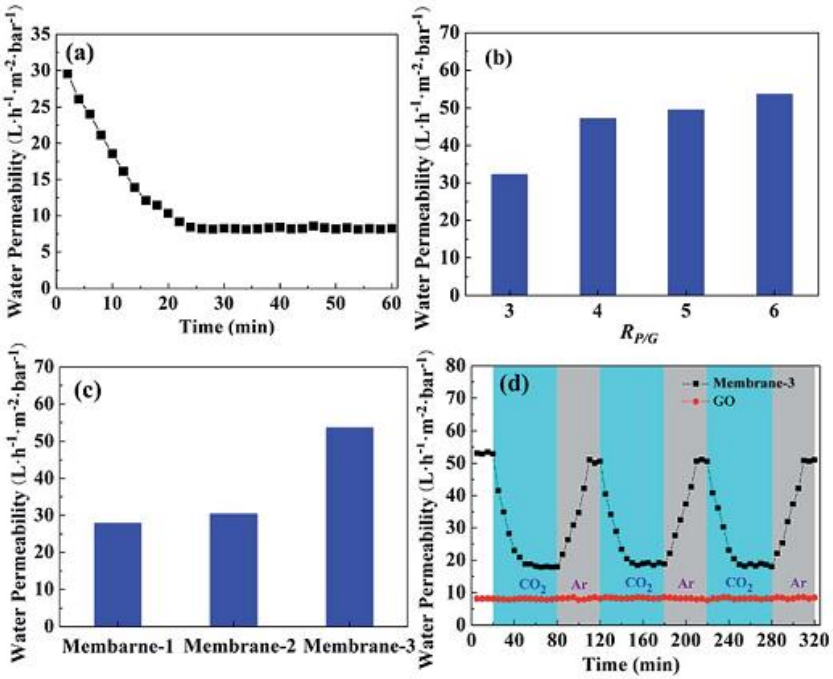

Figure 3. (a) Variation of pure water permeability over time for the pure GO membrane with 0.4 mg of GO under a pressure of 1 bar. (b) Steady-state water permeability of **membrane-3** with different $R_{P/G}$ values. (c) Steady-state water permeability of Py-PDEAEMA/GO NFMs with different molecular weights (increasing from 1 to 3, Table S1) at $R_{P/G}$ = 6. (d) Reversible water permeability switch of **membrane-3** with $R_{P/G}$ = 6: decrease and recovery upon CO_2 and Ar bubbling, respectively. Data obtained under the same conditions for the non-gas-responsive pure GO membrane are shown for comparison.

We went on to investigate how the water permeability of the Py-PDEAEMA/GO NFMs can be switched by alternating injection of CO_2 and Ar into the solution, using a vacuum filtration system under 1 bar. Figure 3d shows the results obtained with **membrane-3** with $R_{P/G}$ = 6. When CO_2 was bubbled through the solution, the water permeability decreased gradually until a plateau was reached after 30 min, while the pure GO membrane showed no change under the same CO_2 stimulation. After 30 min of CO_2 bubbling, the water permeability dropped by 66.0%, but was still much higher than that of the pure GO membrane. Subsequently, when Ar was bubbled into the solution, the water permeability was recovered to the initial level, at a rate

similar to that of water permeability decrease upon CO_2 treatment. The working mechanism of this reversible variation of water permeability for the membrane by CO_2/Ar bubbling basically is what is depicted in Figure 1. At room temperature and pH=7, Py-PDEAEMA chains are insoluble in water, being in the collapsed state, and thus the membrane is "open" to water flow. Upon passing CO_2 through the solution, the tertiary amine groups in Py-PDEAEMA are protonated, which renders the polymer soluble in water. When this happens, the polymer chains of extended conformation fill in the space between GO sheets to close the membrane's path and, consequently, decrease the water permeability. Subsequently, passing Ar through the solution can remove CO_2 and brings Py-PDEAEMA chains back to the insoluble state, which reopens the pores of the membrane and allows the water permeability to be recovered. According to the classical Hagen-Poiseuille equation, the permeation flux, J, is determined as follows:

$$\boldsymbol{J = \varepsilon A r_p^2 \Delta P / 8 \mu L} \qquad (1)$$

where ε is the surface porosity, μ is the water viscosity, A is the membrane area, and L is the total distance of water running through the membrane. The permeation flux is directly proportional to the square of the membrane pore radius, r_p.[44] Therefore, the decreased water permeability after bubbling CO_2 indicates a reduced pore size. The complete water permeability recovery after Ar bubbling implies that the pore size increases to the initial state. This is in accordance with our hypothesis that CO_2/Ar can control the pore opening and closure states of the Py-PDEAEMA/GO NFMs.

We then moved on to studying the possible control of the separation performance of Py-PDEAEMA/GO NFMs using CO_2/Ar stimulation for organic dyes and ions in water. On the one hand, solutions with two dye molecules, rhodamine B (RB) and methyl orange (MO), respectively, were utilized for the retention measurements of **membrane-3** with $R_{P/G}$ = 6 (performed under a pressure of 1 bar) and changes in the dye concentrations of the permeates and feed solutions could readily be monitored from the UV-vis absorption spectra. Four cycles of alternating bubbling of CO_2 for 30 min and Ar for 40 min were applied to each dye solution,

and the dye rejection rate and the permeability were measured after each gas treatment. As can be seen from the results given in Figure 4a, while the water permeability swings between 13.6 L m^{-2} h^{-1} bar^{-1} and 48.5 L m^{-2} h^{-1} bar^{-1} upon CO_2 and Ar bubbling, respectively, as a result of the gas-controlled closure and opening of the membrane pores, the switch of dye rejection is very small. Regardless of the water permeability, the membrane's rejection rate for the two dyes remains very high: in average 98.9% and 96.5% for RB and MO, respectively. This result shows that the gas-tunable membrane pore opening state for high water permeability has no detrimental effect on the separation performance of the membrane towards the organic dyes in water. The nearly complete retention of the dyes is preserved with the Py-PDEAEMA/GO membrane even at the full pore opening state with water permeability several times that of the pure GO membrane.

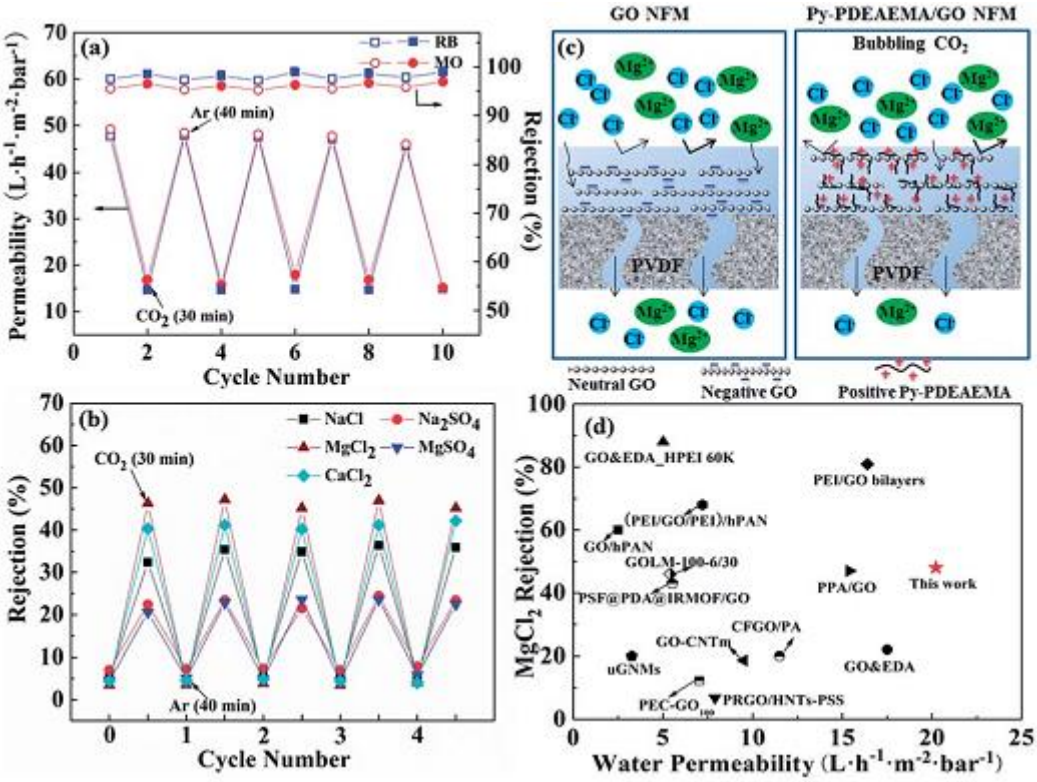

Figure 4. Separation performance and gas tunable behavior of **membrane-3** with $R_{P/G}$=6 under alternating CO_2/Ar stimulation (filtration measurements conducted at a pressure difference of

1 bar): (a) rejection of dye molecules and permeability switch of dye solutions and (b) switchable rejection of salts in water. (c) Schematic illustration of the comparison between Py-PDEAEMA/GO and neat GO NFMs, showing the effect of CO_2-induced charge sign reversal on the rejection of salts like $MgCl_2$. (d) Comparison of pure water permeability and $MgCl_2$ rejection of **membrane-3** with those of recently reported GO-based NFMs: mGNMs,[3] GO&EDA_HPEI60K and GO&EDA,[7b] GO-CNTm,[11] PSF@PDA@IRMOF/GO,[40] CFGO/PA,[47] (PEI/GO/PEI)/hPAN,[48] PEC-GO_{100},[49] PRGO/HNTs-PSS,[50] GOLM-100-6/30,[51] PPA/GO,[52] PEI/GO bilayers[53] and GO/hPAN.[54]

Finally, **membrane-3** with $R_{P/G}$ = 6 was also used to investigate the gas-switchable separation of ions from water. A series of four salts were chosen for the study, and the results of their rejection rate in response to four cycles of alternating bubbling of CO_2 (30 min) and Ar (40 min) are shown in Figure 4b. With the polymer chains in the collapsed state (before CO_2 bubbling or after Ar bubbling), the rejection for all salts is very low, implying that at the pore opening state, the spacing between the GO sheets of the Py-PDEAEMA/GO NFM is too large to prevent the passage of ions in water. Interestingly, after bubbling CO_2 that leads to the pore closure state with extended polymer chains, the membrane displayed good salt rejection, especially for $MgCl_2$, reaching a rejection rate of 48.0%. Upon close inspection of the results, it appears clear that the steric hindrance of the membrane pore closing state is not the only factor that accounts for the ion rejection. Overall, the rejection for the ions in Figure 4b follows an order of $R(MgCl_2) > R(CaCl_2) > R(NaCl) > R(MgSO_4) > R(Na_2SO_4)$, and the separation performance is typical to that of positively charged NFMs.[7b] After CO_2 bubbling, the PDEAEMA chains complexed with GO are protonated, becoming positively charged. The salt rejection mechanism of charged NFMs is usually explained by the combination of Donnan exclusion and steric hindrance effects.[45,46] Based on Donnan exclusion theory, the Donnan potential at the inter-phase between the solution and the membrane is prone to exclude co-ions that have the same charge as the membrane. In order to maintain the electrical neutrality of the solution on each side of the membrane, the counter ions that have the opposite charge to the membrane

are also rejected. Therefore, the retention of salts is sensitive to the valences of the cationic (Z^+) and anionic (Z^-) species of the salts. Donnan theory provides the following equation for the rejection of salts:

$$\boldsymbol{R = 1 - C_B^m / C_B = 1 - (|Z_B| C_B / |Z_B| C_B^m + C_X^m)^{|Z_B|/|Z_A|}} \quad (2)$$

where Z_B and Z_A are the valences of the co-ions and counter-ions, respectively, C_B and C_B^m the concentrations of the co-ions in the solution and membrane, respectively, and C_X^m is the membrane charge concentration. Generally, the rejection of a salt is determined by the exclusion of co-ions.[45] From eqn (2), it can be seen that a higher Z_B of the co-ions and a higher Z_B/Z_A ratio between the co-ions and counter-ions lead to a better retention of the salt. For instance, for the retention of $MgCl_2$, the positively charged NFM is usually better than the negatively charged NFM. This is because Mg^{2+} is the co-ion and the Z_B/Z_A is 2 for positively charged NFM (the valence ratio is 0.5 for the negatively charged NFM). In the present work, in order to better understand the effect of CO_2 bubbling on the retention of ions, we also measured the rejection of the same salts using a neat GO NFM that is known to be a negatively charged membrane.[3] The results plotting rejection vs. Z_B/Z_A show a reverse trend of separation performance towards the used salts, with the highest rejection for Na_2SO_4 (58%) and the lowest rejection for $MgCl_2$ (20%) (Figure S11). This is in line with the typical retention efficiency of the negatively charged NFM.[10] We measured the ζ-potentials of the GO and Py-PDEAEMA/GO dispersions in water prior to the membrane formation through vacuum filtration. As shown in Figure S12, while neat GO was highly negatively charged, Py-PDEAEMA/GO after CO_2 bubbling became highly positively charged, which confirms the charge sign reversal of the Py-PDEAEMA/GO membrane upon CO_2 bubbling. Therefore, passing CO_2 through water not only can close the pore of the Py-PDEAEMA/GO NFM arising from the polymer chain conformational change but also renders the membrane positively charged due to the protonation of tertiary amine groups on the polymer chains (Figure 4c). The combined effect makes the composite membrane highly suitable for retention of salts like $MgCl_2$. With respect to the neat GO membrane, both

the water permeability and the ion rejection rate of the Py-PDEAEMA/GO membrane are doubled. Figure 4d and S13 show a comparison of the $MgCl_2$ and NaCl rejection using our membrane with, to our knowledge, recently reported GO-based NFMs. Under a pressure of 1 bar, the Py-PDEAEMA/GO NFM (**membrane-3** with $R_{P/G} = 6$) upon CO_2 bubbling for 30 min has the highest water permeability and a very good rejection at the same time. The excellent trade-off between the flux and rejection makes the CO_2-switchable Py-PDEAEMA/GO NFM appealing for water purification by removing salts like $MgCl_2$.

2.2.4. Conclusions

In summary, we have prepared a new kind of stimuli-responsive NFM by complexing GO with Py-PDEAEMA. We show that the Py-PDEAEMA/GO membrane exhibits reversible, gas-tunable water permeability, which remains much higher than that of a pure GO membrane even at the pore-closure state with extended polymer chain conformation under CO_2 stimulation. Interestingly, even with the largest water permeability at the pore opening state with collapsed polymer chains upon removal of CO_2 by Ar bubbling, the Py-PDEAEMA/GO NFM shows very high rejection of dye molecules in water. Moreover, bubbling CO_2 into the solution renders the Py-PDEAEMA/GO membrane positively charged, in contrast with a negatively charged pure GO membrane, which leads to a high rejection rate of $MgCl_2$ and, at the same time, excellent water permeability, among the highest known to date. Our Py-PDEAEMA/GO NFM nicely integrates the merits of both CO_2-responsive polymers and GO-based NFMs, thus opening a door for the development of smart stimuli-responsive NFMs.

Conflicts of interest

There are no conflicts to declare.

Acknowledgements

Y. Z. acknowledges the financial support from the Natural Sciences and Engineering Research

Council of Canada (NSERC) and le Fonds de recherche du Québec: Nature et technologies (FRQNT). L. L. D. thanks China Scholarship Council (CSC) for awarding him a scholarship. M. C. thanks the National Natural Science Foundation of China (NNSFC) for financial support (No.51173072 and No. 21571084). H. Z. acknowledges the financial support from NNSFC (No. 21504031) and the Natural Science Foundation of Jiangsu Province (No. BK20150135).

Notes and references

1. E. B. Eide, *Global risks*, World Economic Forum, Geneva, 2015.
2. S. J. Gao, H. L. Qin, P. P. Liu and J. Jin, *J. Mater. Chem. A*, 2015, **3**, 6649.
3. Y. Han, Z. Xu and C. Gao, *Adv. Funct. Mater.*, 2013, **23**, 3693.
4. R. R. Choudhury, J. M. Gohil, S. Mohantya and S. K. Nayak, *J. Mater. Chem. A*, 2018, **6**, 313.
5. R. R. Hu, Y. J. He, C. M. Zhang, R. J. Zhang, J. Li and H. W. Zhu, *J. Mater. Chem. A*, 2017, **5**, 25632.
6. H. B. Huang, Z. G. Song, N. Wei, L. Shi, Y. Y. Mao, Y. L. Ying, L. W. Sun, Z. P. Xu and X. S. Peng, *Nat. Commun.*, 2013, **4**, 2979.
7. (a) Y. Zhang and T. S. Chung, *Curr. Opin. Chem. Eng.*, 2017, **16**, 9; (b) Y. Zhang, S. Zhang and T. S. Chung, *Environ. Sci.Technol.*, 2015, **49**, 10235.
8. R. R. Nair, H. A. Wu, P. N. Jayaram, I. V. Grigorieva and A. K. Geim, *Science*, 2012, **335**, 442.
9. S. K. Kannam, B. D. Todd, J. S. Hansen and P. J. Daivis, *J. Chem. Phys.*, 2012, **136**, 244704.
10. J. Q. Wang, P. Zhang, B. Liang, Y. X. Liu, T. Xu, L. F. Wang, B. Cao and K. Pan, *ACS Appl. Mater. Interfaces*, 2016, **8**, 6211.
11. Y. Han, Y. Q. Jiang and C. Gao, *ACS Appl. Mater. Interfaces*, 2015, **7**, 8147.
12. S. J. Gao, H. L. Qin, P. P. Liu and J. Jin, *J. Mater. Chem. A*, 2015, **3**, 6649.
13. W. T. Wang, E. Eftekhari, G. S. Zhu, X. W. Zhang, Z. F. Yan and Q. Li, *Chem. Commun.*, 2014, **50**, 13089.
14. X. F. Chen, M. H. Qiu, H. Ding, K. Y. Fu and Y. Q. Fan, *Nanoscale*, 2016, **8**, 5696.

15. L. Wang, X. H. Guo, K. C. Cao, B. Li, Y. Li, M. C. Zhang, R. Wen, X. Li, S. J. Li and L. J. Ma, *J. Mater. Chem. A*, 2017, **5**, 8051.
16. B. Lian, J. Deng, G. Leslie, H. Bustamante, V. Sahajwalla, Y. Nishina and R. K. Joshi, *Carbon*, 2017, **116**, 240.
17. Z. Liu, W. Wang, R. Xie, X. J. Ju and L. Y. Chu, *Chem. Soc. Rev.*, 2016, **45**, 460.
18. Z. G. Wang, X. P. Yao and Y. Wang, *J. Mater. Chem.*, 2012, **22**, 20542.
19. D. H. Han, X. Tong, O. Boissiere and Y. Zhao, *ACS Macro Lett.*, 2012, **1**, 57.
20. Q. Zhang, L. Lei and S. P. Zhu, *ACS Macro Lett.*, 2017, **6**, 515.
21. K. J. Boniface, R. R. Dykeman, A. Cormier, H. B. Wang, S. M. Mercer, G. Liu, M. F. Cunningham and P. G. Jessop, *Green Chem.*, 2016, **18**, 208.
22. Y. F. Cai, W. M. Shen, R. Wang, W. B. Krantz, A. G. Faneand and X. Hu, *Chem. Commun.*, 2013, **49**, 8377.
23. H. L. Che, M. Huo, L. Peng, T. Fang, N. Liu, L. Feng, Y. Wei and J. Y. Yuan, *Angew. Chem., Int. Ed.*, 2015, **54**, 8934.
24. H. B. Liu, W. Wang, H. Y. Yin and Y. J. Feng, *Langmuir*, 2015, **31**, 8756.
25. W. B. Zhang and C. Y. Gao, *J. Mater. Chem. A*, 2017, **5**, 16059.
26. Z. R. Guo, Y. J. Feng, Y. Wang, J. Y. Wang, Y. F. Wu and Y. M. Zhang, *Chem. Commun.*, 2011, **47**, 9348.
27. Y. Hoshino, K. Imamura, M. C. Yue, G. Inoue and Y. Miura, *J. Am. Chem. Soc.*, 2012, **134**, 18177.
28. J. Glasing, J. Bouchard, P. G. Jessop, P. Champagne and M. F. Cunningham, *Polym. Chem.*, 2017, **8**, 6000.
29. H. B. Liu, S. J. Lin, Y. J. Feng and P. Theato, *Polym. Chem.*, 2017, **8**, 12.
30. G. T. Rochelle, *Science*, 2009, **325**, 1652.
31. J. C. Hicks, J. H. Drese, D. J. Fauth, M. L. Gray, G. Qi and C. W. Jones, *J. Am. Chem. Soc.*, 2008, **130**, 2902.
32. N. Du, H. B. Park, G. P. Robertson, M. M. Dal-Cin, T. Visser, L. Scoles and M. D. Guiver, *Nat. Mater.*, 2011, **10**, 372.

33. J. Pinaud, E. Kowal, M. Cunningham and P. Jessop, *ACS Macro Lett.*, 2012, **1**, 1103.
34. Q. Yan and Y. Zhao, *Chem. Commun.*, 2014, **50**, 11631.
35. L. L. Dong, W. Z. Fan, H. J. Zhang, M. Q. Chen and Y. Zhao, *Chem. Commun.*, 2017, 53, 9574.
36. Q. Zhang, Z. W. Wang, L. Lei, J. Tang, J. L. Wang and S. P. Zhu, *ACS Appl. Mater. Interfaces*, 2017, **9**, 44146.
37. L. Lei, Q. Zhang, S. X. Shi and S. P. Zhu, *Langmuir*, 2017, **33**, 11936.
38. Y. Lv, Y. Du, Z. X. Chen, W. Z. Qiu and Z. K. Xu, *J. Membr. Sci.*, 2018, **545**, 99.
39. R. N. Zhang, Y. L. Su, X. T. Zhao, Y. F. Li, J. J. Zhao and Z. Y. Jiang, *J. Membr. Sci.*, 2014, **470**, 9.
40. Z. Rao, K. Feng, B. B. Tang and P. Y. Wu, *ACS Appl. Mater. Interfaces*, 2017, **9**, 2594.
41. A. Feng, C. Zhan, Q. Yan, B. Liu and J. Y. Yuan, *Chem. Commun.*, 2014, **50**, 8958.
42. Q. Yan and Y. Zhao, *J. Am. Chem. Soc.*, 2013, **135**, 16300.
43. H. B. Huang, Y. L. Ying and X. S. Peng, *J. Mater. Chem. A*, 2014, **2**, 13772.
44. X. S. Peng, J. Jin, Y. Nakamura, T. Ohno and I. Ichinose, *Nat. Nanotechnol.*, 2009, **4**, 353.
45. S. Bano, A. Mahmood, S. J. Kim and K. H. Lee, *J. Mater. Chem. A*, 2015, **3**, 2065.
46. F. Fornasiero, H. G. Park, J. K. Holt, M. Stadermann, C. P. Grigoropoulos, A. Noy and O. Bakajin, *Proc. Natl. Acad. Sci. U. S. A.*, 2008, **105**, 17250.
47. H. J. Zhang, B. Li, J. F. Pan, Y. W. Qi, J. N. Shen, C. J. Gao and B. V. Bruggen, *J. Membr. Sci.*, 2017, **539**, 128.
48. Q. Nan, P. Li and B. Cao, *Appl. Surf. Sci.*, 2016, **387**, 521.
49. Y. C. Wang, S. R. Kumar, C. M. Shih, W. S. Hung, Q. F. An, H. C. Hsu, S. H. Huang and S. J. Lue, *J. Membr. Sci.*, 2017, **540**, 391.
50. L. P. Zhu, H. X. Wang, J. Bai, J. D. Liu and Y. T. Zhang, *Desalination*, 2017, **420**, 145.
51. X. L. Xu, F. W. Lin, Y. Du, X. Zhang, J. Wu and Z. K. Xu, *ACS Appl. Mater. Interfaces*, 2016, **8**, 12588.
52. J. Wang, C. W. Zhao, T. Wang, Z. Wu, X. Li and J. D. Li, *RSC Adv.*, 2016, **6**, 82174.
53. T. Wang, J. R. Lu, L. L. Mao and Z. N. Wang, *J. Membr. Sci.*, 2016, **515**, 125.

54. Y. Oh, D. L. Armstrong, C. Finnerty, S. X. Zheng, M. Hu, A. Torrents and B. X. Mi, *J. Membr. Sci.*, 2017, **541**, 235.

2.2.5. Supporting Information

2.2.5.1. Synthesis

Materials: GO (produced by The Sixth Element Materials Technology Co., Ltd, China) was kindly provided by Prof. Hesheng Xia (Sichuan University). 1-Pyrenemethanol, *N*, *N'*-dicyclohexylcarbodiimide (DCC) and 4-dimethylaminopyridine (DMAP) were purchased from Aldrich and used without further purification. 2-(Diethylamino) ethyl methacrylate (DEAEMA, from Aldrich) was passed through an activated basic alumina column to remove the inhibitory substances. 2,2'-Azobis (2-methylpropionitrile) (AIBN) was recrystallized from methanol before use. The chain transfer agent of Py-DDMAT (2-(dodecylthiocarbonothioylthio)-2-methylpropionic acid) was synthesized according to a literature report.[44] Polyvinylidene fluoride microfiltration membranes (α-PVDF, mean pore size 220 nm, diameter 47 mm) were purchased from Shanghai Xingya Purification Material. Other chemical reagents were all commercially available and of analytical grade.

Synthesis of Py-PDEAEMA: The synthetic route is shown in Scheme S1. DEAEMA (3.33 g), AIBN (3.94 mg), Py-DMTA (36.43 mg) and THF (3 mL) were added into a Schlenk tube with a magnetic stir bar, and air was eliminated by a nitrogen flow for 20 min. Next, the solution was degassed by three freeze/vacuum/nitrogen cycles and then put into an oil bath at 70 °C for 6h, 12h and 24h, respectively. Subsequently, the mixture was diluted with THF and precipitated in cold hexane for three times. Finally, the obtained material was dried under vacuum overnight.

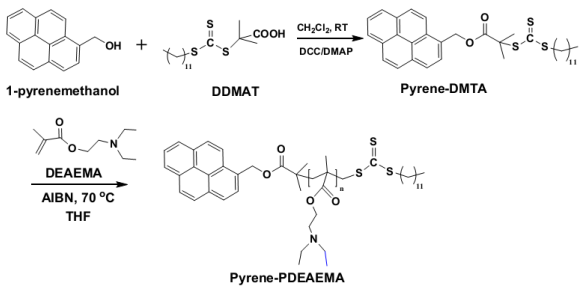

Scheme S1. Synthesis route of Py-PDEAEMA

2.2.5.2. Fabrication of Py-PDEAEMA/GO NFMs

The GO aqueous dispersion (0.1 mg/mL) was prepared by adding a certain amount of GO into water followed by 2h ultrasonication. Then, 15 mg of Py-PDEAEMA was firstly added into 15 mL of deionized water, followed by bubbling CO_2 until Py-PDEAEMA was completely dissolved in deionized water to form transparent Py-PDEAEMA aqueous solution (1 mg/mL). To fabricate Py-PDEAEMA/GO NFMs, 4 ml of GO aqueous solution (0.1 mg/mL) were initially mixed with a calculated amount of Py-PDEAEMA aqueous solution (1 mg/mL) for a desired mass ratio of Py-PDEAEMA to GO ($R_{P/G}$). The mixed solution was then diluted by water to a total volume of 20 mL and filtered on PVDF microfiltration membranes via vacuum filtration. After filtration, the samples were air-dried before use.

2.2.5.3. Characterizations

^{1}H NMR spectra were recorded on a Bruker 300 MHz using deuterated chloroform as the solvent and tetramethylsilane as the internal standard. Size exclusion chromatograph (SEC) measurements were performed on a Waters system equipped with a photodiode array detector (PDA 996) and a refractive index detector (RI 410). THF was used as the eluent at an elution rate of 1 mL/min, while polystyrene (PS) standards were used for calibration. Infrared spectra of the membranes were recorded on a FTIR between 800 and 4000 cm^{-1} at a resolution of 4cm^{-1}. The morphology of membranes was examined using a Hitachi S-4700 field-emission-gun scanning electron microscope (SEM) operating at 1.0 kV to 10.0 kV. For SEM observation, a fine platinum coating layer (a few nm) was deposited on sample surface by using a K550 sputter coater for 1 or 2 min. UV-visible spectra were obtained using an UV-vis-NIR spectrophotometer (Agilent Cary 50 Bio). Fluorescence emission spectra were recorded on a SPEX 1680 double-monochromator spectrometer. Atomic force microscopy (AFM) images were recorded on a

Dimension Icon AFM instrument equipped with a NanoScope V controller (Veeco/Digital Instruments, Santa Barbara, CA). AFM topographical images were obtained under ScanAsyst mode at room temperature using a silicon nitride cantilever tip (force constant 0.4 N/m). The ζ-potential was measured using a Malvern Zetasizer Nano ZS ZEN3600 system with a helium-neon laser (λ = 633 nm). XRD was performed on a D8 Advance X-ray diffractometer with Cu Kα radiation (λ = 0.15418 nm, Bruker, Germany). The average d-spacing within the GO layers was calculated by using the Bragg equation: $\lambda = 2d\sin\theta$, where λ is the wavelength of the X-ray beam, d is the spacing between adjacent GO layers, and θ is the diffraction angle.

2.2.5.4. Measurements of Pure Water Flux and Retention under CO_2/Ar Stimulation

Water filtration was performed at 25 °C under CO_2/Ar stimulation. A dead-end filtration cell with effective membrane area of 13.1 cm^2 was used. The trans-membrane pressure was kept at 1 bar produced by vacuum. For CO_2 induced switching studies, the membrane was first filtered with DI water for a period of time to ensure a steady state, then treated with CO_2 bubbling into solution for 30 min, and subsequently with Ar bubbling for 40 min. Water flux samples were taken every 5 min. The flux was calculated from the volume of solution permeated per unit time and per unit area of the membrane surface. Water flux (Jw) was calculated as follow:

$$\boldsymbol{J_w = \frac{V}{A \cdot t \cdot \Delta P}} \quad \text{(S1)}$$

where V is the volume of water (L), t is the permeation time (h), A is the membrane area and Δp is the transmembrane pressure. The rejection rate of organic dye molecules and salt in aqueous solution can be calculated using the following equation:

$$\boldsymbol{R = \left(1 - \frac{C_p}{C_f}\right) \times 100\%} \quad \text{(S2)}$$

where C_f is the dye or salt concentration in the feed solution (10 mg/L for dye concentration),

and *Cp* is the dye or salt concentration in the permeate solution. UV-vis-NIR spectrophotometer (Agilent Cary 50 Bio) was employed to measure the absorption spectra of dyes within the wavelength range of 200-700 nm using the standard absorbance vs, concentration calibration curve (linear correlation coefficient was 0.9999). The volume of feed solution for salt was 250 mL (2 mg/mL) and the salt concentration in solution was determined by conductivity meter (Cole-Parmer, 1481-90) based on the standard calibration curve (linear correlation coefficient was 0.9998).

2.2.5.5. Characterization Results

Table S1. Properties of the obtained Py-PDEAEMA[a]

Sample	*Mn (g/mol)*	*Mw (g/mol)*	*Đ*	*Yield (%)*
P1	6600	9500	1.4	75
P2	9600	15000	1.5	80
P3	13500	22300	1.6	85

[a]The apparently broad molecular weight distribution of the Py-PDEAEMA samples is likely to be caused by the interaction of the amine-containing polymer with the SEC column.

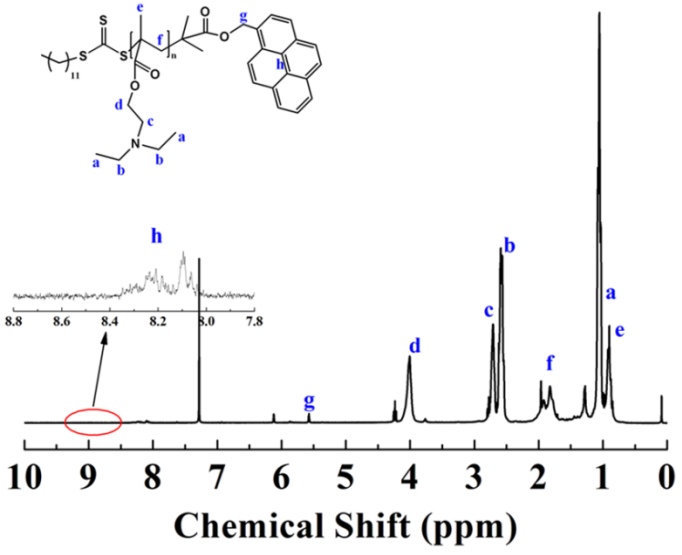

Figure S1. ^{1}H NMR of Py-PDEAEMA in $CDCl_3$

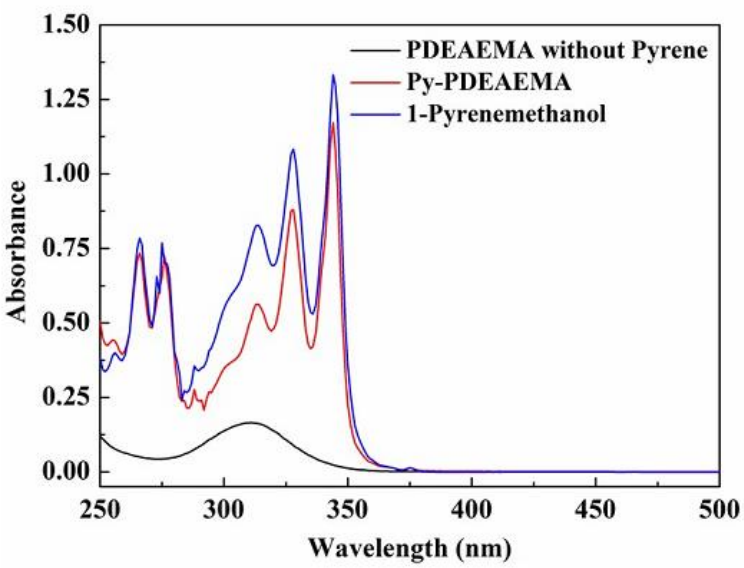

Figure S2. UV-vis absorption spectra of 1-pyrenemethanol and PDEAEMA with and without pyrene group. In this case, the molecular weight of Py-PDEAEMA is 13500 g/mol.

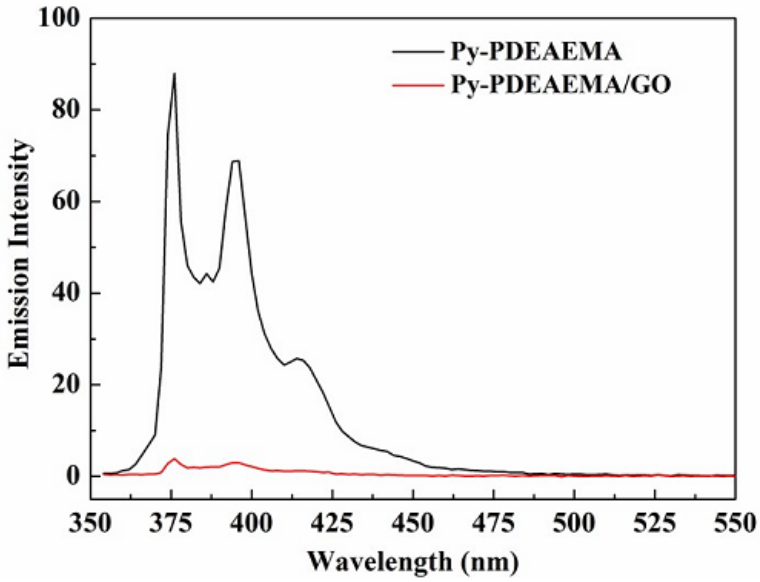

Figure S3. Fluorescence spectra (excited at 344 nm) of Py-PDEAEMA dispersion in water (under CO_2) and the mixture of Py-PDEAEMA/GO with $R_{P/G}$=6 in water. The sharp decrease of fluorescence intensity after mixing Py-PDEAEMA with GO is attributed to the complexation

due to electrostatic interaction between positively charged PDEAEMA and negatively charged GO as well as π-π interaction between pyrene and GO. In this case, the molecular weight of Py-PDEAEMA is 13500 g/mol.

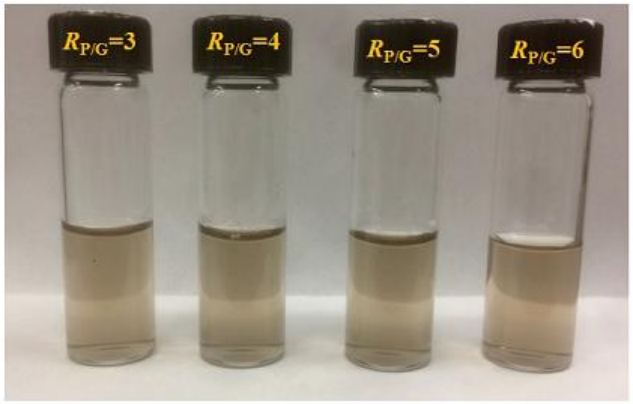

Figure S4. Photos of mixtures of Py-DEAEMA (M_n: 13,500 g/mol)/GO with different $R_{P/G.}$

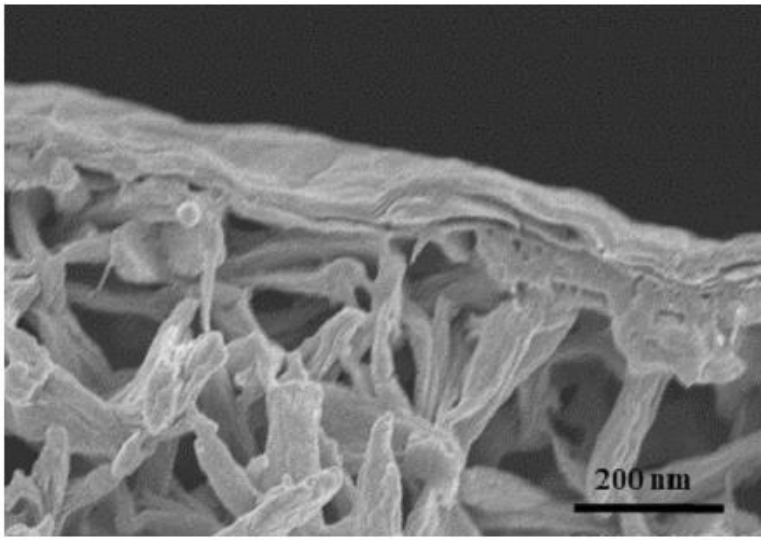

Figure S5. Cross-sectional SEM image of neat GO NFMs. In this case the used GO suspension (0.1 mg/mL) is 4 mL.

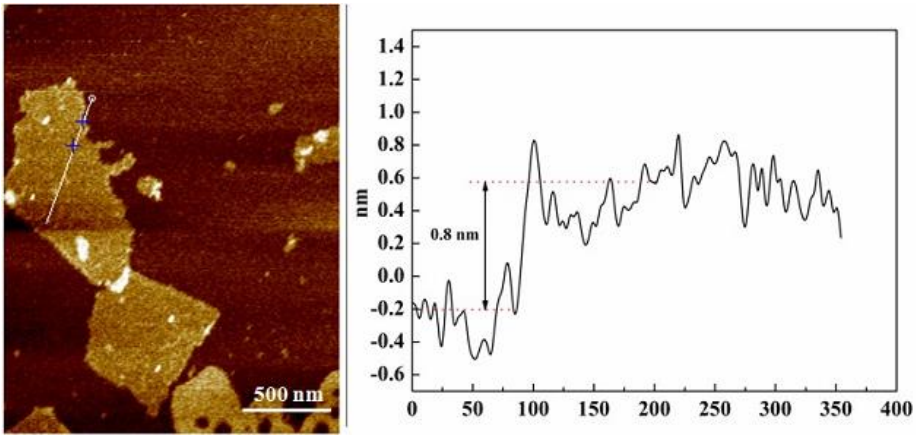

Figure S6. AFM image and corresponding height profile of pure GO. The thickness of GO sheets is about 0.8 nm, implying excellent exfoliation of GO sheets.

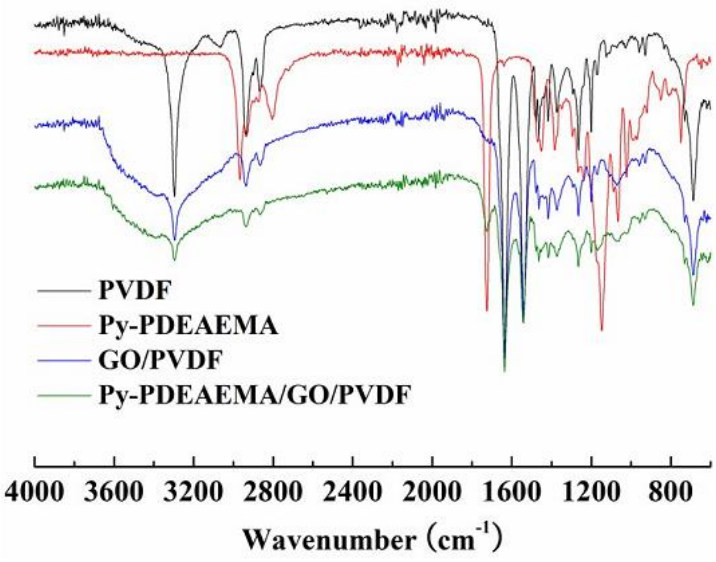

Figure S7. FTIR spectra of PVDF, Py-PDEAEMA, GO/PVDF and Py-PDEAEMA/GO/PVDF. In this case, the molecular weight of Py-PDEAEMA is 13500 g/mol and $R_{P/G}$=6.

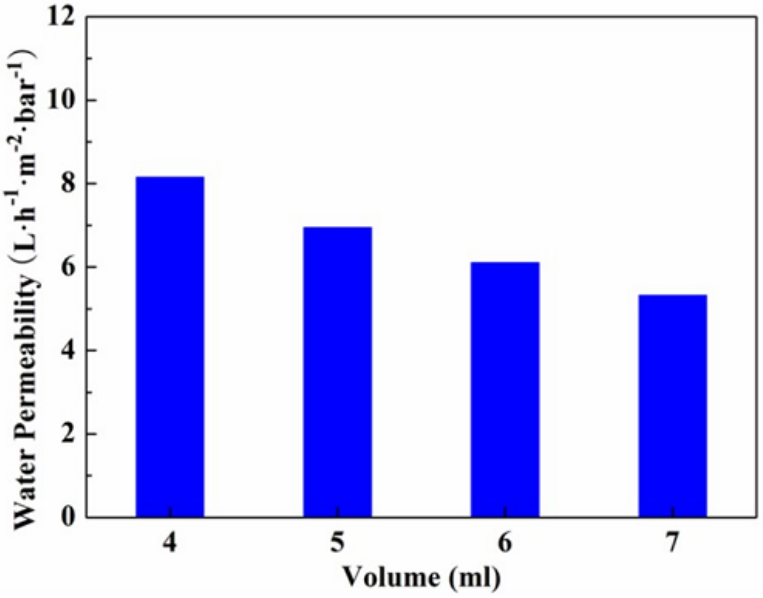

Figure S8. Variation of pure water permeability of GO membrane with different as GO loading under the pressure of 1 bar. When the GO aqueous solution is 8 mL, the water permeability is reduced to none.

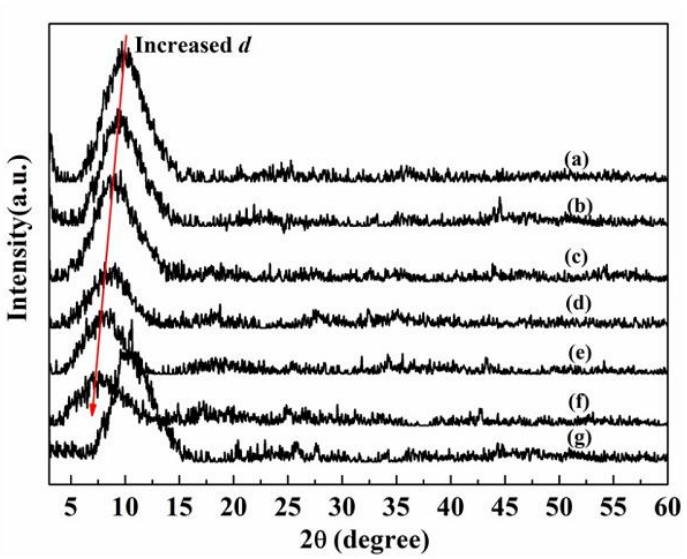

Figure S9. XRD patterns of GO-based membranes: (a) **membrane-3** with $R_{P/G}$=3, (b) **membrane-3**with $R_{P/G}$=4, (c) **membrane-3** with $R_{P/G}$=5, (d) **membrane-1** with $R_{P/G}$=6 and (e) **membrane-2** with $R_{P/G}$=6, and (f) **membrane-3** with $R_{P/G}$=6. (g) Pure GO membrane for comparison.

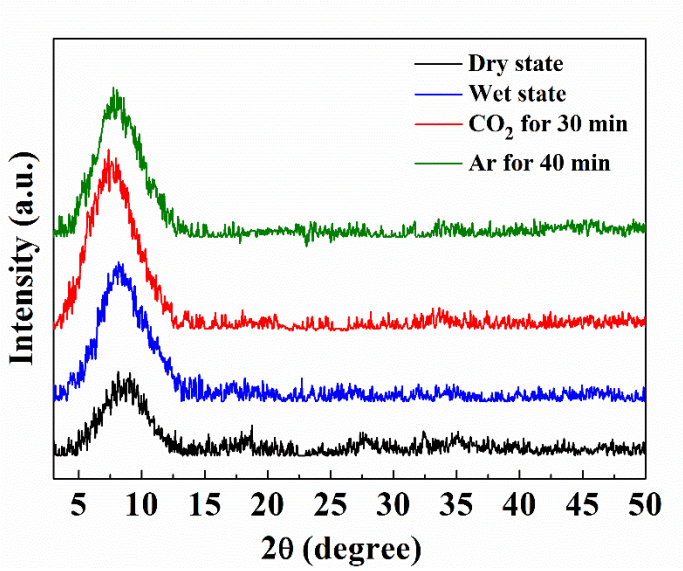

Figure S10. XRD patterns of the **membrane-3** with $R_{P/G}$=6 at the different states.

Figure S10 shows the XRD patterns of **membrane-3** with $R_{P/G}$ = 6 at the different states. The membrane was first pre-immersed in deionized water for 1 h before collecting XRD data from the wet state. Then this membrane was treated with CO_2 bubbling into solution for 30 min, and subsequently with Ar bubbling for 40 min for collecting XRD patterns from these two states. According to the Bragg equation, the *d*-spacing of the membrane at the different states was calculated and reported in Table S2. The interlayer spacings of **membrane-3** increased from 0.98 nm at the dry state to 1.07 nm at the wet state, which is due to swelling of GO sheets in water. After 30 min of CO_2 bubbling, the interlayer spacing increased to 1.17 nm. This is because passing CO_2 through the solution makes the tertiary amine groups in Py-PDEAEMA protonated, which renders the polymer soluble in water. Consequently, the polymer chains of extended conformation increase the interlayer spacings of GO sheets. The subsequent passing of Ar through the solution removes CO_2 and brings Py-PDEAEMA chains back to the insoluble state with collapsed chain conformation, which makes the interlayer spacing return to its original value at the wet state.

Table S2. *d*-Spacing of the **membrane-3** with $R_{P/G}$=6 at the different states.

Membrane	Dry state	Wet state	CO_2 (30 min)	Ar (40 min)
membrane-3 with $R_{P/G}$=6	0.98 nm	1.07 nm	1.17 nm	1.08 nm

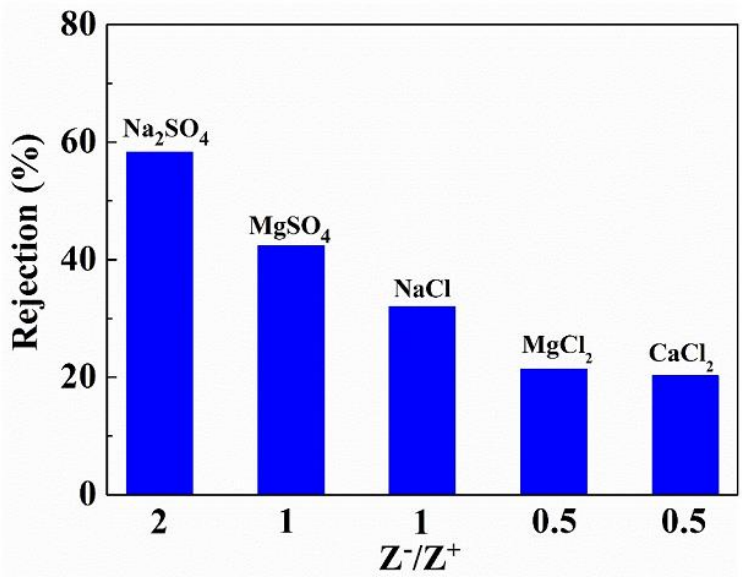

Figure S11. Rejection measured for pure GO membrane for four different salt solutions with different ion valences. In this case the used GO suspension (0.1 mg/mL) is 4 mL.

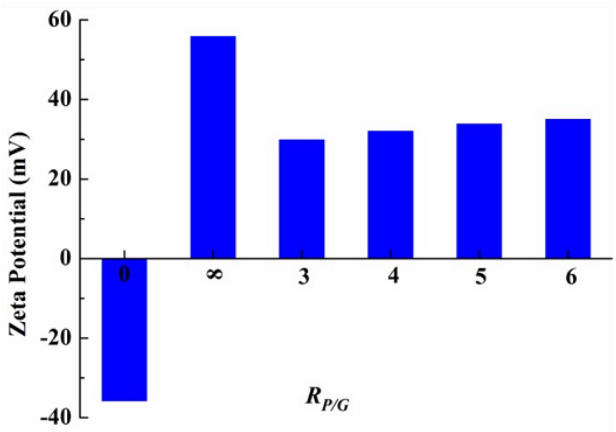

Figure S12. Zeta potential values for Py-PDEAEMA/GO mixtures. Note that $R_{P/G}$= 0 and ∞ represent neat GO and Py-PDEAEMA, respectively. The molecular weight of Py-PDEAEMA

is 13500 g/mol. The pH of Py-PDEAEMA/GO mixtures are 3.7(neat GO), 5.5 (Py-PDEAEMA), 5. ($R_{P/G}$ = 3), 5.4 ($R_{P/G}$ = 4), 5.3 ($R_{P/G}$ = 5) and 5.3 ($R_{P/G}$ = 6).

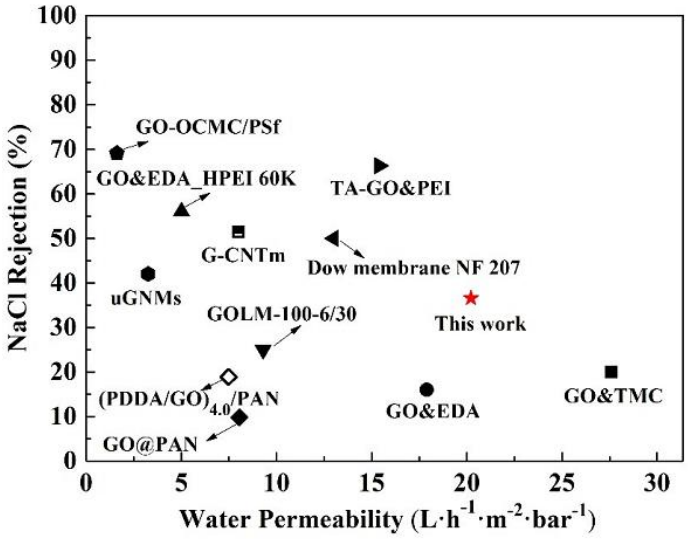

Figure S13. Comparison of pure water permeability and NaCl rejection of **membrane-3** with commercial NFM (NF270)[1] and recently reported GO-based NFMs: GO&EDA and GO&DEA_HPEI 60K,[2] GO@PAN,[3] TA-GO&PEI,[4] GO&TMC,[5] μGNMs,[6] GO-OCMC/psf,[7] GOLM-100-6/30,[8] G-CNTm[9] and $(PDDA/GO)_{4.0}$/PAN membrane[10].

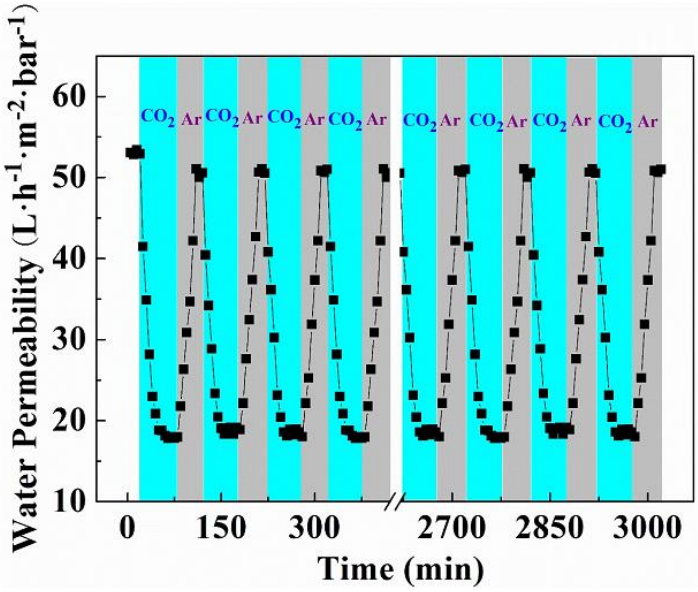

Figure S14. Stability test of gas-switchable permeability of **membrane-3** with $R_{P/G} = 6$.

Reference:

1. B. A. M. Al-Rashdi, D. J. Johnson and N. Hilal, *Desalination*, 2013, **315**, 2.
2. Y. Zhang, S. Zhang and T. S. Chung, *Environ. Sci. Technol.*, 2015, **49**, 10235.
3. J. Q. Wang, P. Zhang, B. Liang, Y. X. Liu, T. Xu, L. F. Wang, B. Cao and K. Pan, *ACS Appl. Mater. Interfaces*, 2016, **8**, 6211.
4. M. Y. Lim, Y. S. Choi, J. Kim, K. Kim, H. Shin, J. J. Kim, D. M. Shin and J. C. Lee, *J. Membr. Sci.*, 2017, **521**, 1.
5. M. Hu and B. X. Mi, Environ. *Sci. Technol.*, 2013, **47**, 3715.
6. Y. Han, Z. Xu and C. Gao, *Adv. Funct. Mater.*, 2013, **23**, 3693.
7. J. L. Wang, X. L. Gao, J. Wang, Y. Wei, Z. K. Li and C. J. Gao, *ACS Appl. Mater. Interfaces*, 2015, **7**, 4381.
8. X. L. Xu, F. W. Lin, Y. Du, X. Zhang, J. Wu and Z. K. Xu, *ACS Appl. Mater. Interfaces*, 2016, **8**, 12588.
9. Y. Han, Y. Q. Jiang and C. Gao, *ACS Appl. Mater. Interfaces*, 2015, **7**, 8147.
10. L. Wang, N. X. Wang, J. Li, J. W. Li, W. Q. Bian and S. L. Ji, *Sep. Purif. Technol.*, 2016, **160**, 123.

2.3. Summary of the Project

In this work, we have successfully combined the CO_2-responsive polymer with GO-based NFMs. The presence of CO_2-responsive polymer, Py-PDEAEMA, rendered NFM with gas responsive behavior, such as gas-tunable water permeability. Even at the pore-closure state caused by swelling polymer chain conformation under CO_2 stimulation, such novel NFM also has higher water permeability than that of pure GO NFM. We found that the nearly complete rejection of the organic dyes (>96%) is preserved with the Py-PDEAEMA/GO NFM even at the full pore opening state with water permeability several times higher than that of the pure GO membrane. More interestingly, different from a negatively charged pure GO NFM, bubbling CO_2 into the solution renders the Py-PDEAEMA/GO NFM positively charged, which leads to a high rejection rate of $MgCl_2$ (48%) as well as excellent water permeability (53.6 L m^{-2} h^{-1} bar^{-1}). Moreover, using multiple strong non-covalent interactions to assemble stimuli-responsive membrane is a promising approach to realizing adaptive materials. Compared with covalent bonding, non-covalent interactions endow membrane fabrication with simpler reaction, more flexible control of chemistry, less usage of organic solvent, and reduction of by-products. Our Py-PDEAEMA/GO NFM perfectly integrates the merits of both CO_2-responsive polymer and GO-based NFMs, opening a door for the next generation of NFMs.

CHAPITRE 3. NEAR-INFRARED LIGHT-DRIVEN LOCOMOTION OF A LIQUID CRYSTAL POLYMER TRILAYER ACTUATOR

3.1. About the Project

Near-infrared (NIR) light induced photothermal effect has been an effective method for the actuation of photo-responsive liquid crystal polymer networks (LCNs). Various photothermal agents have been incorporated into LCN matrices for this purpose, such as carbon nanotubes (CNTs), gold nanorods (AuNR) and graphene oxide (GO). They can transform optical energy into heating to induce the LC-to-isotropic phase transition that drives the LCN actuator to deform macroscopically. In some of the above-mentioned LCN actuators, the light-triggered deformation was converted into locomotion. However, to achieve light-driven motions, the photo-deformable LCN actuator was usually used as hinges to build a device, or needs a supporting plastic frame, and the surface on which the actuator moves needs to be treated. Therefore, it is still challenging to fabricate such LCN actuators that a free piece can perform light-driven caterpillar-type motion on untreated surfaces. In the present work, we design a light-guided trilayer actuator consisted of a thin RGO top layer, an inactive polymer middle layer and an active LCN bottom layer, which can form a light-guided moving wave along the strip. Based on this moving wave, the actuator strip can act as an effective caterpillar-type walker to achieve locomotion on both at-level or inclined surface by scanning NIR laser on it. Our NIR light-driven actuator has the attributes of easy fabrication and capability of locomotion on untreated surface, which may be exploited for applications. To our knowledge, this is the first LCN-based actuator design with graphene paper (RGO or GO) directly deposited on polymer to harness the photothermal effect for light-guided locomotion.

This work was published in *Materials Chemistry Frontiers*, **2018**, 2, 1383 by Liangliang Dong, Xia Tong, Hongji Zhang, Mingqing Chen and Yue Zhao. This research work was accomplished in the Université de Sherbrooke under the supervision of Prof. Zhao and co-supervision of Prof.

Chen. I fabricated the liquid crystal polymer networks (LCNs), reduced graphene oxide (RGO) and all trilayer actuators samples. Xia Tong assisted me with isostrain measurements. I performed all other experiments reported in the paper. Hongji Zhang gave me some useful advice about this project. I wrote the first draft of the manuscript. Prof. Zhao revised and finalized the manuscript.

3.2 Paper Published in Materials Chemistry Frontiers, 2018, 2, 1383.

Near-Infrared Light-Driven Locomotion of a Liquid Crystal Polymer Tri-layer Actuator

Liangliang Dong,[a,b] Xia Tong,[a] Hongji Zhang,[b] Mingqing Chen*[b] and Yue Zhao *[a]

[a]Département de chimie, Université de Sherbrooke, Sherbrooke, QC, J1K 2R1, Canada. E-mail: yue.zhao@usherbrooke.ca

[b]Key Laboratory of Synthetic and Biological Colloids, Ministry of Education, School of Chemical and Material Engineering, Jiangnan University, 1800 Lihu Road, Wuxi 214122, P. R. China. E-mail: mqchen@jiangnan.edu.cn

3.2.1. Abstract

A new and general design is demonstrated for liquid crystal polymer network (LCN)-based actuator to perform near-infrared (NIR) light-guided locomotion. The actuator is a structured trilayer, comprising a thin reduced graphene oxide (RGO) top layer, an inactive polymer middle layer and an active LCN bottom layer. Exposing the RGO side to a moving NIR laser, a moving wave along the strip actuator is generated, which makes the strip an effective caterpillar walker whose light-driven locomotion has appealing attributes. On one hand, in contrast to most LCN-based actuators that moves on ratcheted substrate surface or need a supporting plastic frame, the trilayer actuator moves on untreated, either horizontal or inclined surface. On the other hand, while known actuators using photothermal effect are usually prepared by mixing the nanofiller used as NIR light heater with the polymer, which may reduce the reversible deformation degree and raise the compatibility concern, the easy trilayer fabrication method laminates directly a "sheet" of RGO on thick polymer layers, which circumvents the potential problems.

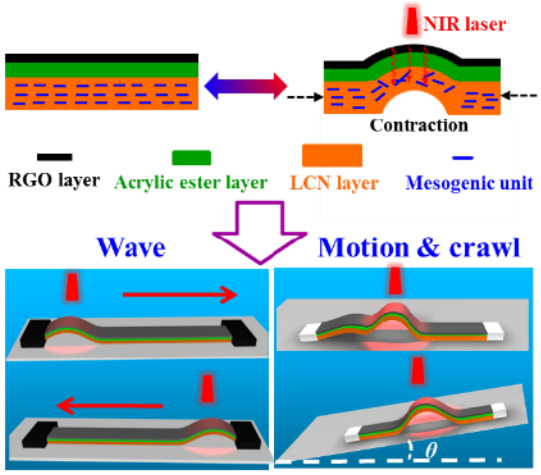

3.2.2. Introduction

In recent years, soft active materials have drawn a great deal of attention because of their envisioned applications in biomedicine,[1, 2] artificial muscles[3, 4] and soft robots.[5-8] Unlike those rigid materials that need mechanical force to be applied to realize motion or deformation, soft active materials can move or deform under thermal,[9-12] optical[13-16] or electrical stimulation.[17-19] Among them, photo-actuated liquid crystal polymer networks (LCNs, including liquid crystal elastomers) have emerged as a particularly promising materials system. They can transform molecular level movements caused by photon energy absorption into macroscopic mechanical motions.[20-27] A common strategy for designing photo-responsive LCNs is based on using azobenzene mesogens in the polymer whose reversible *trans-cis* photoisomerization generates a significant photomechanical effect.[13, 20-26, 28-31] Besides the *trans-cis* photochemical reaction o azobenzene, near-infrared (NIR) light induced photothermal effect has been the basis of another effective method for the actuation of photo-responsive LCNs related to LC-to-isotropic phase transition. Up to now, various photothermal agents have been incorporated into LCN matrices for this purpose, such as carbon nanotubes (CNTs),[27, 32-37] gold nanorods (AuNR)[38-40] and graphene oxide (GO).[41-43] They can transform optical energy into heating to induce the LC-to-isotropic phase transition that drives the LCN actuator to deform macroscopically. However, due to generally poor compatibility with the organic polymers, the concentrations of added photothermal agents are limited, which can restrain the photothermal effect and weaken the photoactuation speeds of the LCN actuators. Directly incorporating a NIR dye into the polymer structure has been proposed to address this issue.[44] In some of the above-mentioned LCN actuators, the light-triggered deformation was converted into locomotion (caterpillar or inchworm-like walking). Generally speaking, to achieve light-driven motions, the photodeformable LCN actuator was used as hinges to build a device,[27, 45] or needs a supporting plastic frame,[21] and the surface on which the actuator moves needs to be treated.[23, 27, 46, 47] Therefore, it is still challenging to fabricate such LCN actuators that a free piece can perform light-driven caterpillar-type motion on untreated surfaces.

Herein, we describe the design, preparation and investigation of a LCN-based trilayer actuator that can address the challenges. The design is depicted in Figure 1A. The top photothermal thin layer is chosen to be reduced graphene oxide (RGO) considering its highly efficient photothermal conversion and thermal conductivity,[48-50] it is separated from the bottom LCN by an inactive polymer layer. The LCN has uniaxial orientation of mesogens, it contracts along the orientation direction upon LC-to-isotropic phase transition and extends on cooling to the LC phase. If the RGO layer is directly connected to the LCN without the middle polymer, when it is exposed to NIR light, the photothermally induced heating on the LCN side in contact with RGO should bend the bilayer towards the light with concave deformation of the RGO layer. While by inserting the middle layer with appropriate thickness and mechanical strength, the RGO-released heat upon NIR light irradiation has to diffuse through the inactive polymer to heat the LCN side for LC-to-isotropic phase transition. With a soft LCN, the contraction should bend the trilayer actuator away from the light with convex deformation for the RGO layer with respect to the incident light. As will be demonstrated further on, the purpose of this design is to use NIR light to generate moving wave along a strip of the actuator with RGO on top to capture the light. This design thus avoids the incorporation of RGO in the LCN matrix.

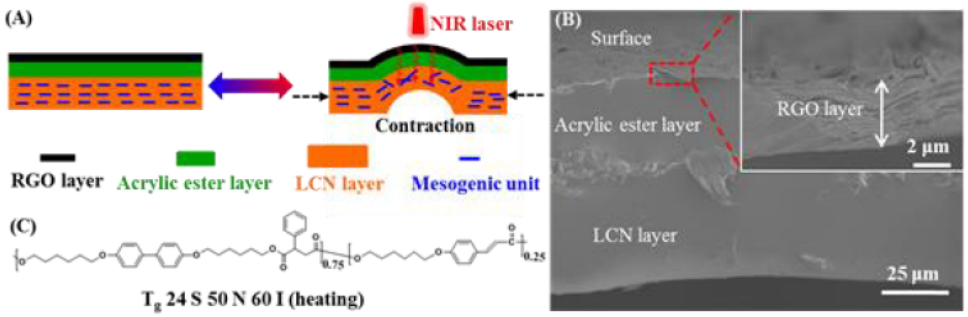

Figure 1. (A) Schematic illustration of the designed near-infrared (NIR) light-responsive trilayer actuator: a thin layer of reduced graphene oxide (RGO) on top, an inactive polymer middle layer and a liquid crystal network (LCN) layer at the bottom. The photothermally induced contraction of the LCN side on contact with the middle layer leads to bending of the actuator

away from the NIR light with convex deformation of the RGO layer surface. (B) Cross-sectional SEM image of a trilayer actuator (the actuator surface is seen due to the imaging angle tilted by 30o). (C) Chemical structure and phase transition temperatures of the used main-chain liquid crystal polymer (Tg, glass transition; S: smectic phase; N: nematic phase; I: isotropic state).

3.2.3. Results and Discussion

The scanning electron microscope (SEM) image in Figure 1B shows the cross-section of a trilayer actuator investigated in this work, the fabrication of which is simple and convenient. The top RGO layer, prepared via vacuum filtration before cutting into a strip shape,[51] has a thickness of about 4 μm, the middle layer, about 30 μm thick, is an acrylic ester tape (double adhesive surfaces)[52] that binds the RGO and the thickest LCN bottom layer (~60 μm) firmly together without delamination. The LCN was prepared using a main-chain liquid crystal polymer (chemical structure in Figure 1C) that was stretched at 55 ºC (in the nematic phase) to 300% elongation to yield monodomain of uniaxial LC orientation, followed by exposure to UV light (320-480 nm filter, 90 mW/cm^2) at 47 ºC on the both sides for uniform photocrosslinking. The obtained LCN actuator displays large reversible contraction/extension (about 51%) along the strain direction upon heating to the isotropic state and cooling to the LC phase, respectively.[11]

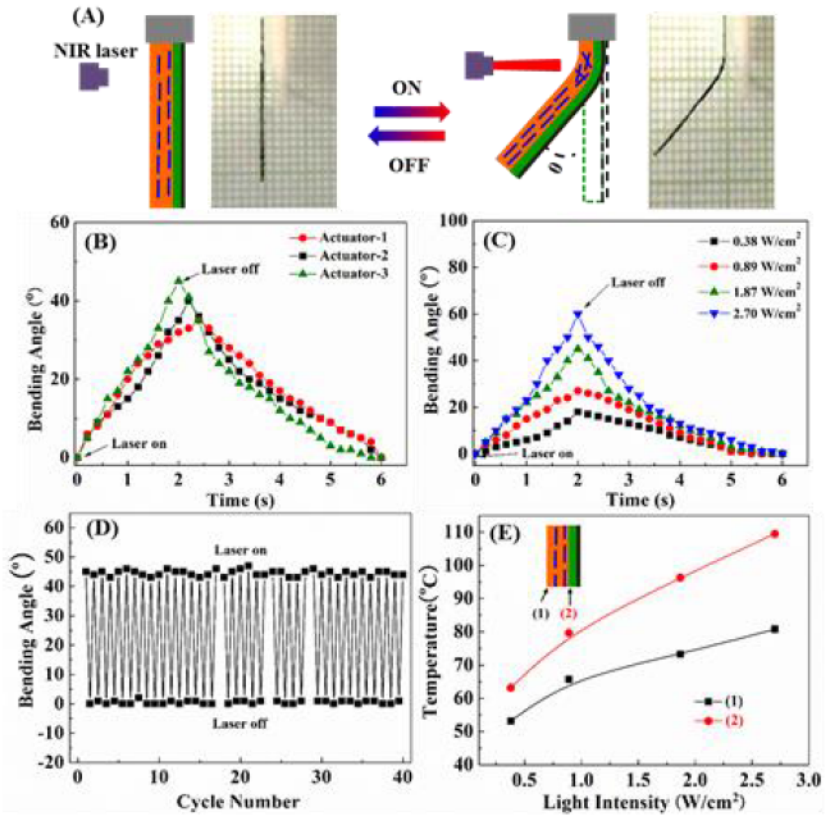

Figure 2. (A) Photos showing the fast bending/unbending of a trilayer strip at NIR light on/off respectively, while the schematic shows the experimental setup and defined bending angle. (B) Change in bending angle over time under NIR light (1.87 W/cm^2) and after NIR turning off for three trilayer actuators with different thicknesses of the LCN layer (about 1, 3 and 4 μm for actuators 1, 2 and 3, respectively). (C) Change in bending angle over time for actuator-3 under NIR light of different intensities and after NIR turning off. (D) Repeated bending angle switch for 40 cycles with actuator-3 subjected to NIR light (1.87 W/cm^2) for 2 seconds and after NIR turning off for 4 seconds. (E) Temperatures measured at the back surface of the LCN layer and at the inactive polymer/LCN interface (inset schematic) after 2 seconds of NIR light irradiation at different intensities, showing NIR light-induced heating of the LCN layer in the trilayer actuator. The dimensions of all actuator strips are 15 mm × 2 mm × 94 μm.

The photoinduced bending behavior of the trilayer actuator was first investigated using an easy setup as depicted in Figure 2A. The specimen was cut into a strip with dimension of 15 mm ×

2 mm × 94 μm, and one end of it was fixed. When NIR light was applied to the upper section of the strip, the photothermally induced LC-to-isotropic phase transition of the LCN can occur and result in deflection of the strip towards the light (due to light exposure from he LCN side). The observed fast bending of an actuator under NIR irradiation for 2 seconds and the subsequent recovery of the straight shape after turning off NIR light for 4 seconds are also shown in Figure 2A. The defined bending angle at NIR light on/off could be measured from the snapshots of the recorded videos (Movie S1). We prepared three trilayer actuators differing only in the thickness of the RGO layer, denoted as actuator-1 (~ 1 μm thick for RGO), actuator-2 (~ 3 μm) and actuator-3 (~ 4 μm) (SEM images in Figure S2). Figure 2B shows the plots of bending angle vs. time under NIR irradiation (980 nm, 1.87 W/cm^2) and after turning off NIR for the three actuators. It appears that with a thicker RGO layer the activation is faster (reaching about 45^o after 1.8 s irradiation for actuator-3), and the relaxation is quicker as well at the NIR off state. This is no surprise because thicker RGO layer means greater photothermal effect that makes a larger portion of LCN undergo the LC-to-isotropic phase transition, resulting in larger photomechanical contraction/extension force for bending/unbending, respectively. Unless otherwise stated, actuator-3 was utilized for other experiments. The effect of NIR light intensity on the photoinduced bending was also investigated. As shown in Figure 2C, with increasing the NIR light intensity, the increasing photothermal effect allowed larger bending angle to be obtained after the same irradiation time of 2 seconds, up to 60^o with the highest intensity tested (2.70 W/cm^2). Figure 2D shows 40 cycles of bending/unbending 2 s after NIR light exposure (1.87 W/cm^2) and 4s after NIR turning off, respectively. Since the durability is important for practical use of an actuator, we tested 500 cycles using actuator-3. The deformation remained almost unchanged and the actuator showed no sign of deterioration in performance (see Figure S4). The fast photoinduced deformation of the trilayer actuator is robust and reliable. The actual NIR light-induced heating of the LCN layer in the actuator was analyzed by measuring the temperatures at the back surface of LCN and the inactive polymer/LCN interface (using RGO/polymer bilayer) using an infrared camera. The temperatures achieved after 2 s NIR irradiation at different light intensities are shown in Figure 2E, indicating clearly the formation

of a temperature gradient across the thickness of the LCN layer, down from the polymer/LCN interface to the back side of the LCN layer. The overall temperature of LCN rises with increasing NIR light intensity, and is effective to induce the LC-to-isotropic phase transition required for the actuation. In control tests using RGO/polymer and polymer/LCN bilayers, no bending actuation was observed under the same NIR light irradiation conditions, further confirming the actuation mechanism of the trilayer actuator.

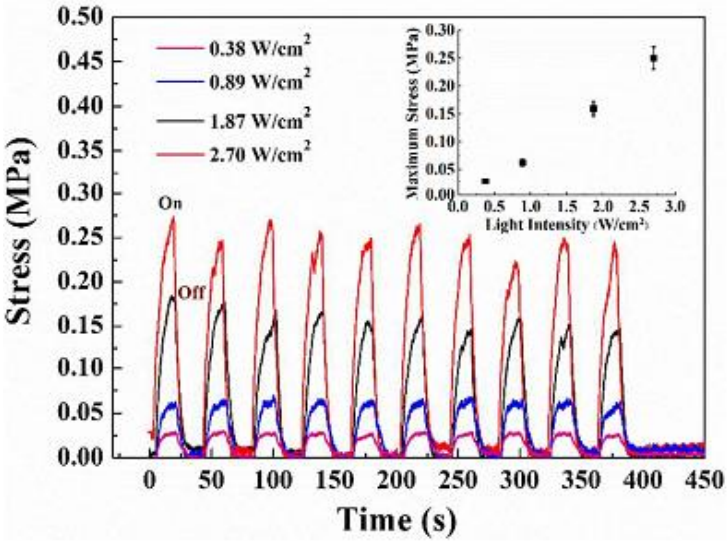

Figure 3. Photothermally induced actuation stress on an actuator-3 strip (15 mm × 2 mm × 94 μm) subjected to a number of cycles of on (15 s)-off (25 s) of 980 nm laser exposure of various intensities. The inset is a plot of maximum stress at laser on state vs. laser intensity.

As described above, the bending behavior of the trilayer actuator under NIR light exposure is determined by an unbalanced contraction force across the thickness direction as a result of photothermally induced order-to-disorder phase transition in the LCN layer. This photomechanical response can be monitored by means of the isostrain testing method by applying NIR light to a strip-shaped sample held under constant strain in the sample holder of a tensile tester (Figure S5). Figure 3 shows the contractile force generated by a trilayer actuator (15 mm × 2 mm × 94 μm) under 980 nm laser irradiation of different intensities. In all cases, when the laser is applied, a contractile force is generated quickly; and it basically drops to zero once the laser

is turned off. It is visible that the actuation stress becomes larger with increasing the 980 nm laser intensity: reaching about 0.025, 0.06, 0.18 and 0.27 MPa for the light intensity of 0.38, 0.89, 1.87 and 2.70 W/cm^2, respectively. The cycle of force up and down under NIR light on and off can be repeated for many times; however, at relatively high laser intensities, the achievable force decreases slightly over time.

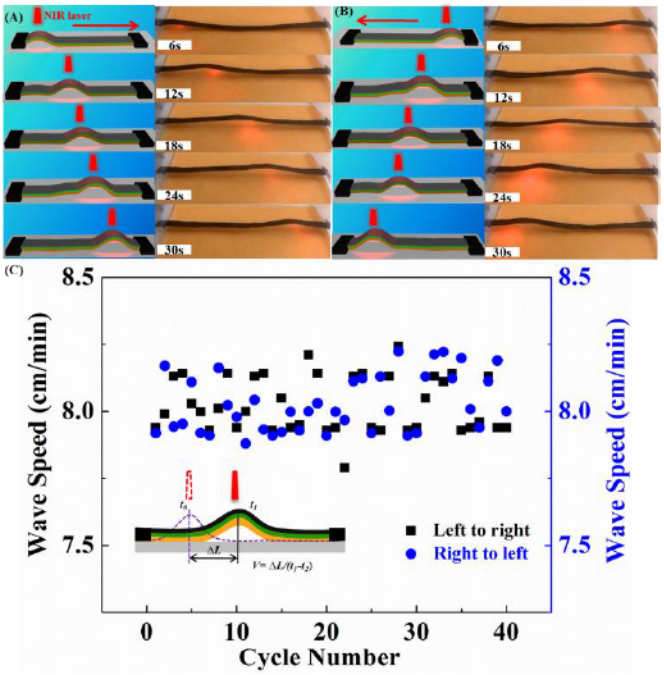

Figure 4. (A, B) Photos and schematics showing NIR light-guided wave propagation along a strip of the actuator whose two ends are fixed to the substrate: (A) moving forward (from left to right) and (B) moving backward (from right to left). (C) Wave moving speed (defined in the schematic) in the two directions obtained for 40 cycles of movement. NIR laser intensity: 1.87 W/cm^2, dimension of the actuator strip: 40 mm × 2 mm × 94 μm.

The fast NIR light triggered actuation was used to generate moving wave along a strip of the trilayer actuator. In this case, the used strip has a large aspect ratio of 20 (dimension: 40 mm × 2 mm × 94 μm) to facilitate the observation. The two ends of the strip were fixed to the substrate (a fluorescent plate for viewing the NIR laser spot), at a separation distance of 35 mm. As shown in Figure 4 by snapshots and illustrations, when the NIR laser is applied to the RGO top

layer, the photothermally induced deformation generates a bump towards the light beam, and when the laser moves along the actuator surface, the bump follows. Guided by the laser movement, this wave can propagate from left to right (Figure 4A, Movie S2) or in the reversed direction (Figure 4B, Movie S2). This light-driven wave motion is robust. Within experimental uncertainty, the wave moving speeds in the two directions remain the same and constant (about 1.3 mm/s) over 40 cycles of "going forward and backward", indicating excellent NIR light-controlled mobility of our trilayer actuator (Figure 4C).

Polymer-based actuators or devices capable of caterpillar-like locomotion under stimulation have attracted much interest in recent years.[21, 23, 27, 45, 46, 53-62] The various types of materials reported in the literature include chemically responsive polymer gel,[55] UV/visible light-activated LCN/polyethylene laminated bilayer,[45] humidity-responsive LCN film,[60] NIR light-responsive devices using CNT-LCN/silicone bilayer,[27] thermally activated poly(ethylene-co-vinyl acetate) (EVA) semicrystalline polymer,[60] and electro-responsive graphene/polydiacetylene (PDA) film.[57] Here, we show that the fast and reversible NIR light-driven wave propagation of our trilayer actuator can be harnessed to fabricate effective caterpillar walker on a smooth surface, using a free actuator strip and without any prior treatment of the substrate surface. Presented in Figure 5 are photos and schematic that show how the light-driven caterpillar locomotion works for a strip placed on the fluorescence plate. At the beginning, the laser spot is applied to the left side of the strip, causing it to arch up and forcing the left edge to bend inward. As the laser spot moves to right, the let part tends to recover to its original flat state. While the left edge experiences a larger frictional force against its motion to left, the right part of the strip, where the laser spot moves to, arches up that flattens the left section with the left edge acting as a stationary point. By repeating the laser movement from left to wright, the propagating wave drives the strip to move toward the right direction. The NIR light-driven moving speed of the caterpillar walker is about 0.1 mm/s (Movie S3), which is similar to what is known with of UV and/or visible light-responsive LCN-base actuators,[23, 45, 53] but much faster than electromechanical LCN (0.05 mm/s)[54] and chemically responsive polymer gel (0.003 mm/s) on a flat

surface.[55]

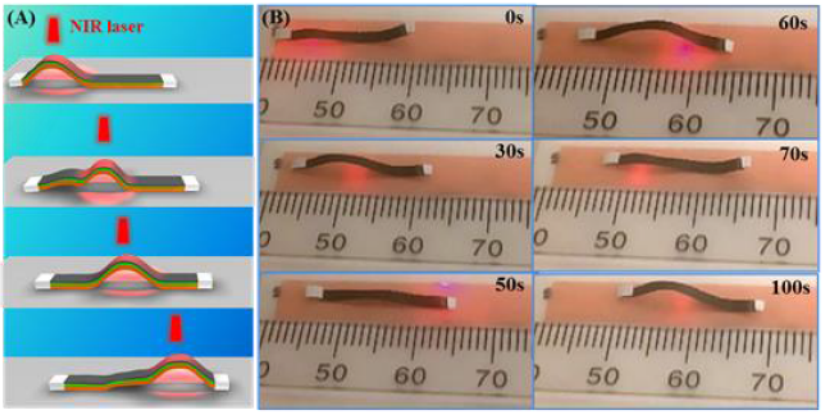

Figure 5. Schematic (A) and photos (B) showing the locomotion of a trilayer strip through propagating wave generated by NIR laser scan from left to right. NIR light intensity: 1.87 W/cm^2, and strip dimension: 20 mm × 2 mm × 94 μm.

More interestingly, our moving-wave walker can also crawl on a smooth slope, which is difficult to achieve without treated surface and hinge-based device. As can be seen in Figure 6, a strip was placed on a piece of fluorescent plate set at a 15° incline. By moving the NIR laser upward along the actuator (1.87 W/cm^2), the strip could climb the incline at an average speed of 0.06 mm/s (Movie S4). Although the incline is relatively small, the result is significant. Indeed, an inchworm-type walker was shown to be able to climb 50° incline under on/off cycles of IR light irradiation, which was a device fabricated with actuating hinges of CNT (SWNT)-loaded LCN/silicone bilayer and the inline surface was ratcheted.[27] Our actuator is very easy to make, just putting the three layers together and cut it into strip shape, and it can crawl up the incline through the moving-wave mechanism with no need to ratchet the incline surface.

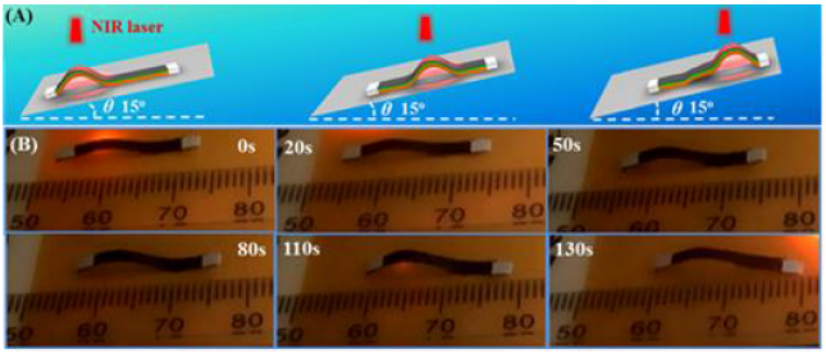

Figure 6. Schematic (A) and photos (B) showing a trilayer strip climbing a 15° incline through moving wave generated by upward NIR laser scan. NIR light intensity: 1.87 W/cm^2, and strip dimension: 20 mm × 2 mm × 94 μm.

3.2.4. Conclusions

We have demonstrated a facile and general approach to fabricating NIR light-driven actuator capable of light-guided locomotion. The trilayer actuator has a thin RGO top layer, an inactive polymer middle layer and a LCN bottom layer, obtained by simply packing them together with the middle layer serving as connection adhesive. By placing a strip of the actuator on a substrate, turning on a NIR laser on the RGO surface and moving it from one side to another can generate a moving wave along the strip, as a result of fast upward bending and downward unbending at laser spot on (photothermally induced heating and LC-to-isotropic phase transition in the bottom LCN layer) and off state (cooling), respectively. We show that this light-driven moving wave makes the actuator strip an effective caterpillar-type walker to undergo locomotion, on both at-level or inclined surface, controlled by directional laser scan on it. Our NIR light-driven actuator has the attributes of easy fabrication and capability of locomotion on untreated surface, which may be exploited for applications. To our knowledge, this is the first LCN-based actuator design with graphene paper (RGO or GO) directly laminated on polymer to harness the photothermal effect for light-guided locomotion.

Conflicts of interest

The authors herein declare no conflicts of interest.

Acknowledgements

Y.Z. acknowledges the financial support from the Natural Sciences and Engineering Research Council of Canada (NSERC) and le Fonds de recherche du Québec: Nature et technologies (FRQNT). L.L.D. thanks China Scholarship Council (CSC) for awarding him a scholarship and the Innovation Project for College Graduates of Jiangsu Province (KYLX16_0783). M.C. thanks the National Natural Science Foundation of China (NNSFC) for financial support (51173072 and 21571084). H. Z. acknowledges the financial support from NNSFC (21504031) and the Natural Science Foundation of Jiangsu Province (BK20150135).

Notes and references

1. H. Yuk, S. Lin, C. Ma, M. Takaffoli, N. X. Fang and X. H. Zhao, *Nat. Commun.*, 2017, **8**, 14230.
2. K. Malachowski, M. Jamal, Q. R. Jin, B. Polat, C. J. Morris and D. H. Gracias, *Nano Lett.*, 2014, **14**, 4164.
3. A. Miriyev, K. Stack and H. Lipson, *Nat. Commun.*, 2017, **8**, 596.
4. S. M. Mirvakili and I. W. Hunter, *Adv. Mater.*, 2017, DOI: 10.1002/adma.201704407.
5. M. Wehner, R. L. Truby, D. J. Fitzgerald, B. Mosadegh, G. M. Whitesides, J. A. Lewis and R. J. Wood, *Nature*, 2016, **536**, 451.
6. H. W. Huang, M. S. Sakar, A. J. Petruska, S. Pané and B. J. Nelson, *Nat. Commun.*, 2016, **7**, 12263.
7. H. Zeng, P. Wasylczyk, D. S. Wiersma and A. Priimagi, *Adv. Mater.*, 2017, DOI: 10.1002/adma.201703554.
8. W. Q. Hu, G. Z. Lum, M. Mastrangeli and M. Sitti, *Nature*, 2018, **554**, 81.
9. K. Yu, Q. Ge and H. J. Qi, *Nat. Commun.*, 2014, **5**, 3066.
10. T. Xie, *Nature*, 2010, **464**, 267.

11. R. Yang and Y. Zhao, *Angew. Chem. Int. Ed.*, 2017, **56**, 14202.
12. V. Stroganov, S. Zakharchenko, E. Sperling, A. K. Meyer, O. G. Schmidt and L. Ionov, *Adv. Funct. Mater.*, 2014, **24**, 4357.
13. J. A. Lv, Y. Y. Liu, J. Wei, E. Q. Chen, L. Qin and Y. L. Yu, *Nature*, 2016, **537**, 179.
14. X. Zhang, Z. Yu, C. Wang, D. Zarrouk, J. W. T. Seo, J. C. Cheng, A. D. Buchan, K. Takei, Y. Zhao, J. W. Ager, J. Zhang, M. Hettick, M. C. Hersam, A. P. Pisano, R. S. Fearing and A. Javey, *Nat. Commun.*, 2014, **5**, 2983.
15. H. W. Zhou, C. G. Xue, P. Weis, Y. Suzuki, S. L. Huang, K. Koynov, G. K. Auernhammer, R. Berger, H. J. Butt and S. Wu, *Nat. Chem.*, 2017, **9**, 145.
16. T. Seki, *J. Mater. Chem. C*, 2016, **4**, 7895.
17. S. Taccola, F. Greco, E. Sinibaldi, A. Mondini, B. Mazzolai and V. Mattoli, *Adv. Mater.*, 2015, **27**, 1668.
18. G. H. Kwon, J. Y. Park, J. Y. Kim, M. L. Frisk, D. J. Beebe and S. H. Lee, *Small*, 2008, **4**, 2148.
19. L. Hines, K. Petersen and M. Sitti, *Adv. Mater.*, 2016, **28**, 3690.
20. A. H. Gelebart, G. Vantomme, E. W. Meijer and D. J. Broer, *Adv. Mater.*, 2017, **29**, 1606712.
21. A. H. Gelebart, D. J. Mulder, M. Varga, A. Konya, G. Vantomme, E. W. Meijer, R. L. B. Selinger and D. J. Broer, *Nature*, 2017, **546**, 632.
22. X. L. Lu, S. W. Guo, X. Tong, H. S. Xia and Y. Zhao, *Adv. Mater.*, 2017, **29**, 1606467.
23. H. Zeng, O. M. Wani, P. Wasylczyk and A. Priimagi, *Macromol. Rapid Commun.*, 2018, **39**, 1700224.
24. M. Yamada, M. Kondo, J. Mamiya, Y. Yu, M. Kinoshita, C. J. Barrett and T. Ikeda, *Angew. Chem. Int. Ed.*, 2008, **47**, 4986.
25. S. Iamsaard, S. J. Aßhoff, B. Matt, T. Kudernac, J. J. L. M. Cornelissen, S. P. Fletcher and N. Katsonis, *Nat. Chem.*, 2014, **6**, 229.
26. H. K. Bisoyi and Q. Li, *Chem. Rev.*, 2016, **116**, 15089.
27. R. R. Kohlmeyer and J. Chen, *Angew. Chem. Int. Ed.*, 2013, **52,** 9234.

28. H. F. Yu and T. Ikeda, *Adv. Mater.*, 2011, **23**, 2149.
29. D. D. Han, Y. L. Zhang, J. N. Ma, Y. Q. Liu, B. Han and H. B. Sun, *Adv. Mater.*, 2016, **28**, 8328.
30. C. Huang, J. Lv, X. Tian, Y. Wang, Y. Yu and J. Liu, *Sci. Rep.*, 2015, **5**, 17414.
31. H. Zeng, O. M. Wani, P. Wasylczyk, R. Kaczmarek and A. Priimagi, *Adv. Mater.*, 2017, DOI: 10.1002/adma.201770215.
32. Y. Yang, Z. Pei, Z. Li, Y. Wei and Y. Ji, *J. Am. Chem. Soc.*, 2016, **138**, 2118.
33. M. Wang, S. M. Sayed, L. X. Guo, B. P. Lin, X. Q. Zhang, Y. Sun and H. Yang, *Macromolecules*, 2016, **49**, 663.
34. J. E. Marshall, Y. Ji, N. Torras, K. Zinoviev and E. M. Terentjev, *Soft Matter*, 2012, **8**, 1570.
35. Y. Ji, Y. Y. Huang, R. Rungsawang and E. M. Terentjev, *Adv. Mater.*, 2010, **22**, 3436.
36. C. S. Li, Y. Liu, X. Z. Huang and H. R. Jiang, *Adv. Funct. Mater.*, 2012, **22**, 5166.
37. L. Q. Yang, K. Setyowati, A. Li, S. Q. Gong, J. Chen, *Adv. Mater.*, 2008, **20**, 2271.
38. X. Y. Liu, R. B. Wei, P. T. Hoang, X. G. Wang, T. Liu and P. Keller, *Adv. Funct. Mater.*, **2015**, **25**, 3022.
39. A. W. Hauser, D. Q. Liu, K. C. Bryson, R. C. Hayward and D. J. Broer, *Macromolecules*, 2016, **49**, 1575.
40. K. G. G. Cuevas, L. Wang, C. M. Xue, G. Singh, S. Kumar, A. Urbas and Q. Li, *Chem. Commun.*, 2015, **51**, 9845.
41. Y. K. Yang, W. J. Zhan, R. G. Peng, C. G. He, X. C. Pang, D. Shi, T. Jiang and Z. Q. Lin, *Adv. Mater.*, 2015, **27**, 6376.
42. R. B. Wei, Z. C. Wang, H. X. Zhang and X. B. Liu, *Liq. Cryst.*, 2016, **43**, 1009.
43. C. S. Li, Y. Liu, X. Z. Huang, C. H. Li and H. R. Jiang, *Mol. Cryst. Liq. Cryst.*, 2015, **616**, 83.
44. L. Liu, M. H. Liu, L. L. Deng, B. P. Lin and H. Yang, *J. Am. Chem. Soc.*, 2017, **139**, 11333.

45. M. Yamada, M. Kondo, R. Miyasato, Y. Naka, J. Mamiya, M. Kinoshita, A. Shishido, Y. L. Yu, C. J. Barrett and T. Ikeda, *J. Mater. Chem.*, 2009, **19**, 60.
46. H. Zeng, P. Wasylczyk, C. Parmeggiani, D. Martella, M. Burresi and D. S. Wiersma, *Adv. Mater.*, 2015, **27**, 3883.
47. X. Y. Liu, S. K. Kim and X. G. Wang, *J. Mater. Chem. B*, 2016, **4**, 7293.
48. Z. X. Cheng, T. J. Wang, X. Li, Y. H. Zhang and H. F. Yu, *ACS Appl. Mater. Interfaces*, 2015, **7**, 27494.
49. T. Wang, J. H. Huang, Y. Q. Yang, E. Z. Zhang, W. X. Sun and Z. Tong, *ACS Appl. Mater. Interfaces*, 2015, **7**, 23423.
50. Y. Yang, Y. Tan, X. L. Wang, W. L. An, S. M. Xu, W. Liao and Y. Z. Wang. *ACS Appl. Mater. Interfaces*, 2018, **10**, 7688.
51. D. Li, M. B. Müller, S. Gilje, R. B. Kaner and G. G. Wallace, *Nat. Nanotechnol.*, 2008, **3**, 101.
52. L. Z. Chen, M. C. Weng, P. D. Zhou, L. L. Zhang, Z. G. Huang and W. Zhang, *Nanoscale*, 2017, **9**, 9825.
53. M. Rogóż, H. Zeng, C. Xuan, D. S. Wiersma and P. Wasylczyk, *Adv. Optical Mater.*, 2016, **4**, 1689.
54. C. Yuan, D. J. Roach, C. K. Dunn, Q. Y. Mu, X. Kuang, C. M. Yakacki, T. J. Wang, K. Yu and H. J. Qi, *Soft Matter*, 2017, **13**, 5558.
55. S. Maeda, Y. Hara, T. Sakai, R. Yoshida and S. Hashimoto, *Adv. Mater.*, 2007, **19**, 3480.
56. Y. Ma, Y. Y. Zhang, B. S. Wu, W. P. Sun, Z. G. Li and J. Q. Sun, *Angew. Chem. Int. Ed.*, 2011, **50**, 6254.
57. J. J. Liang, L. Huang, N. Li, Y. Huang, Y. P. Wu, S. L. Fang, J. Oh, M. Kozlov, Y. F. Ma, F. F. Li, R. Baughman and Y. S. Chen, *ACS Nano*, 2012, **6**, 4508.
58. S. Banisadr and J. Chen, *Sci. Rep.*, 2017, **7**, 17521.
59. M. Y. Ji, N. Jiang, J. Chang and J. Q. Sun, *Adv. Funct. Mater.*, 2014, **24**, 5412.
60. F. J. Ge and Y. Zhao, *Chem. Sci.*, 2017, **8**, 6307.

61. X.B. Zhang, Z.B. Yu, C. Wang, D. Zarrouk, J. W. T. Seo, J. C. Cheng, A. D. Buchan, K. Takei, Y. Zhao, J. W. Ager, J. J. Zhang, M. Hettick, M. C. Hersam, A. P. Pisano, R. S. Fearing and A. Javey, *Nat. Commun.*, 2014, **5**, 2983.
62. S. M. Mirvakili and I. W. Hunter, *Adv. Mater.*, 2017, **29**, 1604734

3.2.5. Supporting Information

3.2.5.1. Materials.

All solvents and reagents were purchased from Sigma Aldrich and used without further purification. Graphene oxide (GO), used to prepare reduced graphene oxide (RGO), was kindly provided by Prof. Hesheng Xia of Sichuan University (produced by The Sixth Element Materials Technology Co., Ltd, China).

3.2.5.2 General Characterizations.

The cross-sectional morphology of trilayer actuators was examined using a Hitachi S-4700 field-emission-gun scanning electron microscope (SEM) operating at 1.0 kV to10.0 kV. For SEM observation, a fine platinum coating layer (a few nm) was laminated on sample surface by using a K550 sputter coater for 1 or 2 min. The bending/unbending angles of the actuators were measured by applying NIR laser (980 nm, normal incidence, light source 10 cm away) to a strip-shaped sample (15 mm × 2 mm × 94 μm). The isostrain measurement for Actuator-3 (experimental setup shown in Figure S4) was performed at room temperature under NIR (785 nm) light irradiation on an Instron 5965 system with a 5 N load cell using the stress-relaxation mode. By applying NIR light (normal incidence, light source 10 cm away) to a stripe-shaped sample held under constant strain (within 0.2 %), the contractile force generated in the film can be sensed and measured. The photothermally induced heating was monitored by measuring the temperature of the actuator using a thermal imager (Tseto 875i) with a temperature resolution of 0.1 °C. While applying the laser on the graphene top layer, the temperature on the other side (either RGO/polymer/LCN trilayer or RGO/polymer bilayer) was recorded. The NIR light intensity was measured using a photometer (Oriel® Instruments).

3.2.5.3. Preparation of RGO Layer.

RGO was prepared according to a literature method.[1] In a typical procedure, the GO was firstly

dispersed in water to create a 0.1 wt% dispersion by ultrasonication for 2 h. Then the resulting homogeneous dispersion was reduced with a hydrazine solution in a 95 ºC oil bath for 1 h. The weight ratio of hydrazine to GO was about 7:10. RGO layers with different thicknesses were prepared by vacuum filtration of different volumes of RGO dispersions through a membrane filter (0.45 μm in pore size), which was followed by drying at room temperature for 6 hours. Finally, the RGO sheet was peeled off from the membrane for further use. In this work, three RGO sheets of varying thickness were obtained by using 5, 6 and 7ml of RGO dispersions, respectively.

3.2.5.4. Preparation of LCN layer and RGO/Acrylic Ester/LCN Trilayer Actuator.

Figure S1 schematically shows the fabrication process of the trilayer actuator. The LCN film was firstly stretched at 55 ºC (nematic phase) to 300% elongation. Then the external force was removed and the two sides of the film were each exposed to UV light (320-480 nm filter, 90 mW/cm^2) for 30 min, reaching essentially uniform crosslinking of the polymer. Trilayer actuator was then assembled by connecting the RGO layer to the stretched LCN through an acrylic ester tape (purchased from Suzhou Tuojia Technology Co., Ltd, China) that becomes the inactive middle polymer layer.

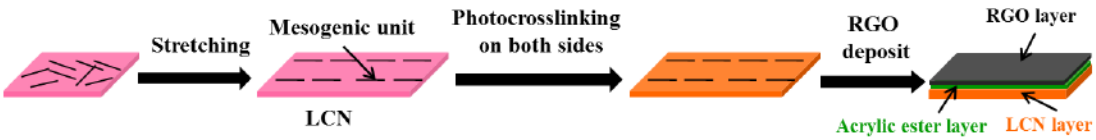

Figure S1. Schematic illustration of the fabrication process of the RGO/Polymer/LCN trilayer actuator.

3.2.5.5. Additional Characterization Results

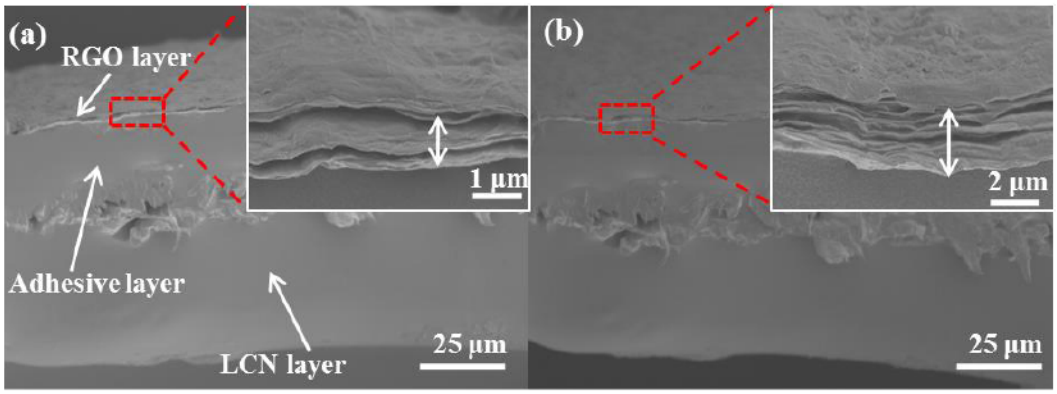

Figure S2. Cross-sectional SEM image of the trilayer actuator-1 (a) and actuator-2, differing in the thickness of the RGO layer.

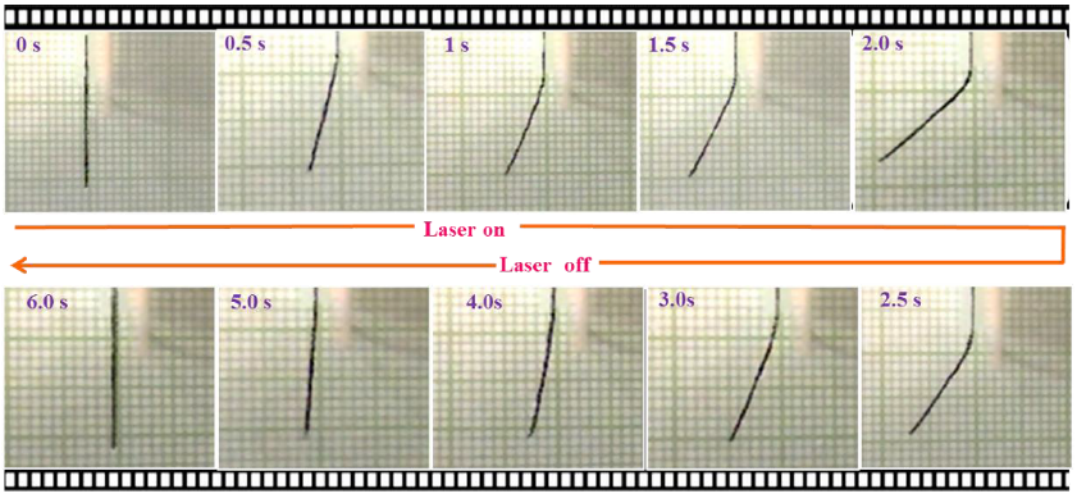

Figure S3. Snapshots showing the reversible bending/unbending of the actuator-3 in response to NIR laser irradiation (1.87 W/cm^2) on/off, respectively.

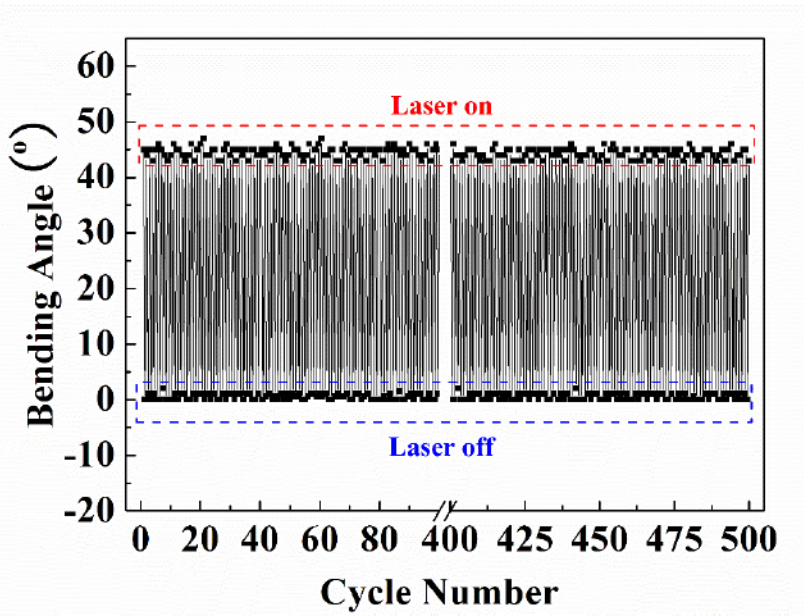

Figure S4. Life cycle of actuator-3 subjected to 500 cycles of NIR light on for 2 seconds (1.87 W/cm^2) and off for 4 seconds

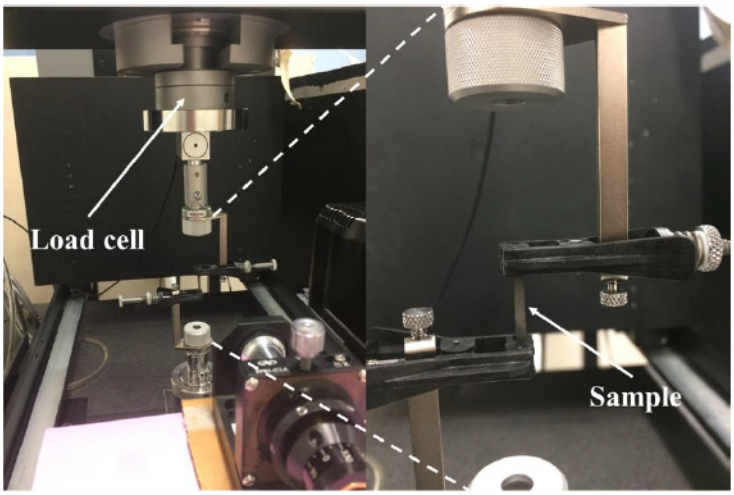

Figure S5. Photograph of the experimental setup used for measuring photoinduced contraction force under the isostrain condition.

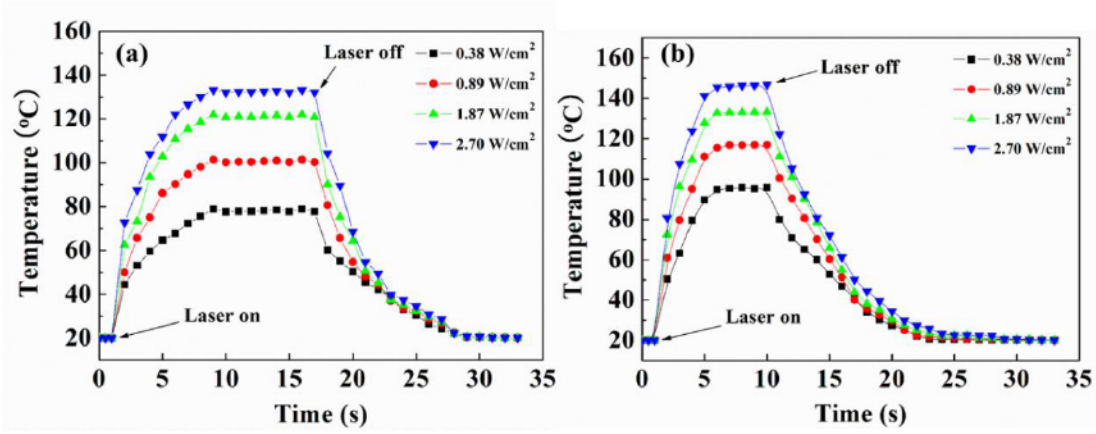

Figure S6. Temperature changes of (a) actuator-3 and (b) RGO/ acrylic ester bilayer as a function of time upon NIR irradiations at different intensities. The NIR laser was applied to the RGO layer and the temperature on the other side of the bilayer or trilayer was measured using an infrared camera. In both cases, the strip was held straight to avoid delamination under prolonged NIR irradiation.

References

1. D. Li, M. Müller, S. Gilje, R. B. Kaner and G. G. Wallace, *Nat. Nanotechnol.*, 2008, **3**, 101.

Supporting Movie Captions

Video S1. Bending/unbending of an actuator in response to NIR laser (1.87 W/cm^2) on/off, respectively

Video S2. NIR light-driven wave propagation under NIR laser (1.87 W/cm^2) scan on a trilayer actuator strip whose two ends were fixed to the substrate.

Video S3. Caterpillar-like locomotion of a free actuator on untreated substrate surface (fluorescent plate) under NIR laser scan (1.87 W/cm^2).

Video S4. Caterpillar-like crawling up of a free actuator on untreated substrate surface (fluorescent plate) set at 15° incline under NIR laser scan (1.87 W/cm^2).

3.3. Summary of the Project

In this project, we design a NIR light-driven trilayer actuator through a facile and general approach. The strip-shape trilayer actuator that contains a thin RGO top layer, an inactive polymer middle layer and a LCN bottom layer, are fabricated by simply packing them together. Under the stimulation of NIR laser, such trilayer actuator shows fast bending/unbending behavior due to excellent photo-thermal conversion efficiency of the RGO layer, as well as unbalanced contraction force across the thickness direction as a result of photothermally induced N-I phase transition in the LCN layer. Based on aforementioned results, a series of versatilely and complicatedly photocontrol motions were achieved. These include NIR light-controlled wave that can can move along with the motion of NIR laser, as well as light-driven, caterpillar walker that can crawl on both at-level or inclined surface by directional laser scan on it, with the speeds of 0.1 mm/s and 0.06 mm/s, respectively. Different from the motion of most LCN-based actuators that need a ratcheted substrate surface or a supporting frame, our trilayer actuator can move on untreated surface. Moreover, the trilayer fabrication method we propose is also an effective strategy to solve the problems that most photothermal responsive actuators usually suffer from, that is, the limited compatibility and decreased reversible deformation degree at high nanofiller loading.

CHAPITRE 4. GENERAL DISCUSSION AND PERSPECTIVES

The research works realized in this thesis are focused on developing novel CO_2-responsive polymer membranes that can realize gas-tunable pore size and gas-controlled size-selective separation, as well as photothermal responsive polymer actuators that have photo-controlled deformations and motions. The research targets are to design new tunable pore structures and controllable motions, study novel stimulation modes and finally build the bridge between these stimuli responsive materials and their applications.

4.1. General Discussion

4.1.1. CO_2-responsive polymer membrane

In the first project, we design a CO_2-responsive polymer membrane that nicely fuses the CO_2-responsive polymers with porous membrane and size separation. Such novel membrane is fabricated by grafting a CO_2-responsive polymer, PDEAEMA, to the PDA functionalized PVDF substrate membrane *via* Michael addition reaction. In this project, PDEAEMA is used as CO_2-responsive functional gates to modulate the pore size of the prepared membranes, due to its reversible change of chain conformation under the stimulation of CO_2/Ar. PDA is used as an interlayer coating for the PVDF porous membrane to allow the further functionalization with PDEAEMA. We used the FTIR/ATR experiments to prove the successful formation of PDEAEMA-PDA@PVDF membranes. The water flux experiments show good gas-responsive behavior of such membrane. Furthermore, we utilize some theoretical calculations to study quantitatively the degree of change of pore sizes under the stimulation of CO_2/Ar. We find that the grafting density of PDEAEMA and CO_2 bubbling time mainly determine the degree of change of pore sizes. The larger the grafting density and longer CO_2 bubbling time, the bigger the degree of change of pore sizes. We also demonstrate that such membrane can successfully achieve the reversible, tunable rejection of AuNP with diameter of 50 nm by simply modulating the CO_2/Ar bubbling time. To our knowledge, this is the first report about the design of CO_2-

responsive polymer membrane with gas-tunable pore sizes for the controlled size separation, which is different from a few reported CO_2-stimulable separation membranes which mainly rely on changes of hydrophilic/hydrophobic properties of the membrane surface for the separation of oil-water mixtures. The unique advantages of this novel membranes include: 1) rapid and reversible changes of pore sizes can be realized by simply passing CO_2 or Ar into solution; 2) CO_2 has a good penetration depth in the presence of water, which allows the responsive behavior inside the membrane to overcome the depth limitation problem often experienced with light- or magnetic field-responsive membranes; 3) while showing excellent switchability, CO_2 as trigger does not contaminate and damage the membrane, which is often experienced by pH- or temperature-responsive membranes.

4.1.2. CO_2-responsive nanofiltration membrane

Although interesting, the membrane reported in the first project can only achieve gas-controlled separation for nanoparticles with a large diameter (>50 nm), which is difficult to be used for separation of organic dyes and salts. The separation of organic dyes and salts is very important to address in the water treatment. Therefore, based on the first project and aimed to solve the above problems, in the second project, we develop a CO_2-responsive nanofiltration membrane for water purification. In this nanofiltration membrane, we not only retain the excellent gas-tunable pore size, but also focus on the gas-induced change of the charge for the tunable separation of organic dyes and salt ions. This "smart" nanofiltration membrane (NFM) can be designed through electrostatic and π-π interactions between the pyrene functionalized PDEAEMA (Py-PDEAEMA) and graphene oxide (GO) under a simple vacuum filtration process. Similar to the results of the first project, the water permeability of such novel NFM can be modulated by alternating the injection of CO_2 and Ar into the solution. Interestingly, even at pore closure state of NFM under stimulation of CO_2, the NFM still has larger water permeability than that of pure GO NFM and commercial NFM. Subsequent rejections experiments of dye molecules show that our designed NFM has high rejections regardless of bubbling CO_2 and Ar, meaning that the membrane can have simultaneously large water permeability and high

rejection of organic dyes, which helps to solve the dilemma of traditional NFM that high water permeability and rejection cannot coexist. More interestingly, upon bubbling CO_2 into the solution, the membrane becomes positively charged, in contrast with negatively charged pure GO membrane, which is suitable for removal of metal ions from the water. Finally, the concept of non-covalent functionalization of GO membrane proposed in this project makes it easy to fabricate CO_2-switchable membranes.

4.1.3. Photothermally-driven liquid crystal polymer actuator

In the third project, we turn our focus to polymer actuators. Polymer actuators can be used for devices that have the ability to give controllable mechanical responses toward external stimuli and then convert those responses into two- or three-dimensional movements and deformations on the nano-, micro-, and macroscales. Polymer actuators have recently attracted growing interest because of their promising applications in artificial muscles, microrobots, lab-on-a-chip systems, and biomimetic devices. Among various polymer actuators, photothermal responsive LCN based actuators have been one of the research hotspots. They can transform photons into heat energy due to the high photothermal effect of the loaded photothermal agents, inducing the LC-to-isotropic phase transition and further driving the whole sample to deform macroscopically. However, the photothermal agents usually have poor compatibility with LCN matrices, leading to a dilemma that decreasing the content of photothermal agents weakens the photoactuation speed of the LCN actuators, but increasing the content would lead to serious phase segregations, impacting negatively the mechanical properties of the LCN actuators. In order to solve this problem, in this project, we develop a NIR light-driven LCN based trilayer actuator. Such trilayer actuator fabricated by packing a thin reduced graphene oxide (RGO) film with an active LCN film with the help of an inactive polymer serving as connection adhesive. We find that our designed trilayer actuator always bend towards the LCN layer regardless of exposing the RGO layer or LCN layer to the NIR laser. This is because photothermally induced contraction always firstly happen on the LCN side in contact with RGO, which results in inhomogeneous contraction of LCN layer due to the presence of RGO layer and adhesive

layer. Based on this inhomogeneous contraction, our trilayer actuator can achieve some NIR light-driven three-dimensional deformations, such as bending/unbending, moving wave and movements. More interestingly, the trilayer actuator is an effective caterpillar-type walker that can walk on both at-level or inclined smooth surface under the guide of NIR laser, compared with motions of most LCN-based actuators that need a ratcheted substrate surface or a supporting plastic frame.

4.2. Future Studies

In view of the enormous application potential of developing CO_2-responsive porous membranes and light-driven polymer actuators, scientists' enthusiasm focused on these two topics will still run high for many years to come. In the light of the knowledge obtained by this thesis, many future works are worth being pursued. Some examples are given below.

4.2.1. CO_2-responsive membrane based on CO_2-responsive polymers-based block copolymers

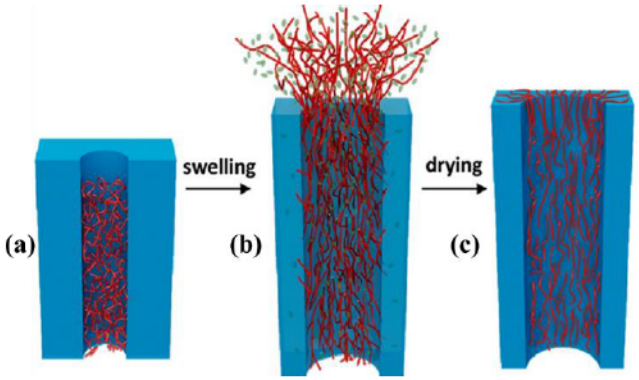

Figure 1. Scheme of the fabrication of homoporous membranes with standing by the selective swelling-induced pore generation. Reproduced from [147] with permission from American Chemical Society.

Generally, the separation performance of a membrane is mainly governed by the sizes and size distribution of pores, porosity, as well as pore geometry. Nowadays, most commercial porous membranes have a tortuous and irregular pore structure, leading to wide size distribution of

pores and crooked pore profile. Such ill-defined pore structure can weaken the separation performance of the membranes (143). As discussed in Introduction, almost all reported stimuli-responsive porous membranes are created by using the stimuli-responsive polymers to modify commercial porous membranes, which means that they inevitably suffer from the same limitation. Recently, Wang *et al.* developed a series of block copolymer (BCP)-based homoporous membranes through selective swelling-induced pore generation (144-148). The mechanism of pore formation is shown in Figure 1. BCP (e.g. PS-*b*-P2VP or PS-*b*-P4VP) solution is firstly deposited on the surface of a support membrane (e.g. PVDF membranes), followed by drying to form BCP nonporous membrane. Then, the BCP nonporous membrane is immersed into a solvent that can selectively swell the minority blocks for hours. Finally, after drying in air, well-defined pores are formed throughout the BCP membrane (147). These membranes possess monodispersed pore sizes, high porosities and straight pore profile, showing high selectivity and permeability. Moreover, by choosing different kinds of BCP or incorporating additives into BCP, various highly ordered and aligned morphologies can be obtained, which endowing the prepared homoporous membrane with different pore structures, such as "standing" and "sleeping" nanopores (Figure 2). Also, this strategy does not destroy the structures of membranes since the minor soft blocks are not dissolved away but transfer to line along the pore walls, thus rendering additional functionalities such as responses to stimuli of the obtained pores (144, 147).

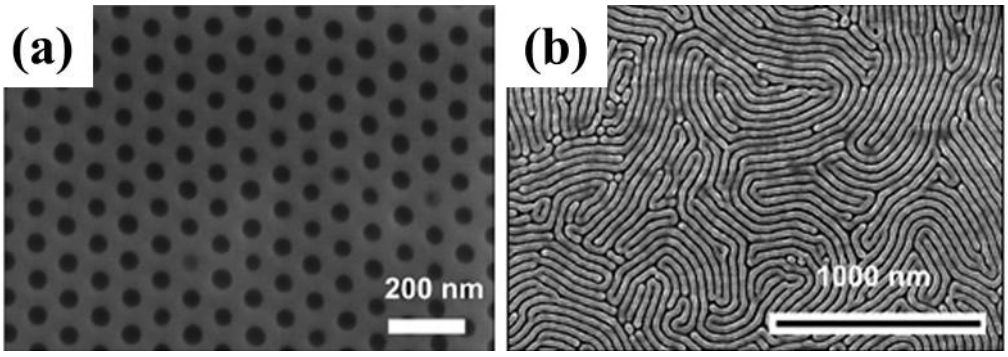

Figure 2. Standing (a) and sleeping (b) pores prepared by selective swelling of prealigned PS-

b-PVP films. Adapted from [144] and [147] with permission from The Royal Society of Chemistry and American Chemical Society, respectively.

Inspired by this strategy, we design a PDEAEMA-based BCP to prepare CO_2-responsive homoporous membrane. We expect that this will be a new direction in CO_2-responsive polymer membranes. As illustrated in Scheme 1, we can synthesis a CO_2-responsive BCP, PS-*b*-PDEAEMA and then prepare the homoporous membrane. In this BCP, PS acts as hard blocks that have slight swelling in the solvent (e.g. ethanol) and also enhance the mechanical property of membrane. While the PDEAEMA acts as soft blocks that has good swelling in the ethanol. When immersed in ethanol, PDEAEMA chains will be swollen and gradually transfer outside their initial state while the PS chains remain essentially unchanged and keep the structural stability of the membrane. After drying, the evaporation of ethanol drives the swelling PDEAEMA chains to collapse. However, the swelling PDEAEMA microdomains will be fixed due to the hard PS phase that prevents them from recovering to their initial state. Therefore, pores are generated in these spaces with the collapsed PDEAEMA chains cling along the pore wall. Upon bubbling CO_2 into the solution, the PDEAEMA will extend and close the pore while bubbling Ar can induce the pore opening again. Furthermore, Wang *et al.* reported that by tuning the molecular weights of BCPs or the swelling conditions, the pore sizes show wide change from 10 nm to 50 nm (143). Therefore, based on this property, it can be expected that the proposed CO_2-responsive homoporous membrane will have wider change of pore size, which means that we can tune the pore size by simply controlling the CO_2/Ar bubbling time for the target applications.

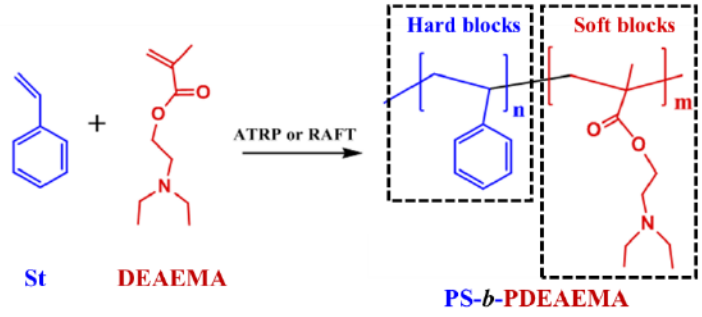

Scheme 1. Synthesis of PS-*b*-PDEAEMA block copolymer for CO_2-responsive homoporous membrane.

4.2.2. CO_2-responsive nanofiltration membrane with gas-switchable charge sign

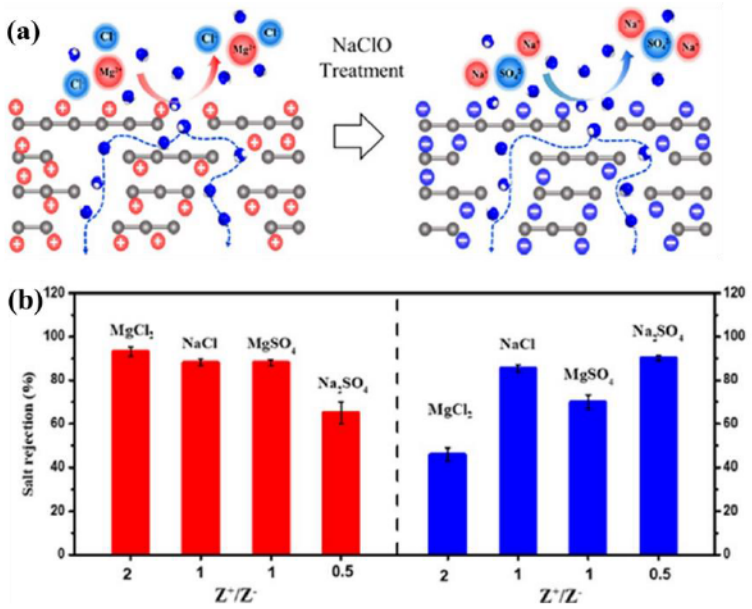

Figure 3. (a) Scheme of mechanism of the tunable charges of PE@ArGO membrane by using NaClO treatments. (b) Rejections of positively (red) and negatively (blue) charged PE@ArGO membranes for salts with different Z^+/Z^- values. Adapted from [149] with permission from American Chemical Society.

As mentioned in Chapter II, NFM as an environment-friendly separation technology has gained increasing attention and widely applied in water softening, wastewater recycling and recovery of pharmaceuticals. Different from the microfiltration (MF) and ultrafiltration (UF) which mainly depend on the steric hindrance effect to achieve the separation of solutes with different molecular sizes, the unique feature of NFM is its electrostatic repulsive effect. For example, the positively charged NFMs usually have high retention of divalent cation (e.g. Mg^{2+} and Ca^{2+}) while the negatively charged NFMs usually have high retention of divalent anion (e.g. SO_4^{2-}). However, since the charges of the all NFMs are usually fixed and unchanged after they are

fabricated, their separation for ions is one direction, which means that none of the NFMs can possess high rejection for all ions. Recently, Tang *et al.* reported a polyelectrolyte (PE) intercalated amine reduced graphene oxide membrane (PE@ArGO membrane) with tunable charges (149). As shown in Figure 3, through in situ NaClO oxidation, the PE@ArGO membrane can change from positive charges to negative charges. Thus, this membrane possesses high rejection for different kinds of ions. But, using the oxidizing agent will damage the integrity of membrane to some extent. Therefore, the challenge remains as to developing NFMs with tunable charges that have simultaneously high rejection for different kinds of ions.

Based on our research in Chapter II, we design a novel CO_2-responsive GO-based NFM with tunable charges. As shown in Scheme 2, we use 2-(dimethylamino)ethyl methacrylate (DMAEMA) instead of DEAEMA to synthesize the pyrene functional PDMAEMA polymer (Py-PDMAEMA) because DMAEMA has good dissolution in water no matter bubbling CO_2 or Ar into solution. This character will always maintain pore of the designed GO-based NFM at closure state, which can avoid the dilemma of NFMs fabricated in Chapter II that bubbling Ar can drive the swelling polymer chains to collapse and then weaken the rejections of ions.

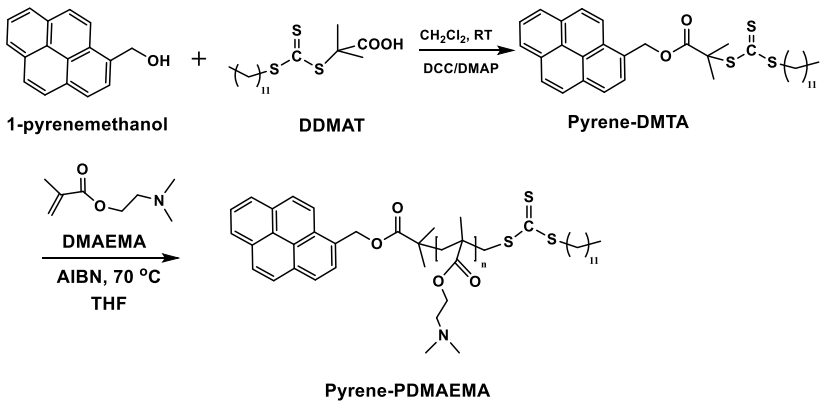

Scheme 2. Synthesis of pyrene-PDMAEMA for CO_2-responsive membrane with gas-switchable charge sign.

As shown in Figure 4, by tuning the ratio of Py-PDMAEMA and GO, we can control the designed NFM at a desired state: originally the NFM has negative charge because of the negative

charge of GO; upon bubbling CO_2 into solution, the Py-PDMAEMA will be protonated and then render the NFM positively charged, which can be used to remove the divalent cation (e.g. Mg^{2+} and Ca^{2+}) from water. Subsequently bubbling Ar or N_2 to remove CO_2, Py-PDMAEMA can be deprotonated and thus the charge of the NFM will recover to its initial state, which can remove the divalent anion (e.g. SO_4^{2-}) from water. Moreover, due to the good hydrophilicity of Py-PDMAEMA, under stimulation of both CO_2 and Ar, our designed Py-PDMAEMA/GO NFM should always possess a good hydrophilicity, which can effectively solve the problem of membrane fouling caused by long and continuous operation. Thus, this novel NFM skillfully fusing the features of negatively charged NFMs and positively charged NFMs will open new direction in NF filed.

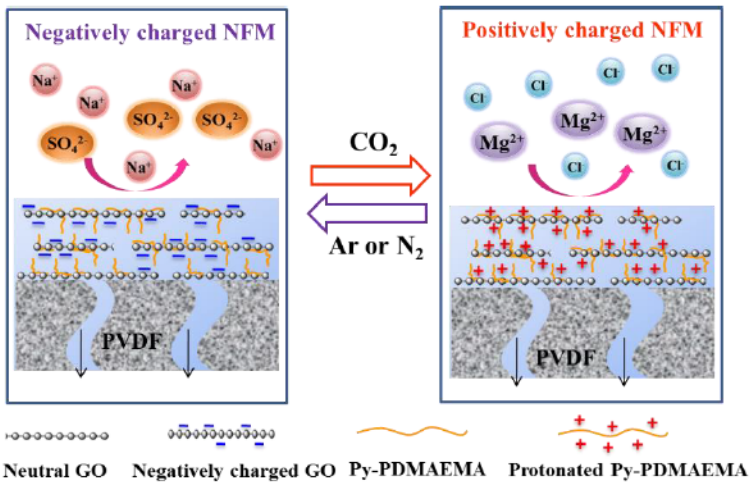

Figure 4. An illustration depicting the reversible change of charge of the CO_2-responsive NFM

4.2.3. Quadruple-responsive polymer actuator

The current developments of stimuli-responsive polymer actuators have gradually evolved from using a single stimulus to multiple stimuli, from simple deformation to complex shape morphing, as well as from using the existing stimuli to seeking for new stimuli. However, the majority of reported polymer actuators only have dual-responsive actuation and still adopt the existing stimuli.

In order to break through this limitation, we design a quadruple-responsive polymer actuator based on LCN and GO composites. As shown in Figure 5, this novel actuator has a bilayer structure with a GO/Py-PDEAEMA layer and LCN layer, which has quadruple-responsive actuation. Firstly, due to the hydration of the C=O and C-O-C groups of LCs in LCN layer (150), the LCN surface can undergo anisotropic swelling when exposing to the moisture, finally causing the humidity-responsive deformation of the whole actuator. Next, because of the presence of the azobenzene chromophores in LCN layer, this bilayer actuator can perform actuation in response to UV and visible light. Additionally, when exposing the GO/Py-PDEAEMA surface to NIR light, the photothermal effect of GO can allow the bilayer actuator to show NIR light-responsive actuation. The last but not least, we introduce the CO_2 response into our bilayer actuator. When the CO_2 saturated with water approaches the GO/Py-PDEAEMA surface, the GO can act as water adsorbent to provide the water environment in which Py-PDEAEMA can react with CO_2 to undergo the transition from hydrophobic to hydrophilic state. This transition will cause the anisotropic swelling of GO/Py-PDEAEMA layer, which leads to deformation of the bilayer actuator. This novel actuator combines the advantages of both the LCN actuators mainly depending on phase transition and GO-based actuators mainly depending on anisotropic swelling, which will pave a new way for fabricating new generation of smart actuators.

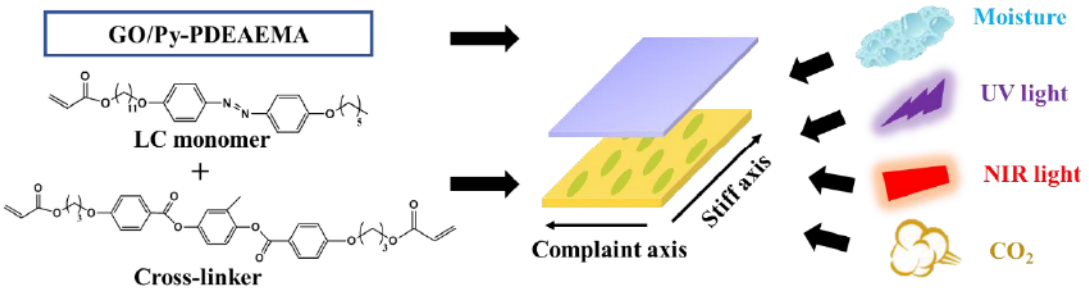

Figure 5. Scheme of fabrication of the quadruple-responsive bilayer actuator based on LCN and Py-PDEAEMA composites.

CONCLUSIONS

The research works presented in this thesis are centered on the design and investigation of the CO_2-responsive porous membranes using CO_2-responsive polymers that achieve the gas-tunable pore size and gas-controlled rejection of salts and photothermal responsive LCN-based actuator that realize the complex deformation under the stimulation of NIR light, such as wave propagation and caterpillar type locomotion. These original research results have led to the publication of three papers in top materials chemistry journals.

In the first work of this thesis, we convincingly introduced the CO_2-responsive polymers into membrane for separation and developed a novel CO_2-responsive polymer membrane with gas-tunable pore size. We found that by alternatively bubbling CO_2 and Ar into water, the prepared CO_2-responsive polymer membrane can effectively have the pores close and open, respectively, as a result of reversible collapse and extension of the CO_2-responsive polymer chains. This control by using gases makes the polymer membrane very useful for size-selective separation or acting as a valve for on-demand passage of species of appropriate sizes. In the carried out study, we demonstrated that the reversible rejection of AuNP with diameter of 50 nm can be successfully realized by using the designed membrane. Moreover, another unique advantage of CO_2-responsive polymer membrane is that the use of the gaseous trigger is not only robust, environmentally friendly and cost-effective, but also solves the problems that pH-, light- or redox-responsive membranes often suffer from. This work develops a new direction of the application of CO_2-responsive polymers and also shows the potential applications in microfluidic systems and biomedical fields where tunable mass separation is required.

The second work of this thesis aimed to go one step further by developing a CO_2-responsive GO-based NFM for the water purification. We demonstrated that the use of a CO_2-responsive polymer in the NFM can significantly increase the space between GO layers to enhance the water permeability with no detrimental effect on the rejection of dye molecules. Also, the gas can convert the CO_2-responsive GO-based NFM from a negatively charged to a positively

charged state, which endows this NFM with high rejection of $MgCl_2$. Moreover, we proposed a novel yet versatile method based on the multiple strong non-covalent interactions for fabrication of CO_2 responsive GO-based NFM. This method has some distinct advantages of simple reaction, flexible control of chemistry, little usage of organic solvent, and reduction of by-products. This work nicely combines the merits of CO_2-responsive polymers and GO-based NFMs, which opens a door for the development of smart stimuli-responsive NFMs.

The last work of this thesis was focused on another important application of stimuli-responsive polymers - polymer actuators. In this study, we fabricated a NIR light-driven trilayer actuator consisting of a thin RGO top layer, an inactive polymer middle layer and a LCN bottom layer. We demonstrated that under the stimulation of NIR laser, such trilayer actuator shows fast bending/unbending behavior due to the photo-thermal conversion efficiency of the RGO layer and the unbalanced contraction force across the thickness direction as a result of photothermally induced LC-isotropic phase transition in the LCN layer. A variety of photothermally driven motions were also achieved, including light-guided wave propagation and caterpillar walker that can crawl on untreated, either horizontal or inclined surface. Moreover, since most of photothermal responsive actuators are usually fabricated by mixing the nanofiller as NIR light heater with the polymer, which may lead to poor compatibility at high nanofiller loading and then declined actuation performance. The trilayer fabrication method in this work is easy and only needs to laminate directly a thin RGO film on thick polymer layers, which can circumvent the compatibility problem.

In conclusion, we have made significant contributions to the design and application of stimuli-responsive polymers. Our works demonstrate that using gas as trigger to fabricate CO_2-responsive porous membranes is very interesting and attractive due to its significant advantages over other stimuli. Additionally, our proposed concept of light-driven trilayer actuator for the locomotion also contributes to the advancement of knowledge in the emerging polymer actuator field. Further fundamental research for better understanding these stimuli-responsive polymers and exploring their applications are very much needed.

BIBLIOGRAPHIE

1. G. Kocak, C. Tuncer and V. Bütün, *Polym. Chem.*, 2017, **8**, 144.
2. T. Manouras and M. Vamvakaki, *Polym. Chem.*, 2017, **8**, 74.
3. J. F. Quinn, M. R. Whittaker and T. P. Davis, *Polym. Chem.*, 2017, **8**, 97.
4. M. L. Wei, Y. F. Gao, X. Li and M. J. Serpe, *Polym. Chem.*, 2017, **8**, 127.
5. K. Huang, *J. Am. Chem. Soc.*, 2017, **139**, 6422.
6. Z. Y. Wang, X. Cheng, A. J. Qin, H. K. Zhang, J. Z. Sun and B. Z. Tang, *J. Phys. Chem. B*, 2018, **122**, 2165.
7. M. Toma, U. Jonas, A. Mateescu, W. Knoll and J. Dostalek, *J. Phys. Chem. C*, 2013, **117**, 11705.
8. X. Li and M. J. Serpe, *Adv. Funct. Mater.*, 2016, **26**, 3282.
9. Y. Mao, Z. Ding, C. Yuan, S. Ai, M. Isakov, J. Wu, T. Wang, M. L. Dunn and H. J. Qi, *Sci. Rep.*, 2016, **6**, 24761.
10. D. Wandera, S. R. Wickramasinghe and S. M. Husson, *J. Membrane Sci.*, 2010, **357**, 6.
11. K. Dutta and S. De, *J. Mater. Chem. A*, 2017, **5**, 22095.
12. Z. Liu, W. Wang, R. Xie, X. J. Ju and L. Y. Chu, *Chem. Soc. Rev.*, 2016, **45**, 460.
13. M. A. C. Stuart, W. T. S. Huck, J. Genzer, M. Muller, C. Ober, M. Stamm, G. B. Sukhorukov, I. Szleifer, V. V. Tsukruk, M. Urban, F. Winnik, S. Zauscher, I. Luzinov and S. Minko, *Nat. Mater.*, 2010, **9**, 101.
14. T. Meng, R. Xie, Y. C. Chen, C. J. Cheng, P. F. Li, X. J. Ju and L. Y. Chu, *J. Membrane Sci.*, 2010, **349**, 258.
15. D. Menne, F. Pitsch, J. E. Wong, A. Pich and M. Wessling, *Angew. Chem. Int. Ed.*, 2014, **53**, 5706.
16. L. Y. Chu, T. Yamaguchi and S. Nakao, *Adv. Mater.*, 2002, **14**, 386.
17. J. I. Clodt, V. Filiz, S. Rangou, K. Buhr, C. Abetz, D. Hoche, J. Hahn, A. Jung and V. Abetz, *Adv. Funct. Mater.*, 2013, **23**, 731.
18. L. Y. Chu, Y. Li, J. H. Zhu and W. M. Chen, *Angew. Chem. Int. Ed.*, 2005, **44**, 2124.

19. M. Yang, L. Y. Chu, H. D. Wang, R. Xie, H. Song and C. H. Niu, *Adv. Funct. Mater.*, 2008, **18**, 652.
20. B. Yang and W. T. Yang, *J. Membrane Sci.*, 2003, **218**, 247.
21. J. Ran, L. Wu, Z. H. Zhang and T. W. Xu, *Prog. Polym. Sci.*, 2014, **39**, 124.
22. J. P. Deng, L. F. Wang, L. Y. Liu and W. T. Yang, *Prog. Polym. Sci.*, 2009, **34**, 156.
23. Z. Liu, F. Luo, X. J. Ju, R. Xie, Y. M. Sun, W. Wang and L. Y. Chu, *J. Mater. Chem. A*, 2013, **1**, 9659.
24. J. Xue, L. Chen, H. L. Wang, Z. B. Zhang, X. L. Zhu, E. T. Kang and K. G. Neoh, *Langmuir*, 2008, **24**, 14151.
25. T. Luo, S. Lin, R. Xie, X. J. Ju, Z. Liu, W. Wang, C. L. Mou, C. S. Zhao, Q. M. Chen and L. Y. Chu, *J. Membrane Sci.*, 2014, **450**, 162.
26. F. Luo, R. Xie, Z. Liu, X. J. Ju, W. Wang, S. Lin and L. Y. Chu, *Sci. Rep.*, 2015, **5**, 14708.
27. C. Weber, R. Hoogenboomd and U. S. Schubert, *Prog. Polym. Sci.*, 2012, **37**, 686.
28. Z. G. Wang, X. P. Yao and Y. Wang, *J. Mater. Chem.*, 2012, **22**, 20542.
29. J. J. Li, Y. N. Zhou and Z. H. Luo, *ACS Appl. Mater. Interfaces*, 2015, **7**, 19643.
30. S. P. Nunes, A. R. Behzad, B. Hooghan, R. Sougrat, M. Karunakaran, N. Pradeep, U. Vainio and K. V. Peinemann, *ACS Nano*, 2011, **5**, 3516.
31. R. Shevate, M. Karunakaran, M. Kumar and K. V. Peinemann, *J. Membrane Sci.*, 2016, **501**, 161.
32. Y. F. Zhao, P. B. Zhang, J. Sun, C. J. Liu, L. P. Zhu and Y. Y. Xu, *J. Membrane Sci.*, 2016, **510**, 306.
33. X. Zhang, J. K. Zhou, R. Wei, W. F. Zhao, S. D. Sun and C. S. Zhao, *J. Membrane Sci.*, 2017, **535**, 158.
34. L. Y. Chu, Y. Li, J. H. Zhu, H. D. Wang and Y. J. Liang, *J. Control. Release*, 2004, **97**, 43.
35. M. Dübner, M. E. Naoum, N. D. Spencer and C. Padeste, *ACS Omega*, 2017, **2**, 455.
36. S. N. Ramanan, N. Shahkaramipour, T. Tran, L. X. Zhu, S. R. Venna, C. K. Lim, A. Singh, P. N. Prasad and H. Q. Lin, *J. Membrane Sci.*, 2018, **554**, 164.

37. H. Rau, *Angew. Chem. Int. Ed.*, 1973, **12**, 224.

38. G. S. Hartley and R. J. W. Le Fevre, *J. Chem. Soc.*, 1939, **0**, 531.

39. F. P. Nicoletta, D. Cupelli, P. Formoso, G. De Filpo, V. Colella and A. Gugliuzza, *Membranes*, 2012, **2**, 134.

40. T. Kinoshita, M. Sato, A. Takizawa and Y. Tsujita, *Macromolecules*, 1986, **19**, 51.

41. K. Weh, M. Noack, R. Ruhmann, K. Hoffmann, P. Toussaint and J. Caro, *Chem. Eng. Technol.*, 1998, **21**, 408.

42. B. Tylkowski, S. Peris, M. Giamberini, R. G. Valls, J. A. Reina and J. C. Ronda, *Langmuir*, 2010, **26**, 14821.

43. J. Anzai, A. Ueno, H. Sasaki, K. Shimokawa and T. Osa, *Makromol. Chem. Rapid Commun.*, 1983, **4**, 731.

44. Y. S. Park, Y. Ito and Y. Imanishi, *Macromolecules*, 1998, **31**, 2606.

45. D. Chung, Y. Ito and Y. Imanishi, *J. Appl. Polym. Sci.*, 1994, **51**, 2027.

46. A. Nayak, H. W. Liu and G. Belfort, *Angew. Chem. Int. Ed.*, 2006, **45**, 4094.

47. P. Kaner, X. R. Hu, S. W. Thomas and A. Asatekin, *ACS Appl. Mater. Interfaces*, 2017, **9**, 13619.

48. J. R. M. Ramírez, *NPG Asia Mater.*, 2013, **5**, 52.

49. L. Hu, S. J. Gao, X. G. Ding, D. Wang, J. Jiang, J. Jin and L. Jiang, *ACS Nano*, 2015, **9**, 4835.

50. J. C. Liu, N. Wang, L. J. Yu, A. Karton, W. Li, W. X. Zhang, F. Y. Guo, L. L. Hou, Q. F. Cheng, L. Jiang, D. A. Weitz and Y. Zhao, *Nat. Commun.*, 2017, **8**, 2011.

51. Q. H. Ng, J. K. Lim, A. L. Ahmad, B. S. Ooi and S. C. Low, *J. Membrane Sci.*, 2015, **493**, 134.

52. A. M. Gajda and M. Ulbricht, *J. Mater. Chem. B*, 2014, **2**, 1317.

53. X. Lin, R. Huang and M. Ulbricht, *J. Mater. Chem. B*, 2016, **4**, 867.

54. X. Lin, B. N. Quoc and M. Ulbricht, *ACS Appl. Mater. Interfaces*, 2016, **8**, 29001.

55. H. Chen, G. R. Palmese and Y. A. Elabd, *Macromolecules*, 2007, **40**, 781.

56. T. W. Chuo, T. C. Wei, Y. Chang and Y. L. Liu, *ACS Appl. Mater. Interfaces*, 2013, **5**,

9918.

57. H. B. Liu, S. J. Lin, Y. J. Feng and P. Theato, *Polym. Chem.*, 2017, **8**, 12.
58. Q. Zhang, L. Lei and S. P. Zhu, *ACS Macro Lett.*, 2017, **6**, 515.
59. Q. Yan and Y. Zhao, *Chem. Commun.*, 2014, **50**, 11631.
60. D. H. Han, X. Tong, O. Boissière and Y. Zhao, *ACS Macro Lett.*, 2012, **1**, 57.
61. H. L. Che, M. Huo, L. Peng, T. Fang, N. Liu, L. Feng, Y. Wei and J. Y. Yuan, *Angew. Chem. Int. Ed.*, 2015, **54**, 8934.
62. H. Y. Yin, A. L. Bulteau, Y. J. Feng and L. Billon, *Adv. Mater. Interfaces*, 2016, **3**, 1500623.
63. S. J. Lin, J. J. Shang and P. Theato, *ACS Macro Lett.*, 2018, **7**, 431.
64. E. Reyssat and L. Mahadevan, *J. R. Soc., Interface*, 2009, **6**, 951.
65. E. Stokstad, *Science*, 2016, **352**, 756.
66. R. Hanlon, *Curr. Biol.*, 2007, **17**, R400.
67. S. M. Mirvakili and I. W. Hunter, *Adv. Mater.*, 2018, **30**, 1704407.
68. Z. Pei, Y. Yang, Q. Chen, E. M. Terentjev, Y. Wei and Y. Ji, *Nat. Mater.*, 2014, **13**, 36.
69. G. M. Whitesides, *Angew. Chem. Int. Ed.*, 2018, **57**, 2.
70. L. Hines, K. Petersen, G. Z. Lum and M. Sitti, *Adv. Mater.*, 2017, **29**, 1603483.
71. C. J. Wang, K. Sim, J. Chen, H. Kim, Z. Rao, Y. H. Li, W. Q. Chen, J. Z. Song, R. Verduzco and C. J. Yu, *Adv. Mater.*, 2018, **30**, 1706695.
72. W. Q. Hu, G. Z. Lum, M. Mastrangeli and M. Sitti, *Nature*, 2018, **554**, 81.
73. F. Rosso, G. Marino, A. Giordano, M. Barbarisi, D. Parmeggiani and A. Barbarisi, *J. Cell Physiol.*, 2005, **203**, 465.
74. T. H. Ware, M. E. McConney, J. J. Wie, V. P. Tondiglia and T. J. White, *Science*, 2015, **347**, 982.
75. F. J. Ge, X. L. Lu, J. Xiang, X. Tong and Y. Zhao, *Angew. Chem. Int. Ed.*, 2017, **56**, 6126.
76. H. Zeng, P. Wasylczyk, D. S. Wiersma and A. Priimagi, *Adv. Mater.*, 2018, **30**, 1703554.
77. D. D. Han, Y. L. Zhang, J. N. Ma, Y. Q. Liu, B. Han and H. B. Sun, *Adv. Mater.*, 2016, **28**, 8328.

78. L. X. Guo, M. H. Liu, S. M. Sayed, B. P. Lin, P. Keller, X. Q. Zhang, Y. Sun and H. Yang, *Chem. Sci.*, 2016, **7**, 4400.
79. Y. L. Yu, M. Nakano and T. Ikeda, *Nature*, 2003, **425**, 145.
80. H. F. Yu and T. Ikeda, *Adv. Mater.*, 2011, **23**, 2149.
81. J. J. Wie, M. R. Shankar and T. J. White, *Nat. Commun.*, 2016, **7**, 13260.
82. M. Yamada, M. Kondo, J. I. Mamiya, Y. Yu, M. Kinoshita, C. J. Barrett and T. Ikeda, *Angew. Chem. Int. Ed.*, 2008, **47**, 4986.
83. X. L. Lu, S. W. Guo, X. Tong, H. S. Xia and Y. Zhao, *Adv. Mater.*, 2017, **29**, 1606467.
84. C. L. van Oosten, C. W. M. Bastiaansen and D. J. Broer, *Nat. Mater.*, 2009, **8**, 677.
85. Z. X. Cheng, S. D. Ma, Y. H. Zhang, S. Huang, Y. X. Chen and H. F. Yu, *Macromolecules*, 2017, **50**, 8317.
86. M. Yamada, M. Kondo, R. Miyasato, Y. Naka, J. Mamiya, M. Kinoshita, A. Shishido, Y. L. Yu, C. J. Barrett and T. Ikeda, J. Mater. Chem., 2009, **19**, 60.
87. X. L. Lu, H. Zhang, G. X. Fei, B. Yu, X. Tong, H. S. Xia and Y. Zhao, *Adv. Mater.*, 2018, **30**, 1706597.
88. S. Iamsaard, S. J. Aßhoff, B. Matt, T. Kudernac, J. L. M. C. Jeroen, S. P. Fletcher and N. Katsonis, *Nat. Chem.*, 2014, **6**, 229.
89. K. M. Lee and T. J. White, *Polymers*, 2011, **3**, 1447.
90. K. Kumar, C. Knie, D. Bléger, M. A. Peletier, H. Friedrich, S. Hecht, D. J. Broer, M. G. Debije and A. P. H. J. Schenning, *Nat. Commun.*, 2016, **7**, 11975.
91. S. Serak, N. Tabiryan, R. Vergara, T. J. White, R. A. Vaia and T. J. Bunning, *Soft Matter*, 2010, **6**, 779.
92. J. E. Marshall, Y. Ji, N. Torras, K. Zinoviev and E. M. Terentjev, *Soft Matter*, 2012, **8**, 1570.
93. A. A. Beharry, O. Sadovski and G. A. Woolley, *J. Am. Chem. Soc.*, 2011, **133**, 19684.
94. C. Knie, M. Utecht, F. L. Zhao, H. Kulla, S. Kovalenko, A. M. Brouwer, P. Saalfrank, S. Hecht and D. Bléger, *Chem. Eur. J.*, 2014, **20**, 16492.
95. S. M. Guo, X. Liang, C. H. Zhang, M. Chen, C. Shen, L. Y. Zhang, X. Yuan, B. F. He

and H. Yang, *ACS Appl. Mater. Interfaces*, 2017, **9**, 2942.

96. X. Liang, S. M. Guo, M. Chen, C. Y. Li, Q. Wang, C. Zou, C. H. Zhang, L. Y. Zhang, S. J. Guo and H. Yang, *Mater. Horiz.*, 2017, **4**, 878.
97. M. Wang, C. Zou, J. Sun, L. Y. Zhang, L. Wang, J. M. Xiao, F. S. Li, P. Song and H. Yang, *Adv. Funct. Mater.*, 2017, **27**, 1702261.
98. X. Liang, C. S. Guo, M. Chen, S. M. Guo, L. Y. Zhang, F. S. Li, S. J. Guo and H. Yang, *Nanoscale Horiz.*, 2017, **2**, 319.
99. T. J. White and D. J. Broer, *Nat. Mater.*, 2015, **14**, 1087.
100. P. Beyer, E. M. Terentjev and R. Zentel, *Macromol. Rapid Commun.*, 2007, **28**, 1485.
101. N. Torras, K. E. Zinoviev, J. E. Marshall, E. M. Terentjev and J. Esteve, *Appl. Phys. Lett.,* 2011, **99**, 254102.
102. M. Wang, S. M. Sayed, L. X. Guo, B. P. Lin, X. Q. Zhang, Y. Sun and H. Yang, *Macromolecules*, 2016, **49**, 663.
103. L. Q. Yang, K. Setyowati, A. Li, S. Q. Gong and J. Chen, *Adv. Mater.*, 2008, **20**, 2271.
104. C. J. Camargo, H. Campanella, J. E. Marshall, N. Torras, K. Zinoviev, E. M. Terentjev and J. Esteve, *Macromol. Rapid Commun.*, 2011, **32**, 1953.
105. C. J. Camargo, H. Campanella, J. E. Marshall, N. Torras, K. Zinoviev, E. M. Terentjev and J. Esteve, *J. Micromech. Microeng.*, 2012, **22**, 075009.
106. Y. Yang, Z. Q. Pei, Z. Li, Y. Wei and Y. Ji, *J. Am. Chem. Soc.*, 2016, **138**, 2118.
107. Y. Ji, Y. Y. Huang, R. Rungsawang and E. M. Terentjev, *Adv. Mater.*, 2010, **22**, 3436.
108. R. R. Kohlmeyer and J. Chen, *Angew. Chem. Int. Ed.*, 2013, **52**, 9234.
109. C. H. Li, Y. Liu, C.W. Lo and H. R. Jiang, *Soft Matter*, 2011, **7**, 7511.
110. S. V. Ahir, A. M. Squires, A. R. Tajbakhsh and E. M. Terentjev, *Phys. Rev. B*, 2006,**73**, 085420.
111. C. S. Li, Y. Liu, X. Z. Huang and H. R. Jiang, *Adv. Funct. Mater.*, 2012, **22**, 5166.
112. Z. X. Cheng, T. J. Wang, X. Li, Y. H. Zhang and H. F. Yu, *ACS Appl. Mater. Interfaces*, 2015, **7**, 27494.
113. L. Yu, Z. X. Cheng, Z. J. Dong, Y. H. Zhang and H. F. Yu, *J. Mater. Chem. C*, 2014, **2**,

8501.

114. R. B. Wei, Z. C. Wang, H. X. Zhang and X. B. Liu, *Liq. Cryst.*, 2016, **43**, 1009.

115. Y. K. Yang, W. J. Zhan, R. G. Peng, C. G. He, X. C. Pang, D. Shi, T. Jiang and Z. Q. Lin, *Adv. Mater.*, 2015, **27**, 6376.

116. Y. R. Sun, J. S. Evans, T. Lee, B. Senyuk, P. Keller, S. L. He and I. I. Smalyukh, *Appl. Phys. Lett.*, 2012, **100**, 241901.

117. A. W. Hauser, D. Q. Liu, K. C. Bryson, R. C. Hayward and D. J. Broer, *Macromolecules*, 2016, **49**, 1575.

118. K. G. G. Cuevas, L. Wang, C. M. Xue, G. Singh, S. Kumar, A. Urbas and Q. Li, *Chem. Commun.*, 2015, **51**, 9845.

119. X. Y. Liu, R. B. Wei, P. T. Hoang, X. G. Wang, T. Liu and P. Keller, *Adv. Funct. Mater.*, 2015, **25**, 3022.

120. H.Yang, J. J. Liu, Z. F. Wang, L. X. Guo, P. Keller, B. P. Lin, Y. Sun and X. Q. Zhang, *Chem. Commun.*, 2015, **51**, 12126.

121. L. T. Haan, C. S. Somolinos, C. M. W. Bastiaansen, A. P. H. J. Schenning and D. J. Broer, *Angew. Chem. Int. Ed.*, 2012, **51**, 12469.

122. L. T. Haan, V. G. Pinto, A. Konya, T. S. Nguyen, J. M. N. Verjans, C. S. Somolinos, J. V. Selinger, R. L. B. Selinger, D. J. Broer and A. P. H. J. Schenning, *Adv. Funct. Mater.*, 2014, **24**, 1251.

123. A. H. Gelebart, G. Vantomme, E. W. Meijer and D. J. Broer, *Adv. Mater.*, 2017, **29**, 1606712.

124. M. Wang, B. P. Lin and H. Yang, *Nat. Commun.*, 2016, **7**, 13981.

125. L. Liu, M. H. Liu, L. L. Deng, B. P. Lin and H. Yang, *J. Am. Chem. Soc.*, 2017, **139**, 11333.

126. H. Zeng, O. M. Wani, P. Wasylczyk and A. Priimagi, *Macromol. Rapid Commun.*, 2018, **39**, 1700224.

127. M. Rogóż, H. Zeng, C. Xuan, D. S. Wiersma and P. Wasylczyk, *Adv. Optical Mater.*, 2016, **4**, 1689.

128. H. Zeng, P. Wasylczyk, C. Parmeggiani, D. Martella, M. Burresi and D. S. Wiersma, *Adv. Mater.*, 2015, **27**, 3883.

129. F. J. Ge, R. Yang, X. Tong, F. Camerel and Y. Zhao, *Angew. Chem. Int. Ed.*, 2018, **57**, 11758.

130. A. H. Gelebart, D. J. Mulder, G. Vantomme, A. P. H. J. Schenning and D.J.Broer, *Angew. Chem. Int. Ed.*, 2017, **56**, 13436.

131. A. H. Gelebart, D. J. Mulder, M. Varga, A. Konya, G. Vantomme, E. W. Meijer, R. L. B. Selinger and D. J. Broer, *Nature,* 2017, **546**, 632.

132. K. Kumar, C. Knie, D. Bléger, M. A. Peletier, H. Friedrich, S. Hecht, D. J. Broer, M. G. Debije and A. P. H. J. Schenning, Nat. Commun., 2016, **7**, 11975.

133. W. Liu, L. X. Guo, B. P. Lin, X. Q. Zhang, Y. Sun and H. Yang, *Macromolecules*, 2016, **49**, 4023.

134. C. Ohm, M. Brehmer and R. Zentel, *Adv. Mater.*, 2010, **22**, 3366.

135. H. J. Zhang, H. S. Xia and Y. Zhao, *ACS Macro Lett.*, 2014, **3**, 940.

136. Z. Li, Y. Yang, Z. H. Wang, X. Y. Zhang, Q. M. Chen, X. J. Qian, N. Liu, Y. Wei and Y. Ji, *J. Mater. Chem. A*, 2017, **5**, 6740.

137. H. M. Tian, Z. J. Wang, Y. L. Chen, J. Y. Shao, T. Gao and S. Q. Cai, *ACS Appl. Mater. Interfaces*, 2018, **10**, 8307.

138. D. Martella, S. Nocentini, D. Nuzhdin, C. Parmeggiani and D. S. Wiersma, *Adv. Mater.*, 2017, **29**, 1704047.

139. O. M. Wani, H. Zeng and A. Priimagi, *Nat. Commun.*, 2017, 8, 15546.

140. J. J. Wie, M. R. Shankar and T. J. White, *Nat. Commun.*, 2016, **7**, 13260.

141. S. Palagi, A. G. Mark, S. Y. Reigh, K. Melde, T. Qiu, H. Zeng, C. Parmeggiani, D. Martella, A. S. Castillo, N. Kapernaum, F. Giesselmann, D. S. Wiersma, E. Lauga and P. Fischer, *Nat. Mater.*, 2016, **15**, 647.

142. K. M. Lee, M. L. Smith, H. Koerner, N. Tabiryan, R. A. Vaia, T. J. Bunning and T. J. White, *Adv. Funct. Mater.,* 2011, **21**, 2913.

143. Y. Wang, *Acc. Chem. Res.*, 2016, **49**, 1401.

144. L. M. Guo and Y. Wang, *Chem. Commun.*, 2014, **50**, 12022.

145. L. M. Guo and Y. Wang, *Macromolecules*, 2015, **48**, 8471.

146. M. J. Wei, W. Sun, X. S. Shi, Z. G. Wang and Y. Wang, *Macromolecules*, 2016, **49**, 215.

147. J. Yin, X. P. Yao, J. Y. Liou, W. Sun, Y. S. Sun and Y. Wang, *ACS Nano*, 2013, **7**, 9961.

148. Y. Wang and F. B. Li, *Adv. Mater.*, 2011, **23**, 2134.

149. X. X. Song, R. S. Zambare, S. Qi, B. N. Sowrirajalu, A. P. J. Selvaraj, C. Y. Tang and C. J. Gao, *ACS Appl. Mater. Interfaces*, 2017, **9**, 41482.

150. Y. Y. Liu, B. Xu, S. T. Sun, J. Wei, L. M. Wu and Y. L. Yu, *Adv. Mater.*, 2017, **29**, 1604792.